



UNIVERSITY OF
LEICESTER

Department of Engineering

University of Leicester

**Microstructure evolution and hydrogen embrittlement
in super duplex stainless steels**

Thesis submitted for the degree of

Doctor of Philosophy

at the University of Leicester

by

Xingzhong Liang

May 2018

Abstract:

Microstructure evolution and hydrogen embrittlement in super duplex stainless steels

Xingzhong Liang

Super duplex stainless steel has a wide range of applications in chemical transport and processing facilities, especially in subsea oil and gas pipelines. A desirable combination of corrosion resistance and mechanical properties can be delivered by a balanced duplex microstructure. However, the microstructure of steel can be altered during processing, which can result in degradation of mechanical properties and corrosion resistance. In offshore environment, cathodic protection is widely used to improve corrosion resistance of gas and oil transportation pipelines. However, the application of cathodic protection can trigger the evolution of atomic hydrogen, which can adversely affect the macroscopic mechanical properties. Solute hydrogen induces premature failure, which is known as hydrogen embrittlement.

In this project, microstructure evolution in super duplex stainless steel was first investigated. A new Cr_2N precipitation mechanism has been proposed that a nano size lamellar M_{23}C_6 facilitates Cr_2N rods precipitation in super duplex stainless steel. To study Cr_2N precipitates in super duplex stainless steel weldment, transmission Kikuchi diffraction (TKD) was used to measure the geometrically necessary dislocation distribution (GND) around Cr_2N . The TKD-GND results suggest a high GND density can be measured in nano-sized regions adjacent to Cr_2N . The effect of hydrogen charging on dislocation multiplication in super duplex stainless steel was investigated and it is found that dislocation density multiplies by about one order of magnitude in steels with under 5% pre-strain, but dislocation density remains the same in steel with pre-strain at 10% and above. EBSD was used to study the effect of hydrogen on crack propagation. Hydrogen assists crack propagation through ferrite but can be trapped by both ferrite and austenite. It is found that austenite traps cracks by emitting dislocations or forming secondary grain boundaries ahead of crack tips, while in ferrite grains, the grain boundaries can impede crack propagation. The above findings provide new insight into microstructure evolution and hydrogen induced failure in super duplex stainless steel.

Publications

- [1] X.Z. Liang, M.F. Dodge, J. Jiang, H.B. Dong, Using transmission Kikuchi diffraction in a scanning electron microscope to quantify geometrically necessary dislocation density on nanoscale (submitted to *Ultramicroscopy*).
- [2] X.Z. Liang, M.F. Dodge, S. Kabra, J.F. Kelleher, T.L. Lee, H. B. Dong, Effect of hydrogen charging on dislocation multiplication in pre-strained super duplex stainless steel, *Scripta. Materialia* 143 (2018) 20-24.
- [3] X.Z. Liang, M.F. Dodge, W. Liang, H.B. Dong, Precipitation of chromium nitride nano-rods on lamellar carbides along austenite-ferrite boundaries in super duplex stainless steel, *Scripta. Materialia* 127 (2017) 45-48.

Acknowledgement

I wish to express my sincere gratitude to my supervisor, Professor Hongbiao Dong, for his supervision, supports and advises throughout my time at the University. He has not only provided me constant guidance but also extended my interest and desires in materials science.

I would also like to thank staff members in the Department of Engineering who have supported me. Professor Keith Carter is thanked for his professional knowledge and contributions to the current work; Graham Clarke and Vinay Patel are thanked for fundamental training of laboratory equipment;

I am deeply in debt to my industrial supervisor Dr Michael Dodge at TWI. His expertise and insight has deepened my understandings on this research topic. I am grateful for his time and discussion in the writing of published papers. It would be unimaginable to publish my research work without his help.

I would like to thank Saurabh Kabra, Joe Kelleher, Tung-lik Lee in the beamline team at ISIS, for their unwavering supports during beam hours and off hours of my experiment.

Thanks to all my friends in Leicester, including but not limited to: Baber Saleem, Stephan Hug, Hai Yan, Lixin Zhang, Huang Jiang, Ruiyao Zhang, Zihui Dong, Dr. Jie Shen, Shuo Feng, Lida Che, Xinpu Chen, Dr. Huadong Fu, Dr. Duyao Zhang, Rui Yan. It is fantastic to have met you all in Leicester.

Finally, thanks to my parents who provide me constant encourage and support throughout my PhD study. Thanks to my fiancée, my life is full of happiness with you. I am looking forward to welcoming our new family member in eight months. I love you all forever.

Abbreviations

BCC	Body centre cubic
BSE	Backscatter electron
CCT	Continuous-cooling-transformation
CSL	Coincidence site lattice
DEP	Dislocation etch pits
DSS	Duplex stainless steel
EBSD	Electron backscatter diffraction
EDS	Energy dispersive x-ray spectroscopy
FCC	Face centre cubic
FWHM	Full width at half maximum
GND	Geometrically necessary dislocation
HAC	Hydrogen assisted cracking
HAZ	Heat affected zone
HE	Hydrogen embrittlement
HEDE	Hydrogen enhanced decohesion
HELP	Hydrogen enhanced local plasticity
HISC	Hydrogen induced stress cracking
IPF	Inverse pole figure
KAM	Kernel average misorientation

ND	Neutron diffraction
OM	Optical microscopy
PRENW	Pitting resistance equivalent number (with tungsten)
SADP	Selected area diffraction pattern
SDSS	Super duplex stainless steel
SE	Secondary electron
SEM	Scanning electron microscopy
SSD	Statistically stored dislocation
STEM	Scanning transmission electron microscopy
TEM	Transmission electron microscopy
TKD	Transmission Kikuchi diffraction
TOF	Time of flight
TTT	Time-temperature-transformation

Symbols

σ_0	Intrinsic strength of material
σ_D	Dislocation strengthening
σ_{GB}	Grain-boundary strengthening
σ_P	Precipitation strengthening
σ_{SS}	Solid-solution strengthening,
γ	Austenite
χ	Chi phase
δ	Ferrite
σ	Sigma phase
b	Burgers vector
C	Concentration of the diffusing species.
C_0	Initial uniform concentration of the diffusing atoms in the material
C_s	Constant concentration of the diffusing atoms at the surface of the material.
C_x	Concentration of the diffusing atom at location x
D	Diffusion coefficient
d	Grain size
d	Interplanar spacing
D_0	Temperature-independent pre-exponential factor (m^2/s)
d_{GND}	Unit length of GND measurement
d_{hkl}	Interplanar spacing
E	Young's modulus
G	Shear modulus
h	Planck's constant
J	Diffusion flux
k_1	Storage constant
k_2	Dynamic recovery constant
k_{GB}	Grain boundary strengthening coefficient
L	Spacing between pinning points
L	Neutron flight distance

M	Mass
m_n	Neutron mass
M_T	Taylor's factor
N	Entropy factor
Q_d	Activation energy for diffusion (J/mol);
Q_v	Formation enthalpy of mono-vacancy
R	Gas constant
r	Second phase particle radius
T_K	Absolute temperature (K) (1.4.4)
t	Grain size
T	Temperature (°C)
t	Time of diffusion
ν	Poisson's ratio
x	Distance
α	Constant for scaling the interaction strength between dislocations
γ	Surface energy
Δd	Peak broadening of neutron diffraction
ε	Elastic strain
θ	Neutron scattering angle
λ	Neutron wavelength
ρ	Dislocation density
τ	Shear stress

Table of Contents

Chapter 1	Introduction and Literature Review	- 1 -
1.1	Introduction	- 2 -
1.2	Super duplex stainless steel.....	- 3 -
1.2.1	Fundamentals of duplex stainless steel.....	- 3 -
1.2.2	Subsea challenges and materials requirement for super duplex stainless steel.....	- 4 -
1.2.3	Chemistry of super duplex stainless steel	- 5 -
1.2.4	Phase transformations in super duplex stainless steel.....	- 7 -
1.3	Strengthening mechanisms.....	- 11 -
1.3.1	Solid solution hardening	- 12 -
1.3.2	Dislocation hardening	- 12 -
1.3.3	Grain-boundary hardening	- 13 -
1.3.4	Precipitation hardening	- 13 -
1.4	Hydrogen in metals	- 14 -
1.4.1	Atomic features of hydrogen	- 14 -
1.4.2	Hydrogen degraded materials plasticity.....	- 15 -
1.4.3	Introducing H into metals	- 16 -
1.4.4	Diffusion of H in metals	- 16 -
1.4.5	Mechanisms of hydrogen embrittlement	- 18 -
1.5	Hydrogen-defects interaction	- 22 -
1.5.1	Hydrogen-vacancy interaction	- 22 -
1.5.2	Hydrogen-dislocation interaction.....	- 23 -

1.5.3	Hydrogen-boundaries interaction.....	- 26 -
1.6	Development of transmission Kikuchi diffraction	- 27 -
1.6.1	Background of EBSD	- 27 -
1.6.2	Transmission Kikuchi diffraction	- 28 -
1.6.3	General applications of SEM-TKD	- 29 -
Chapter 2	Experimental methods	- 32 -
2.1	Sample preparation.....	- 33 -
2.1.1	Samples used in Chapter 3.....	- 33 -
2.1.2	Samples used in Chapter 4.....	- 35 -
2.1.3	Samples used in Chapter 5.....	- 37 -
2.2	Equipment	- 38 -
2.2.1	Equipment used in Chapter 3.....	- 38 -
2.2.2	Equipment used in Chapter 4.....	- 39 -
2.2.3	Equipment used in Chapter 5.....	- 39 -
2.3	Methodology	- 40 -
2.3.1	Modelling of phase transformation.....	- 40 -
2.3.2	Using neutron diffraction to measure dislocation density in Chapter 4.....	- 40 -
2.3.3	Using TKD to measure geometrically necessary dislocation in Chapter 5 ..	- 44 -
Chapter 3	Phase transformation in super duplex stainless steel	- 53 -
3.1	Equilibrium phase transformations of SDSS	- 54 -
3.2	Precipitation in super duplex stainless steels	- 55 -
3.2.1	Isothermal phase transformation.....	- 55 -

3.2.2	Element concentration in precipitates	- 56 -
3.2.3	Precipitation by isothermal heat treatment	- 58 -
3.2.4	Precipitation of sigma phase	- 59 -
3.2.5	Precipitation of chi phase.....	- 63 -
3.2.6	Precipitation of nitrides and carbides.....	- 64 -
3.3	Precipitates in HAZ of a weldment	- 68 -
3.3.1	Continuous cooling transformation.....	- 68 -
3.3.2	Precipitates in HAZ of a weldment.....	- 69 -
3.3.3	Precipitation of chromium nitrides	- 72 -
3.4	Chapter summary	- 82 -
Chapter 4	Effect of hydrogen charging on dislocation multiplication in pre-strained super duplex stainless steel.....	- 83 -
4.1	Modelling of hydrogen concentration after hydrogen charging.....	- 84 -
4.2	Results of dislocation density as a function of pre-strain.....	- 85 -
4.3	The multiplication and annihilation of dislocation	- 88 -
4.3.1	Athermal storage of dislocation	- 88 -
4.3.2	Source of dislocation multiplication	- 88 -
4.3.3	Saturation of dislocation density.....	- 89 -
4.4	Chapter summary	- 90 -
Chapter 5	Effect of hydrogen on crack propagation.....	- 92 -
5.1	Hydrogen assisted crack propagation in SDSS	- 93 -
5.2	Effect of hydrogen on cleavage behaviour.....	- 93 -
5.2.1	Fracture behaviours in hydrogen free and hydrogen charged samples.....	- 93 -

5.2.2	EBSD result of fracture behaviour in hydrogen free sample	- 95 -
5.2.3	EBSD of fracture behaviour in hydrogen charged sample	- 98 -
5.3	Trapping mechanisms of hydrogen assisted crack propagation	- 102 -
5.3.1	GND density distribution ahead of crack tip	- 102 -
5.3.2	Crack trapping mechanisms in SDSS with hydrogen concentration	- 103 -
5.4	Chapter summary	- 104 -
Chapter 6	Conclusions and future work	- 105 -
6.1	Conclusions	- 105 -
6.2	Future work	- 106 -
References	- 108 -

List of Tables

Table 1-1 Nominal chemical composition (wt. %) of some common DSS and SDSS [1, 16]-	5
-	
Table 2-1 Chemical composition of SDSS pipeline sample	33 -
Table 2-2 Chemical composition of SDSS weldment sample	34 -
Table 2-3 Prepared samples in this study	36 -
Table 3-1 STEM-EDS results of the Cr_2N and M_{23}C_6	66 -
Table 3-2 SEM-EDS results performed in HAZ of a weldment.....	71 -
Table 3-3 STEM-EDS result of chromium rich precipitates	73 -

List of Figures

Figure 1-1 Hydrogen assisted failure of SDSS hub and two pipes, removal from the manifold [13].....	- 3 -
Figure 1-2 Precipitation diagram of DSS [4].....	- 8 -
Figure 1-3 Schematic diagram of σ phase precipitation in duplex stainless steel [25].....	- 9 -
Figure 1-4 Schematic representation of χ phase precipitation in duplex stainless steel [26].-	10
-	
Figure 1-5 Mechanism of Orowan strengthening [45]	- 14 -
Figure 1-6 Periodic table with atomic radius feature [46].	- 15 -
Figure 1-7 Different crack tip angle opening in Fe-3wt. %Si single crystal after straining in (a) vacuum and (b) hydrogen [9].....	- 19 -
Figure 1-8 Observation of hydrogen induced dislocation pile-up (lines marked as overlapped grey lines), original dislocation position shown in black colour [62].....	- 20 -
Figure 1-9 Illustration of micro-crack evolution during loading: (a) in the absence of H, blunting of crack tip impeded its propagation, and (b) in the presence of H, dislocation emission inhibited, leading to cleavage fracture [67].	- 21 -
Figure 1-10 Effect of H-vacancy complex on dislocation movement; (a) dislocations movement by cyclic loads without hydrogenation, where four mobile dislocation lines were observed; (b) dislocations positions before hydrogenation and (c) after hydrogenation; (d) dislocation response to same cyclic load after hydrogenation. Scale bars stand for 200 nm [70].	- 23 -
Figure 1-11 Evolution of the dislocation density of cold-rolled palladium with increasing hydrogen content during cold rolling. The measurements were performed by two different methods: interpretation of the diffraction patterns of the samples using the method of Williamson-Hall and measurement of the relative dislocation density by evaluating the diffusion time of hydrogen through the palladium samples.	- 25 -

Figure 1-12 EC-AFM deflection mode images from the surface of the sample during in situ electrochemical H-charging. (a) Before H-charging at the OCP; on the left is a ferrite grain and on the right is an austenite grain which can be easily distinguished by its convex grain boundary. (b) The image of the same position after 1 h of in situ H-charging. (c) The image of the same position after 2.5 h of in situ H-charging. (d) Higher magnification image of the surface of the austenite grain. Images from reference [77]. - 25 -

Figure 1-13 TEM micrographs of cold-rolled palladium without hydrogen (a) and with 0.1 at.% H/Pd (b), 0.5 at.% H/Pd (c) and 1.0 at.% H/Pd (d) during the cold rolling. Reduction in thickness: 50%. Cite from Ref. [76]. - 26 -

Figure 1-14 Principle set-up of (a) EBSD and (b) TKD [89-93]. - 29 -

Figure 1-15 TKD results of a duplex stainless steel (a) phase map; IPF-z plot of (b) ferrite and (c) austenite [101] - 30 -

Figure 1-16 Orientation map of an ultra-fine grained titanium alloy; the black and white arrows indicating twin boundaries and twin boundaries segments [102]. - 31 -

Figure 2-1 Photomicrograph of the welded super duplex stainless steel joint in the etched condition. A thin foil sample was machined from the heat-affected zone on the forging side of the joint. - 34 -

Figure 2-2 Schematic representation of sample machining from a raw pipe structure. - 35 -

Figure 2-3 Dimensions of tensile sample; direction of x is longitudinal, y is radial and z axis is hoop; unit in mm. - 35 -

Figure 2-4 Tensile curve of sample engineering strain (%) against force (kN); the pre-strain of 5%, 10% and 15% can be achieved with 5.2275, 5.5500 and 5.7525 kN loads; uncertainty of pre-strain is measured as 0.3% - 36 -

Figure 2-5 Schematic representation of hydrogen charging cell. - 37 -

Figure 2-6 Neutron diffraction set-up in ENGIN-X, ISIS, UK [103]. - 39 -

Figure 2-7 Schematic diagram of Bragg diffraction - 42 -

Figure 2-8 A schematic diagram of the KAM measurement. For the first order (i.e. 3×3 pixel) measurements, the local orientation is calculated between the host pixel (in red) and the nearest pixels (in yellow). Similarly, the second order (5×5 pixels) measurement of KAM will be calculated between the host pixel and the nearby pixels in both blue and yellow..... - 45 -

Figure 2-9 Experiment methods for dislocation detection [44, 62, 74, 97, 100, 122-125, 129-132]. - 47 -

Figure 2-10 KAM and GND density maps of a selected area within a ferrite grain: first order results of (a) KAM and (b) GND; second order results of (c) KAM and (d) GND. Invalid pixels of GND are shown in blue. - 48 -

Figure 2-11 Histogram of scanned GND density values in local area using first order and second order calculation schemes. - 49 -

Figure 2-12 Bright field imaging by TEM under different diffraction conditions (a) $g//(110)$ and (b) $g//(1\bar{1}0)$. Visibility of dislocation under different diffraction conditions is given in Fig. 7. The TKD scanned area is bound by the purple box. (c) a closer view of the dislocation lines; two regions, Area-1 and Area-2, are illustrated for comparison; the red circle area in TKD-GND result shows high density of dislocations, which is consistence with the TEM observation; dislocations in (c) were highlighted by white dashed lines. - 50 -

Figure 2-13 TEM bright field images of dislocations under different diffraction conditions (a) $g//(1\bar{1}0)$ and (b) $g//(110)$ with the incident beam direction approximately parallel to zone axis [001]; (c) schematic representation of zone-axis pattern with tabled dislocation visibility; dislocation is invisible when $g \cdot b=0$ - 51 -

Figure 3-1 Fe-Cr-Ni equilibrium phase diagram for 68 wt. %Fe [135]..... - 54 -

Figure 3-2 Equilibrium phase diagram of Zeron 100, calculated by Thermo-Calc (TCFE-6 database). - 55 -

Figure 3-3 TTT diagram of SDSS, phase fraction is in weight percentage. - 56 -

Figure 3-4 Element concentration is different phases, calculated by JMatPro. - 57 -

Figure 3-5 Phase evolution of SDSS by 800°C isothermal heat treatment with heat ageing time of (a) 0 min, (b) 6 min, (c) 30 min, (d) 60 min; orange and red arrows point to the precipitation of χ phase and σ phase, respectively; images obtained by SEM under BSE mode. - 59 -

Figure 3-6 Impact energy of SDSS against varies ageing times at 800°C. - 60 -

Figure 3-7 TEM bright field image of σ phase precipitation at a ferrite-ferrite grain boundary; EDS map was obtained from the red boxed area; EDS point tests were performed on three points with EDS results tabled. - 61 -

Figure 3-8 TKD result of σ phase precipitation at a ferrite-ferrite grain boundary. - 62 -

Figure 3-9 A proposed mechanism of σ phase precipitation at a ferrite-ferrite grain boundary. - 63 -

Figure 3-10 Characterisation of χ phase at a phase boundary: (a) scanning area shown in SEM-SE and (b) EBSD result. - 63 -

Figure 3-11 TEM bright field image of rod Cr_2N precipitates (yellow arrows pointed) in the ferrite matrix. - 64 -

Figure 3-12 TEM bright field image of rod Cr_2N precipitates (yellow arrows pointed) at phase boundary; part of austenite has been polished off during sample preparation. - 65 -

Figure 3-13 STEM observation of rod-shaped precipitates on a thin lamellar precipitate, and the corresponding EDS examination results are shown in Table 1; EDS mapping, results on right side, was performed to examine the highlighted area (yellow box). - 66 -

Figure 3-14 (a) low magnification TEM image of the grain boundary, which shows Cr_2N rods ‘seating’ on the vicinity lamellar M_{23}C_6 ; (b) high magnification image of the lamellar M_{23}C_6 from the yellow boxed area which shows the width of this M_{23}C_6 is ~ 20 nm; HR images of (c), (d) and (e) are taken from the square boxed selected areas (SAs) with corresponding colours;

scale bars for HR images on the right side are 1 nm; the predominant orientation relationship can be confirmed as

$(0002)Cr_2N || (400)M_{23}C_6 || (110)\delta$ and $[\bar{1}100]Cr_2N || [01\bar{1}]M_{23}C_6 || [\bar{1}11]\delta$ - 67 -

Figure 3-15 (a) TEM image indicating SAs of austenite and ferrite; (b) SADP of ferrite in zone axis $[\bar{1}11]\delta$; (c) SADP- γ near zone $[\bar{1}14]$; (d) clear $[\bar{1}14]\gamma$ austenite SADP after 3.2° rotation around $[\bar{1}11]\delta$; (e) Schematic representation of ferrite and austenite diffraction pattern, revealing austenite does not have a direct orientation relationship with either ferrite or $M_{23}C_6$ -
68 -

Figure 3-16 CCT diagram of SDSS, phase fraction is in weight percentage. - 69 -

Figure 3-17 SEM images show the morphology of (a) Flange; (b) HAZ Cap and (c) HAZ Root.
..... - 70 -

Figure 3-18 Precipitates in HAZ of the weldment..... - 71 -

Figure 3-19 Cr_2N precipitates at austenite-ferrite phase boundary, imaged by SEM in SE mode.
..... - 72 -

Figure 3-20 STEM image of a chromium rich precipitate at a boundary; four STEM-EDS spot tests were performed across the precipitate; spectrum 7 shows a high chromium content 46.1 wt. % while the matrix only has approximately 24 wt. % chromium contents. - 73 -

Figure 3-21 STEM image of chromium rich precipitates at a phase boundary; STM-EDS map scan is obtained from the masked area. - 74 -

Figure 3-22 Cr_2N precipitates at a ferrite-ferrite grain boundary, imaged by BSE mode in SEM.
..... - 75 -

Figure 3-23 TKD Results of Cr_2N precipitates at a ferrite-ferrite grain boundary: (a) Phase map; (b) Grain boundary map, result of misorientation line profile is shown in (c); (d) and (e) are KAM maps using 1st and 2nd order scheme, respectively; (f) and (g) are GND maps using 1st and 2nd order scheme, respectively; invalid pixels of GND are shown in blue. - 76 -

Figure 3-24 Cr₂N precipitates at a ferrite-austenite phase boundary; (a) BSE image and TKD scanning performed in yellow boxed area; (b) Phase map, EBSPs of ferrite, Cr₂N and austenite are shown on the right side; (c) KAM map and (d) GND map, calculated by first order scheme.

..... - 77 -

Figure 3-25 STEM-EDS results of a Cr₂N at a ferrite/ferrite grain boundary; a 45.5 wt. % chromium was examined from Cr₂N by using Point EDS; EDS line profile result of chromium, iron, nickel and nitrogen elements cross the Cr₂N is shown as above.....

Figure 3-26 Cr₂N precipitates at a ferrite-ferrite grain boundary; SADP is obtained from yellow rings and results show in figures I to IV; white arrows point the diffraction spots from ferrite contribution.

Figure 3-27 Dictra modelling of Cr₂N precipitation at a ferrite-austenite phase boundary; evolution of (a) chromium concentration and (b) nitrogen concentration; the unit of distance is a metre.....

Figure 4-1 Hydrogen concentration against sample depth with 10 days hydrogen charge. Hydrogen diffusivity values of $5.0 \times 10^{-15} \text{ m}^2/\text{s}$, $1.0 \times 10^{-14} \text{ m}^2/\text{s}$ and $5.0 \times 10^{-14} \text{ m}^2/\text{s}$ are applied for modelling. Hydrogen concentrations of 40 ppm and 2 ppm is assumed for surface and bulk, respectively.

Figure 4-2 Neutron diffraction spectrum patterns of (a) lattice plane normal to sample longitude direction, signal collected from North bank; (b) lattice plane normal to sample transverse direction, signal collected from South bank. Abbreviations of hf and hc stand for hydrogen free and hydrogen charged, respectively. The numbers 0, 5, 10, and 15 represent the percentage of pre-strain.

Figure 4-3 Dislocation density in austenite (face centre cubic, FCC) and ferrite (body centre cubic, BCC) as a function of different pre-strain; abbreviation of L and T strand for longitudinal

and transverse, respectively; overall dislocation density is calculated by linearly averaging the values of dislocation density determined from both directions. - 87 -

Figure 5-1 Fractures on the side surface in the necking area of hydrogen free sample after tensioning, imaged by OM; stress was applied vertically..... - 94 -

Figure 5-2 Fractures on the side surface in the necking area of hydrogen charged sample after tensioning, imaged by OM; stress was applied vertically..... - 94 -

Figure 5-3 EBSD maps of a crack tip in a hydrogen free sample: (a) SEM-SE micrograph ; (b) Phase map; (c) and (d) are KAM maps using first order and second order calculation schemes, respectively; (e) and (f) are calculated GND density using first order and second order schemes, respectively. Invalid GND density values are shown in blue. Tensile stress applied vertically.- 96 -

Figure 5-4 Another EBSD scan result of a crack tip in a hydrogen free sample: (a) SEM-SE micrograph; (b) Phase map; (c) and (d) are KAM maps using first order and second order calculation schemes, respectively; (e) and (f) are calculated GND density using first order and second order schemes, respectively. Invalid GND density values are shown in blue. Tensile stress applied vertically..... - 97 -

Figure 5-5 EBSD characterisation of a mesoscale crack in the hydrogen charged sample after tensioning: (a) band contrast map; (b) Phase map, the ferrite phases are in blue and austenite phases are in red; yellow arrows point to crack tips which get trapped in the austenite phase. Tensile stress applied vertically..... - 98 -

Figure 5-6 EBSD result of a microcrack that gets trapped in austenite in the hydrogen charged sample after tensioning: (a) Band contrast; (b) Phase map; (c) Grain boundary plot; (d) CSL grain boundary; (e) and (f) KAM map using first order and second order calculation schemes, respectively; (g) and (h) are calculated GND density using first order schemes and second order

calculation schemes, respectively. Invalid GND density values are shown in blue. Tensile stress applied vertically..... - 99 -

Figure 5-7 EBSD result of sub-grain boundary formation in austenite in the hydrogen charged sample after tensioning: (a) Band contrast; (b) Phase map; (c) IPF (Z) map; (d) Grain boundary plot; (e) CSL grain boundary plot; next page, (f) and (g) are KAM maps using first order and second order calculation schemes, respectively; (h) and (i) are calculated GND density using first order and second order schemes, respectively. White arrows in (c) and (h) point to the formed secondary grain boundaries. Invalid GND density values are shown in blue. Tensile stress applied vertically..... - 101 -

Figure 5-8 EBSD result of a microcrack that gets trapped at a ferrite grain boundary in the hydrogen charged sample after tensioning: (a) SEM-SE micrograph; (b) Phase map; (c) and (d) are KAM maps using first order and second order calculation schemes, respectively; (e) and (f) are calculated GND density using first order and second order schemes, respectively. Invalid GND density values are shown in blue. Tensile stress applied vertically. - 102 -

Chapter 1

Introduction and Literature Review

This opening chapter will detail the background and motivation of this work:

Section 1.1 provides a general context for the work;

Section 1.2 introduces the development of super duplex stainless steels;

Section 1.3 introduces strengthening mechanisms of metals;

Section 1.4 introduces the fundamental concept of hydrogen in metals;

Section 1.5 introduces hydrogen-defects interactions;

Section 1.6 introduces the methodology of transmission electron microscopy.

1.1 Introduction

In recent decades, great strides have been made in the development of super duplex stainless steel (SDSS), where a balanced structure of ferrite and austenite in SDSS provides superior corrosion resistance as well as good mechanical properties [1, 2]. Such advances of SDSS have made it a suitable candidate for applications in harsh environment, for example, offshore pipeline application. Nevertheless, challenges remain during manufacturing, processing and servicing of SDSS.

During manufacturing and processing, materials are subject to temperature changes. For example, a welding process will heat materials over melting temperature, followed by rapid cooling down to room temperature. Such temperature change would possibly induce changes to the balanced microstructure and introduce precipitation of secondary phases. These microstructure changes can degrade mechanical properties and corrosion resistance of SDSS [1-4].

Another degradation of SDSS during service comes from hydrogen embrittlement. Hydrogen is the lowest atomic number element and it plays a significant role in metals. A small amount of solute hydrogen can degrade materials mechanical properties resulting in a materials premature failure [5]. Such failures have been documented in pure metals or alloys involving iron, nickel, titanium, aluminium, palladium and so on [5-12].

Despite the superior properties of SDSS which make it an irreplaceable component in subsea oil and gas pipeline system, its application still suffers the microstructure change during materials processing and hydrogen embrittlement during offshore servicing. For example, Figure 1-1 shows a documented hydrogen assisted failure of SDSS whose leakage was detected after six months servicing under cathodic protection [13]. The failure position was detected in the heat-affected-zone whose microstructure is different from the base

material. In the heat-affected-zone (HAZ) of SDSS microstructure changes can include grain growth, new phase precipitation and increase of defects density. Critical threshold combinations of the presence of sensitive microstructures, stress and hydrogen concentration can lead to hydrogen embrittlement.



Figure 1-1 Hydrogen assisted failure of SDSS hub and two pipes, removal from the manifold [13]

The motivation of this work is to understand microstructure evolutions in SDSS and then investigate their effects on mechanical properties and hydrogen embrittlement of SDSS.

1.2 Super duplex stainless steel

SDSS is formed from a balanced microstructure of ferrite and austenite. In this Section, the development of SDSS is introduced, together with its chemistry, microstructures, mechanical properties and applications.

1.2.1 Fundamentals of duplex stainless steel

Duplex stainless steels are designed to have a half-ferrite half-austenite microstructure. In subsea oil & gas pipeline application, a typical weakness of austenitic stainless steel is its low resistance to stress corrosion cracking whilst a poor toughness is presented in ferritic stainless steel weldment [2]. These shortcomings can be largely corrected by presence of

both ferrite and austenite in microstructure and this led to the development of duplex stainless steel (DSS) [1, 14].

Duplex grades kept developing for decades since the first wrought duplex stainless steel was introduced in Sweden in early 1930. However, the poor as-weld condition of DSS has impeded its development in broader applications. Only with the nitrogen alloying in DSS, the performances of DSS weldment were dramatically improved. Indeed, nitrogen addition promote the austenite formation and reduce the formation of precipitates in HAZ [15]. In the 1990s, a series of standard DSS was produced, e.g. one of the most well-known grades is SAF 2205 (a Sandvik-owned trademark).

1.2.2 Subsea challenges and materials requirement for super duplex stainless steel

DSS is designed by taking advantages of austenite and ferrite and minimise their individual weaknesses. In general, DSS has the following materials characters: a relatively high strength (400-550 MPa for 0.2% proof stress), good weldability, superior toughness and resistance to stress corrosion cracking. Due to these advantages, DSS is still being developed and having a higher proportion of usage in subsea oil & gas pipeline applications.

However in subsea environment, a higher corrosion resistance is paramount for the reliability of pipeline structures. This demand has led to improvement on DSS, where more alloying elements are introduced and it is termed as SDSS. SDSS was developed with a higher alloying composition according to pitting resistance equivalent number (with tungsten) (PREN_W) which is determined by $\%Cr + 3.3(\%Mo + 0.5x\%W) + 16x\%N$ (taking tungsten into account in weight percentage) [16]. Table 1-1 shows PREN_W for some common DSS and SDSS grades. A typical PREN_W of DSS UNS S31803 (SAF 2205) is indexed around 35. In comparison, the approximate PREN_W of SDSS UNS S32760 (Zeron 100) is calculated to be 41, which means a higher pitting corrosion resistance [1].

Table 1-1 Nominal chemical composition (wt. %) of some common DSS and SDSS [1, 16]

Tradename	Standard	Cr	Mo	Ni	N	Other elements	PRENW
SAF 2205	UNS S31803	22	3	5.3	0.17	-	35
DP 3	UNS S31260	25	3	6.5	0.16	0.5Cu, 0.3W	37
Zeron 100	UNS S32760	25	3.6	7	0.25	0.7Cu, 0.7W	41
SAF 2507	UNS S32750	25	3.8	7	0.27	-	42

1.2.3 Chemistry of super duplex stainless steel

A variety of alloying elements were introduced in SDSS to form a stable ferrite-austenite structure with good corrosion resistance and desirable mechanical properties. As mentioned above, PRENW is introduced as a general guideline to evaluate the corrosion resistance of stainless steels, by which higher composition contents of chromium, nitrogen, molybdenum and tungsten were found favourable in SDSS. Here, a brief review is made to discuss the role of these four elements in SDSS.

1.2.3.1 Chromium

Chromium is a strong ferrite stabilizer which promotes the ferrite formation in SDSS [15]. In general, higher chromium content can provide a better corrosion resistance for materials since the addition of chromium content in SDSS can form a stable chromium passive film. This passive film protects the steel surface against environmental corrosion. However, higher chromium content also promotes the formation of precipitates such as chromium carbides, chromium nitrides, σ phase, brittle chromium-rich ferrite etc. Such precipitation will be discussed in Section 1.2.4.

1.2.3.2 Nitrogen

Nitrogen is an important alloying element and has multiple functions in SDSS. Firstly, nitrogen can dramatically increase the pitting and intergranular corrosion resistance of

SDSS by the nitrogen solid solution [17]. Secondly, enhancement of mechanical properties can be achieved by interstitial solid solution strengthening [17]. In the third place, the addition of nitrogen improves the weldability of duplex stainless steels since it delays the intermetallic phase formation, especially carbides and σ phase precipitation in HAZ [15]. Finally, nitrogen is a very strong austenite stabiliser [18]. From an economic point of view, due to a high and unstable price trend of raw nickel resources worldwide, nitrogen is designed to replace nickel in the production of austenitic steels as well as duplex steels. Although a list of favourable enhancement can be introduced in SDSS with the addition of nitrogen content, precipitates containing nitrogen, Cr_2N as the most important one, are also introduced in SDSS at the same time. Details of background and a new precipitation mechanism of Cr_2N will be discussed in Section 1.2.4 and Section 4.2.6, respectively.

1.2.3.3 Molybdenum

In SDSS, molybdenum is a ferrite stabiliser, and is reported to be three times more effective than chromium in improving pitting and crevice corrosion resistance in chloride-containing environments [19]. In most cases, a threshold of 4 wt. % molybdenum is introduced in SDSS to reduce the formation of precipitation and keep a balanced austenite-ferrite ratio. Nevertheless, the addition of molybdenum increases the tendency of χ phase precipitation. The precipitation mechanism of χ phase is detailed in Section 1.2.4.

1.2.3.4 Tungsten

Due to a low alloying composition of tungsten in most common SDSS, tungsten is less mentioned comparing with chromium, nitrogen and molybdenum, and sometimes even absent in PREN formula. In SDSS, the addition of tungsten is to stabilise a passive film against corrosion on pitting and crevice [16]. However, some reports have suggested that the addition of tungsten increases the precipitation tendency [16, 20, 21]. Precipitation of χ phase can be promoted by tungsten addition due to its higher diffusion rate at grain

boundaries and therefore encouraging early precipitation of χ phase. Meanwhile, the formation of σ phase can be delayed with tungsten addition.

1.2.3.5 Other elements

As described above, the four desirable elements have their individual merit in alloying SDSS. However, there are other detriment elements presence in the SDSS, for example, carbon always present and forms various harmful carbides. Therefore, producing SDSS with lower carbon content is always favourable in industry. Carbon content less than 0.03 wt. % is regarded as a safe level and this designed cap has been achieved at present [1, 2]. However, in this study, a thin lamellar structure $M_{23}C_6$ was observed that can dramatically trigger Cr_2N array formation at an austenite-ferrite grain boundary by isothermal heating at 800°C [3]. This phenomenon implies a new role of carbides in SDSS and will be discussed in Section 4.2.6.

1.2.4 Phase transformations in super duplex stainless steel

Although a balanced ferrite-austenite phase structure is always desirable for SDSS, precipitates are difficult to avoid during manufacturing and processing. A precipitation diagram for DSS is shown in Figure 1-2 which is also applicable for SDSS. Precipitates in SDSS can generally be divided into two groups: high temperature precipitates whose formation occurred between 600°C to 1000°C, and low temperature precipitates whose formation initiates below 600°C.

The low temperature precipitates rarely exist in SDSS since an upper limit of 300°C servicing environment is always recommended for SDSS. Compared with high temperature precipitation, the atomic diffusion rate is relatively slower at low temperatures, which results in a slow process of low temperature precipitates initiation and growth. For the

group of high temperature precipitates, they could be formed in a short time during material processing such as forging, hot rolling and welding.

In SDSS, these precipitates have detrimental effects on both corrosion resistance and mechanical properties. For SDSS in the subsea pipeline application, the most common precipitates are chromium nitrides, σ phase and χ phase. It is still a large challenge, for SDSS application in subsea oil & gas pipeline, to avoid the presence of these precipitates. Here, we review the types of precipitates and their precipitation mechanisms in SDSS.

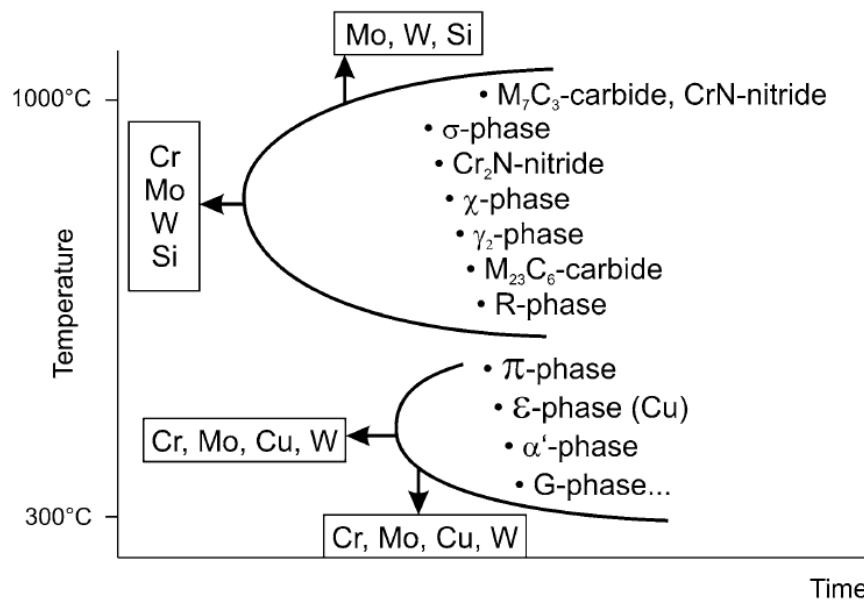


Figure 1-2 Precipitation diagram of DSS [4]

1.2.4.1 Sigma phase

σ phase is a well-known chromium-rich precipitate and can be formed in a large number of steels [1, 2, 22]. In 1907, Treitschke and Tammann [23] investigated a Fe-Cr binary system and they found an intermetallic compound with 40 ± 10 wt. % Cr. In 1927, Bain and Griffiths [24] studied the σ phase in the Fe-Cr-Ni ternary system and they reported the σ phase is hard and brittle which dramatically lowers the impact toughness of steels.

Investigations have been made in understanding the precipitation mechanism of σ phase in SDSS. In 2006, Villanueva et al. [25] reported a comparative study on σ phase precipitation in steels and a σ phase precipitation mechanism is proposed for DSS, as shown in Figure 1-3. In the first stage, the σ phase initiates from a ferrite-austenite phase boundary. Then the σ dendrites grow from this primary σ phase. At this stage, the precipitation of secondary austenite is accommodated. Finally, a saturated precipitation of σ is achieved.

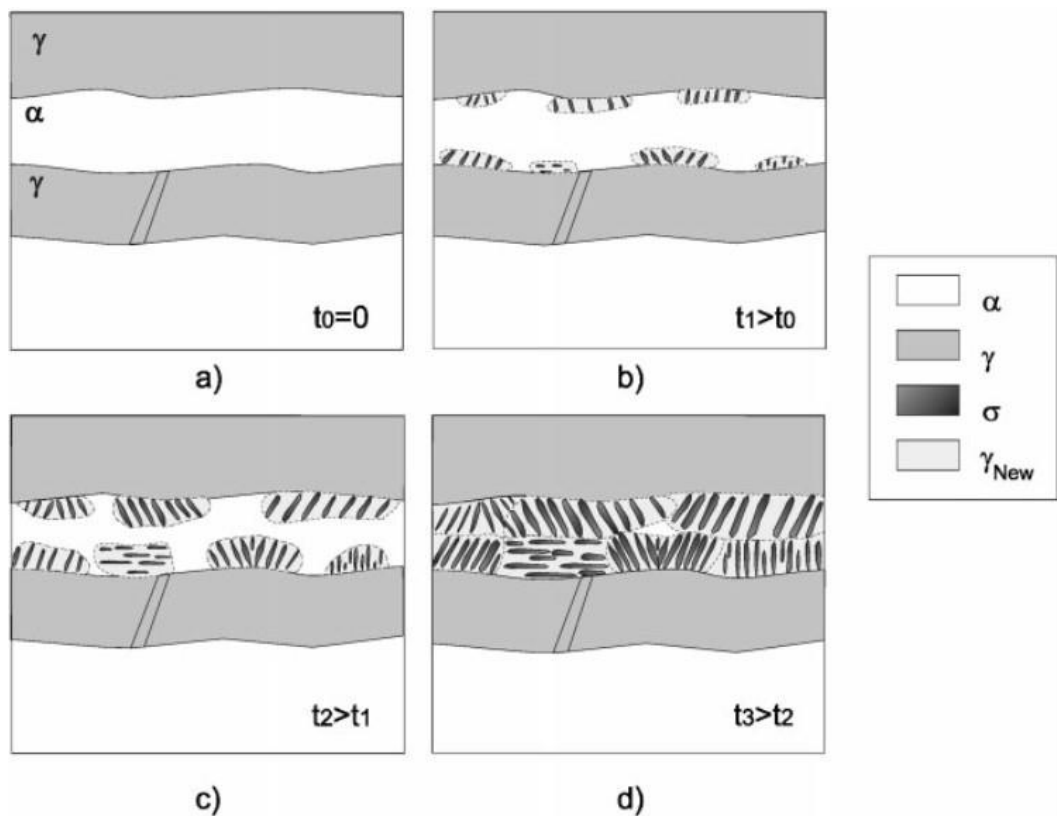


Figure 1-3 Schematic diagram of σ phase precipitation in duplex stainless steel [25].

1.2.4.2 Chi phase

χ phase is reported as a Mo-rich precipitate in steels [2, 26]. With the precipitation of χ phase in materials, the impact toughness is reduced although this effect is less than σ phase [2].

The precipitation of χ phase is believed earlier than σ phase [2]. However, the χ phase will finally transform to σ phase as χ phase is considered as a metastable precipitate. In 2009,

Escriba et al. [26] reported a precipitation mechanism for χ phase in DSS. A schematic representation diagram is shown in Figure 1-4. A ferrite-ferrite grain boundary is a preferential site for χ phase initiation. While χ phase has a larger precipitation volume, the precipitation of σ phase takes the place following χ phase and eventually becomes the dominate precipitate in DSS.

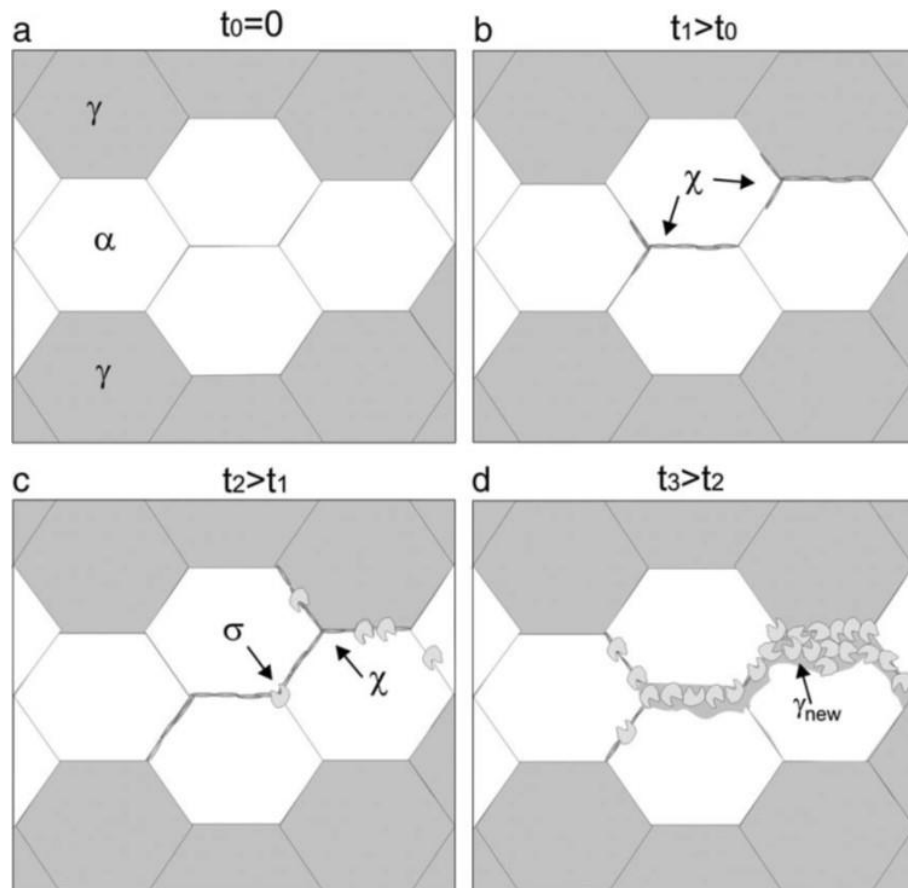


Figure 1-4 Schematic representation of χ phase precipitation in duplex stainless steel [26].

1.2.4.3 Chromium nitrides

In SDSS, chromium nitrides have two forms which are metastable CrN and stable Cr_2N [1, 2, 4, 27]. There are few reports on former one due to its rare precipitation in SDSS. However, the latter one, Cr_2N , has a relative large precipitation volume in SDSS due to the higher alloying element of chromium and nitrogen in materials.

In SDSS, the effects of Cr₂N precipitation on mechanical properties and corrosion resistance remain unclear. On the one hand, the precipitation of Cr₂N could strengthen the matrix, which could improve the mechanical property of materials [2]. On the other hand, the precipitation of Cr₂N may lead to a nanoscale chromium depletion zone which reduces the materials corrosion resistance [28, 29]. In general, the precipitation of Cr₂N should be avoided in SDSS.

Many studies have been made to investigate the mechanism of Cr₂N precipitation and there are two treatment routines to obtain Cr₂N in the matrix, i.e. ageing between 600°C to 1000°C or rapid quenching after solution heat treatment [3, 30, 31]. In an ageing process, the Cr₂N is observed to go through an embryo, core initiation and growth processes. The relevant papers have shown that tens of minutes ageing are sufficient to facilitate the precipitation of ageing-Cr₂N. Also, it has been widely accepted that grain or phase boundaries are preferential sites for Cr₂N to precipitate owing to an unordered lattice structure at boundaries. This irregular microstructure can result in a lowering of the energy barrier for the diffusion of chromium and nitrogen atoms [4, 30, 31].

1.3 Strengthening mechanisms

The strength of ideal metals is usually calculated to be considerably higher compared with their actual strength tested at the macroscale. The lower strength of actual metal is due to deformation that is facilitated by dislocation movement [32]. By hindering the dislocation movement, the strength of materials can be elevated and such strengthening sources and mechanisms are constantly being explored.

Strengthening mechanisms in polycrystalline materials are mainly summarized into four types: solid-solution hardening, grain-boundary hardening, dislocation hardening, and

precipitation hardening [32-34]. These strengthening sources can result in a comprehensive effect on materials strength and the overall strengthening can be summarised as [33, 34]:

$$\sigma = \sigma_0 + \sigma_{SS} + \sigma_{GB} + \sigma_D + \sigma_P \quad (1-1)$$

where σ_0 is the intrinsic strength of material; σ_{SS} , σ_{GB} , σ_D and σ_P are strengthening contributions from solid-solution hardening, grain-boundary hardening, dislocation hardening, and precipitation hardening, respectively.

1.3.1 Solid solution hardening

The pure metals strength can be elevated by alloying impurities, such strengthening mechanism is termed as solid solution strengthening or solid solution hardening. The impurities cause lattice distortion which hampers dislocation movement or plane slip, thus making the alloy stronger than pure metals. For example, the iron can be strengthened by alloying carbon, silicon, chromium, nitrogen etc. The following equation is suggested to estimate the solution strengthening in austenite stainless steel [35]:

$$\sigma_{SS-ASS} = 354 \%C + 20 \%Si + 3.7 \%Cr + 486 \%N^{0.5}, \text{ in weight percentage.} \quad (1-2)$$

1.3.2 Dislocation hardening

Dislocations are a type of line defect in metals and the plastic deformation of metals can be facilitated by mobile dislocation movement. With a higher density of dislocation in metals, the difficulty of dislocation movement can be achieved due to the dislocation tangle effect and thus result in a hardening. For example, the strength of material can be enhanced by applying pre-strain which extra amount of dislocations can be introduced in metals [148]. This effect is normally termed as dislocation hardening or work hardening. An empirical Taylor relation can be applied to estimate the relationship between shear stress and dislocation density [36]:

$$\tau = \alpha G b \sqrt{\rho} \quad (1-3)$$

where α is a constant for scaling the interaction strength between dislocations; G is the shear modulus; b is burgers vector; ρ is the dislocation density.

1.3.3 Grain-boundary hardening

In polycrystalline materials, grain boundaries are critical sources to strength materials. The grain boundary strengthening mechanism is by resistance to moving dislocation at grain boundary due to the large-scale lattice misfit at grain boundaries. The Hall-Petch relation is suggested to rule the strengthening contribution from grain boundaries [32]:

$$\sigma_{GB} = k_{GB} d^{-1/2} \quad (1-4)$$

where k_{GB} is the strengthening coefficient; d is grain size.

By taking the advantages of grain boundaries, nanocrystalline materials are designed to achieve a higher strength with grain sizes of tens of nanometres [37-44].

1.3.4 Precipitation hardening

In metals, precipitates can serve as pinning points for dislocation movement. For example, one popular nickel-based alloy 718 is strengthened by precipitation of γ' and γ'' .

There are two mechanisms to rule the precipitation hardening as shown in Figure 1-5.

Following equations express the dislocations cutting and bowing mechanisms [45]:

$$\tau = \frac{\pi r \gamma}{bL} \quad \text{Dislocations cutting through particles} \quad (1-5)$$

$$\tau = \frac{Gb}{L-2r} \quad \text{Dislocations bowing around particle} \quad (1-6)$$

where r is the second phase particle radius; γ is the surface energy; L is the spacing between pinning points.

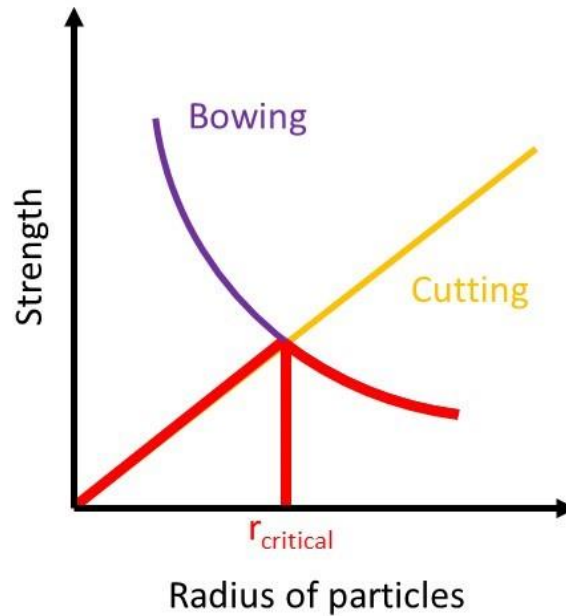


Figure 1-5 Mechanism of Orowan strengthening [45]

1.4 Hydrogen in metals

Section 1.1 introduces the background of hydrogen in SDSS. To detail the hydrogen behaviour in metals, this Section will review atomic features of hydrogen, the origin discovers of hydrogen embrittlement, hydrogen diffusion in metals and finally hydrogen embrittlement mechanisms.

1.4.1 Atomic features of hydrogen

Figure 1-6 shows a periodic table with atomic radius feature where hydrogen is the smallest atom with a radius of about 0.37 \AA . As the atomic radius from chromium to nickel is in the range of 1.2 to 1.3 \AA , the atomic radius difference between hydrogen and these alloy elements leads to relatively free interstitial of hydrogen atom among lattice gaps of Fe-based crystalline materials.

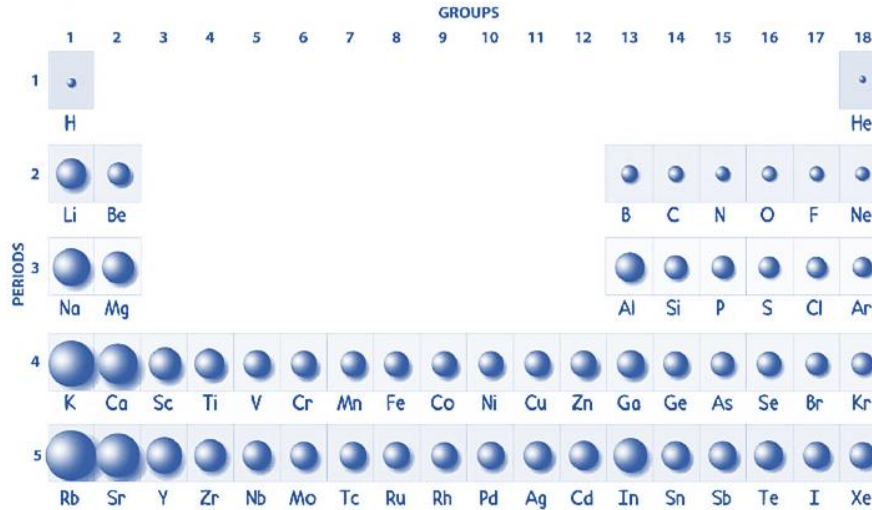


Figure 1-6 Periodic table with atomic radius feature [46].

1.4.2 Hydrogen degraded materials plasticity

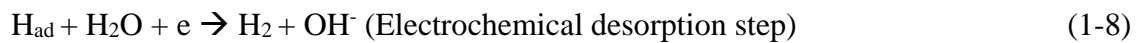
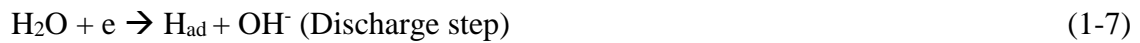
For more than a century, it has been well known that metals mechanical properties can be dramatically degraded by solute hydrogen. In 1875, Johnson [47] published the first documentary titled “*some remarkable changes produced in iron by the action of hydrogen and acids*” to depict the effect of hydrogen on the behaviour of premature failure of iron. He carried out the experiment by immersing the iron in acid for a few minutes, then a loss of plasticity of iron was observed:

“This change is at once made evident to any one by the extraordinary decrease in toughness and breaking strain of the iron so treated, and is all the more remarkable as it is not permanent, but only temporary in character, for with lapse of time the metal slowly regains its original toughness and strength” [47]

Following that, increasing investigations have shown that hydrogen can embrittle a variety of metals, such as nickel, titanium, aluminium, palladium etc. [5-12]. Terms of HE and HISC were introduced to depict materials premature failure due to materials plasticity degradation by hydrogen.

1.4.3 Introducing H into metals

Unlike the molecular structure of hydrogen gas, hydrogen atoms can be introduced into metals as solutes during manufacturing, processing and servicing. The manufacturing and processing, for example, casting and welding, involves solidification of metals where the hydrogen can be introduced from the atmosphere. This hydrogen source is significant in metals but the amount of such hydrogen is small. Compared with the hydrogen introduced during servicing, especially cathodic protection in the subsea environment, a large amount of hydrogen can be continuously generated and introduced into materials. The reaction steps in a neutral solution can be considered as follows [48]:



1.4.4 Diffusion of H in metals

Hydrogen can have a different level of concentration in parts of materials and the diffusion of hydrogen obeys Fick's laws. In this section, we introduce the Fick's laws and the effect of temperature on hydrogen diffusion.

1.4.4.1 Fick's first and second laws

Diffusion is driven by the chemical potential gradient. Under a steady state, the Fick's first law describes a diffusion of hydrogen from a region with high concentration to one with low concentration. The Fick's second law governs the diffusion, by which the change in concentration with time at a given point can be calculated.

$$J_x = -D \frac{dC}{dx} \quad \text{(Fick's first law)} \quad (1-10)$$

$$\frac{\partial C}{\partial t} = D \frac{\partial^2 C}{\partial x^2} \quad \text{(Fick's second law)} \quad (1-11)$$

where J is diffusion flux, defined as mass M diffusing through and perpendicular to a unit cross-sectional area of solid per unit of time. D is diffusion coefficient. x is distance and t is time of diffusion. C is the concentration of the diffusing species.

Ferrite and austenite behave dramatic differently on hydrogen diffusivity and solubility. Ferrite has an order of 10^{-11} m²/s for diffusion coefficient while it is 10^{-15} to 10^{-16} m²/s for austenite at room temperature [49-51].

In DSS and SDSS, a diffusion coefficient is reported between 10^{-14} m²/s and 10^{-15} m²/s [51]. An elevated 50°C temperature environment can give a greater hydrogen diffusivity. Askeland et al. [51] reported an approximately five times greater diffusivity can be achieved in 50°C temperature environment than it is in room temperature for some typical duplex stainless steels. Therefore, it can be assumed that the hydrogen diffusivity of SDSS is between 5×10^{-15} m²/s and 5×10^{-14} m²/s in a 50°C hydrogen charging environment. This hydrogen diffusivity will be applied to model the hydrogen concentration in this work.

The ferrite and austenite have a significant difference of hydrogen solubility. Nevertheless, few reports have been published regarding the solubility of ferrite and austenite in SDSS. Based on reference [50], it is assumed that ferrite saturates at 0.033 ppm while austenite saturates at 32.51 ppm

1.4.4.2 Solution of Fick's second law

The Fick's second law is used to model the hydrogen diffusion and concentration in a nonsteady-state diffusion system. The solution of the Fick's second law is shown as follows [52]:

$$\frac{C_x - C_0}{C_s - C_0} = 1 - \operatorname{erf}\left(\frac{x}{2\sqrt{Dt}}\right) \quad (1-12)$$

where C_x is the concentration of the diffusing atom at location x below the surface after time t ; C_0 is the initial uniform concentration of the diffusing atoms in the material; C_s is a constant concentration of the diffusing atoms at the surface of the material.

By rearrange the above equation, the concentration can be obtained by:

$$C_x = \left(1 - \operatorname{erf}\left(\frac{x}{2\sqrt{Dt}}\right)\right) \times (C_s - C_0) + C_0 \quad (1-13)$$

1.4.4.3 Hydrogen diffusion behaviour at elevated temperature

The diffusivity of species changes with temperature and can be estimated by:

$$D = D_0 \exp\left(-\frac{Q_d}{RT_K}\right) \quad (1-14)$$

where D_0 is a temperature-independent pre-exponential factor (m^2/s); Q_d is the activation energy for diffusion (J/mol); R is the gas constant which is measured as $8.31 \text{ J/mol}\cdot\text{K}$; T_K is absolute temperature (K).

Fast [53] reports values of D_0 in the range $0.076\text{-}0.22 \text{ mm}^2/\text{s}$ for ferrite and in the range $1.1\text{-}1.5 \text{ mm}^2/\text{s}$ for austenite. The related activation energy for lattice diffusion is given as 12.5 J/mol for ferrite and 42 J/mol for austenite.

1.4.5 Mechanisms of hydrogen embrittlement

Several established mechanisms have been proposed to account for HE, such as hydride-induced embrittlement [10, 54], hydrogen enhanced decohesion (HEDE) [55-61] and hydrogen enhanced local plasticity (HELP) [9, 62-64]. Hydride-induced embrittlement is only observed in some typical cases, which is not a general interpretation of HE. Here, we briefly review the mechanisms of HEDE and HELP, with supplementary of recent microscale mechanisms which are proposed based on large-scale atomic simulation.

1.4.5.1 Hydrogen enhanced decohesion

In the 1950s to 60s, Troiano et al. [55-57] proposed a mechanism HEDE to interpret HE. Follow-up major developments were progressed by Oriani and co-workers [58-61] on investigating the behaviour of hydrogen diffusion and trapping in metals. In this study, hydrogen was trapped and accumulated within the gaps of a lattice. A higher level of hydrogen was trapped within the lattice gaps under stress state which led to weakening of the lattice coherent bonding due to hydrogen atoms presence and thus crack initiation and propagation.

This mechanism has been applied to qualitatively interpret the experiments with pre-cracked specimens [9]. Figure 1-7 shows an example of samples crack opening behaviour in vacuum and hydrogen environment, respectively. This experiment result can be interpreted as hydrogen weakened the atomic bonding ahead of the crack tip. However, it appears HEDE mechanism has not fully convinced researchers as it is based on many assumptions and direct evidence is insufficient to support the proposed mechanism, i.e. no direct observation of decohesion of atomic bonds by hydrogen.

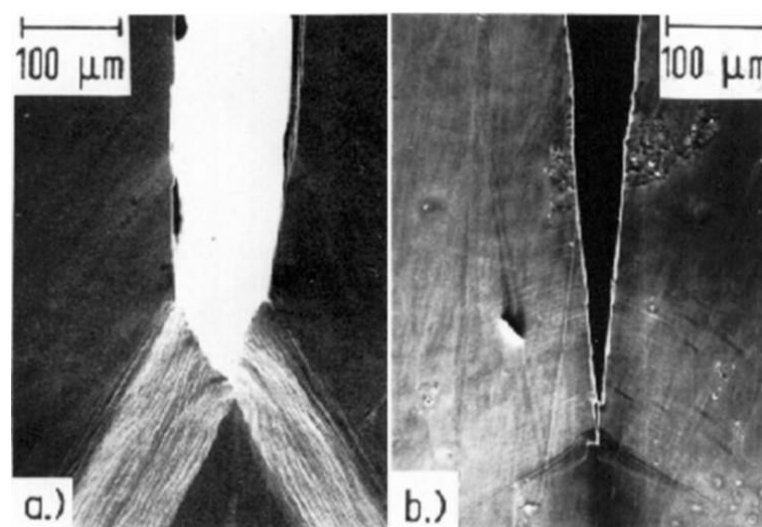


Figure 1-7 Different crack tip angle opening in Fe-3wt. %Si single crystal after straining in (a) vacuum and (b) hydrogen [9]

1.4.5.2 Hydrogen enhanced local plasticity

HELP was proposed based on the direct observation of dislocation pile-ups within hydrogen atmosphere using environmental TEM [62, 63] and a high density of slips lines at vicinity to fracture position [64]. Figure 1-8 reveals a typical pile-up of dislocation line in a hydrogen atmosphere by in-situ environmental TEM observation. These observations imply local plasticity can be enhanced with solute hydrogen, and thus leading to embrittlement.

However, some conflicts exist in HELP when interpreting materials deformation behaviour under tensioning, where the work hardening rate has no direct link with hydrogen [65]. Besides, this mechanism is not suggested by atomic modelling as there is no direct connection between HELP and actual embrittlement [66, 67].

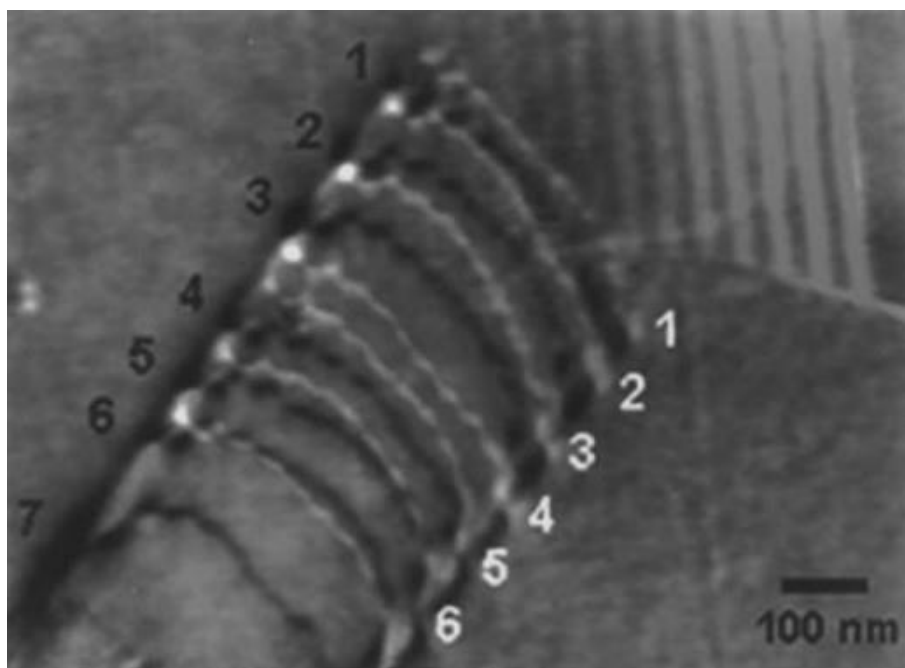


Figure 1-8 Observation of hydrogen induced dislocation pile-up (lines marked as overlapped grey lines), original dislocation position shown in black colour [62].

1.4.5.3 Hydrogen embrittlement on the atomic scale

With recent advances in using large-scale simulation and novel experimental methods, more features of hydrogen behaviour are understood on the atomic scale. Song et al. [67, 68] proposed an atomic scale HE mechanism by applying large-scale molecular dynamic simulation, schematic diagram shown in Figure 1-9. In this mechanism, dislocation emission ahead of a crack tip was inhibited by the presence of hydrogen atoms. Thus, a cleavage fracture is encouraged with hydrogen presence and thus leading to a brittle failure. Li et al. [69] studied the effect of hydrogen-vacancy complex on dislocations, where a stable hydrogen-vacancy structure is proposed in iron. Their following in situ TEM study revealed that hydrogen-vacancy structure has strong pinning effect on dislocation motion [70] (a short review of hydrogen-vacancy complex interaction is made in the Section 1.5.1). These studies are complementary and build-up a moderate framework on understanding hydrogen embrittlement on the atomic scale. Hitherto, due to the scale effect, this atomic-scale HE studies still require further investigation and exploration to bridge the HE behaviour from microscale to macroscale.

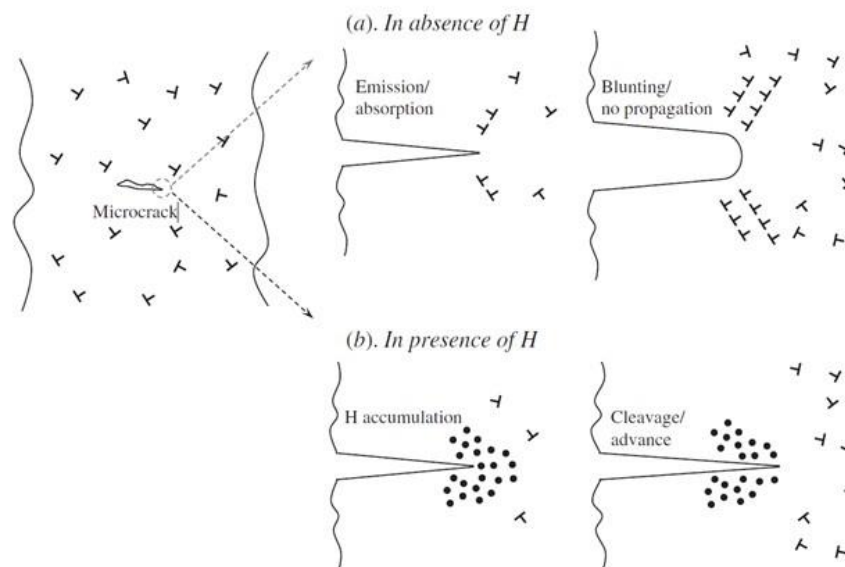


Figure 1-9 Illustration of micro-crack evolution during loading: (a) in the absence of H, blunting of crack tip impeded its propagation, and (b) in the presence of H, dislocation emission inhibited, leading to cleavage fracture [67].

1.5 Hydrogen-defects interaction

The above section discussed the mechanisms of hydrogen embrittlement in metals. The build-up of these mechanisms is based on the understanding of hydrogen-defect interaction. Defects have a high population in metals and they can be classified according to their dimension features as point defect, linear defect and interfacial defect. Simplest forms of point and linear defects are vacancy and dislocation, respectively. Interfacial defects contain grain boundaries, phase boundaries and stacking faults. The presence of such defects has effects on hydrogen trapping, diffusion and embrittlement.

1.5.1 Hydrogen-vacancy interaction

In metallic materials, one significant point defect are vacancies where an occupation atom is missing. It has been reported that hydrogen-vacancy interaction plays a crucial role in the behaviour of hydrogen embrittlement [69-73].

1.5.1.1 Thermal equilibrium of vacancy density

Vacancy defects are lattice sites which would be occupied in a perfect crystal, but are vacant. The equilibrium number of vacancies N_v is given by [32]:

$$N_v = N \exp\left(-\frac{Q_v}{RT}\right) \quad (1-12)$$

where N is the entropy factor within a range from 1 to 10 for most metals. Q_v is the formation enthalpy of mono-vacancy. R and T are gas constant and temperature, respectively.

1.5.1.2 Hydrogen-vacancy complex

Vacancies are widely and randomly spread in metals. With the hydrogen solute, some evidence has demonstrated the formation of hydrogen-vacancy complex plays a key role in hydrogen embrittlement [69-73]. In 2015, Li et al. [69] show a hydrogen-vacancy

complex is a stable form in α -Fe by molecular simulation. In 2016, Xie et al. [70] report that the hydrogenated vacancies are able to lock dislocations in aluminium using in-situ environmental TEM as shown in Figure 1-10. Such that, the hydrogen-vacancy may strengthen materials initially, but leading to a localization instability of plastic deformation when dislocation shakes off the pinning of hydrogen-vacancy complex. Thus, the release of plastic localization instability can contribute to a formation of microcrack.

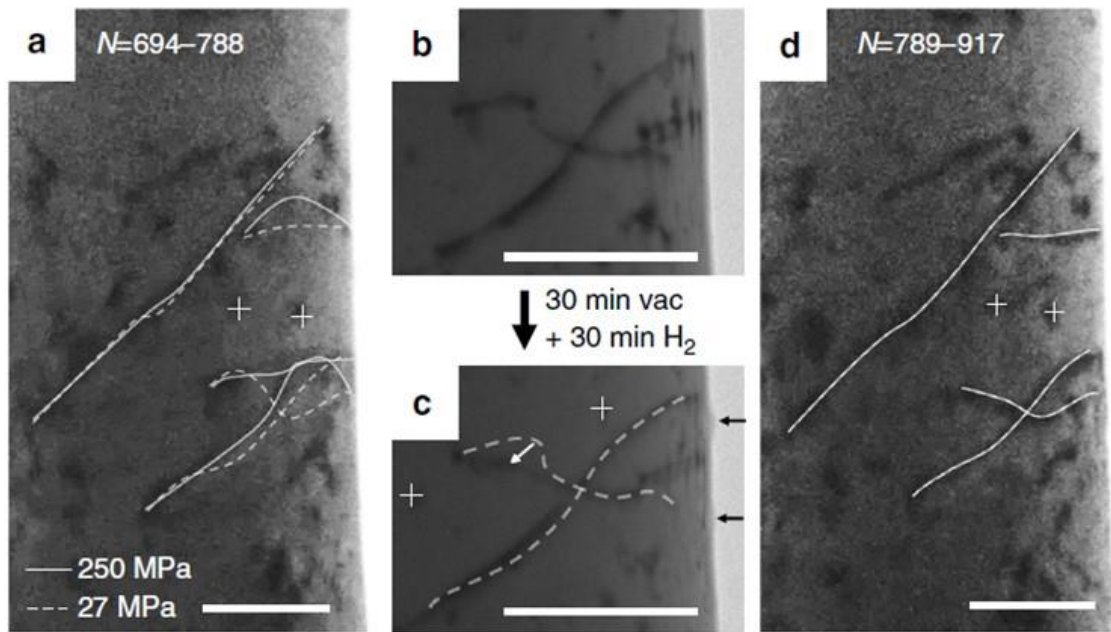


Figure 1-10 Effect of H-vacancy complex on dislocation movement; (a) dislocations movement by cyclic loads without hydrogenation, where four mobile dislocation lines were observed; (b) dislocations positions before hydrogenation and (c) after hydrogenation; (d) dislocation response to same cyclic load after hydrogenation. Scale bars stand for 200 nm [70].

1.5.2 Hydrogen-dislocation interaction

Dislocations are one of the common types of defect in materials. The materials plastic deformation can be driven by the movement of dislocations. It is important to understand the hydrogen-dislocation interaction. Although this interaction is not fully understood, the effect of hydrogen in materials on mobility, density and configuration of dislocation have been demonstrated.

1.5.2.1 Effect of hydrogen on dislocation mobility

Hydrogen has dual roles on dislocation mobility. On the one hand, dislocation mobility can be enhanced due to the dislocation line energy reduced by hydrogen solute. Wang et al. [74] reported a decreased activation energy to mobile dislocation which was measured by obtaining the plastic strain rate to calculate the ratio of mobile dislocations using in-situ hydrogen charging stress relaxation test. On the other hand, dislocation mobility can be decreased due to a concentration of hydrogen which exerts a drag effect on dislocation. Meanwhile, the sources of hydrogen-vacancy complexes can hamper the dislocation movement [70], which has been discussed in Section 1.5.1. Due to the dual effects of hydrogen on the mobility of dislocation, a simple conclusion is not possible to be draw as to whether hydrogen can increase or decrease the dislocation mobility.

1.5.2.2 Effect of hydrogen on dislocation density

In most common solution treated metals, intrinsic dislocation density ranges generally from 10^{10} to 10^{12} m^{-2} . Nonetheless, the intrinsic dislocation density can be changed by the presence of hydrogen. Using X-ray diffraction, Chen et al. [75] and Deutges et al. [76] showed that the presence of hydrogen can trigger dislocation multiplication in cold-rolled palladium, as shown in Figure 1-11. Barnoush et al. [77] reported that slip lines can arise on austenite surfaces during hydrogen charging. Figure 1-12 shows the images of slip line evolution on an austenite surface. From the Figure 1-12 (d), a slip line density of over 10^{13} m^{-2} can be estimated after 2.5 hours in situ hydrogen charging. This density is higher than the intrinsic dislocation density of 10^{12} m^{-2} in the solution treated sample.

These studies have shown the higher hydrogen concentration is able to activate the dislocation multiplication in crystalline materials. However, these studies have generally been limited to near-surface techniques, making it difficult to isolate the effect of dislocation-surface interactions.

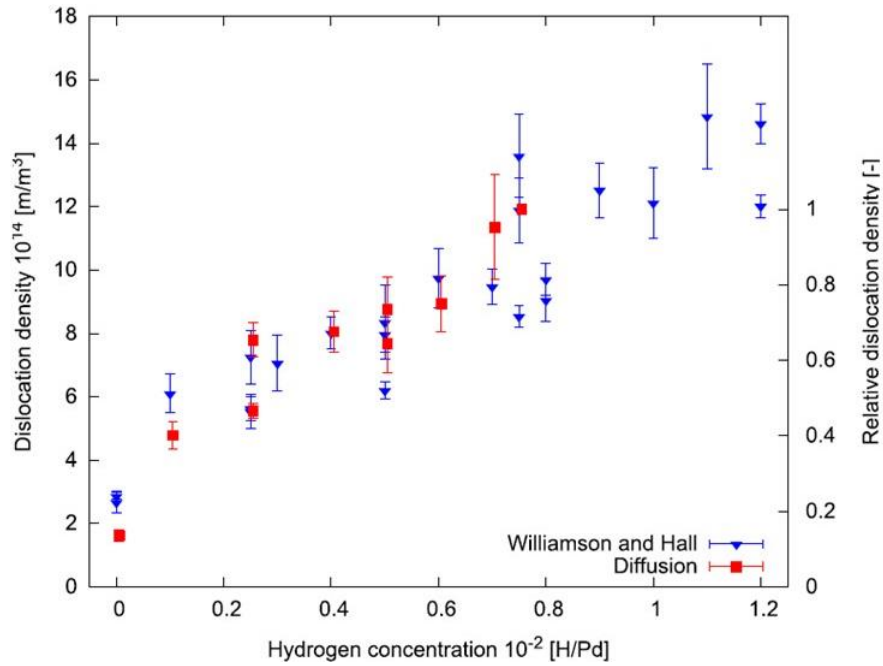


Figure 1-11 Evolution of the dislocation density of cold-rolled palladium with increasing hydrogen content during cold rolling. The measurements were performed by two different methods: interpretation of the diffraction patterns of the samples using the method of Williamson-Hall and measurement of the relative dislocation density by evaluating the diffusion time of hydrogen through the palladium samples.

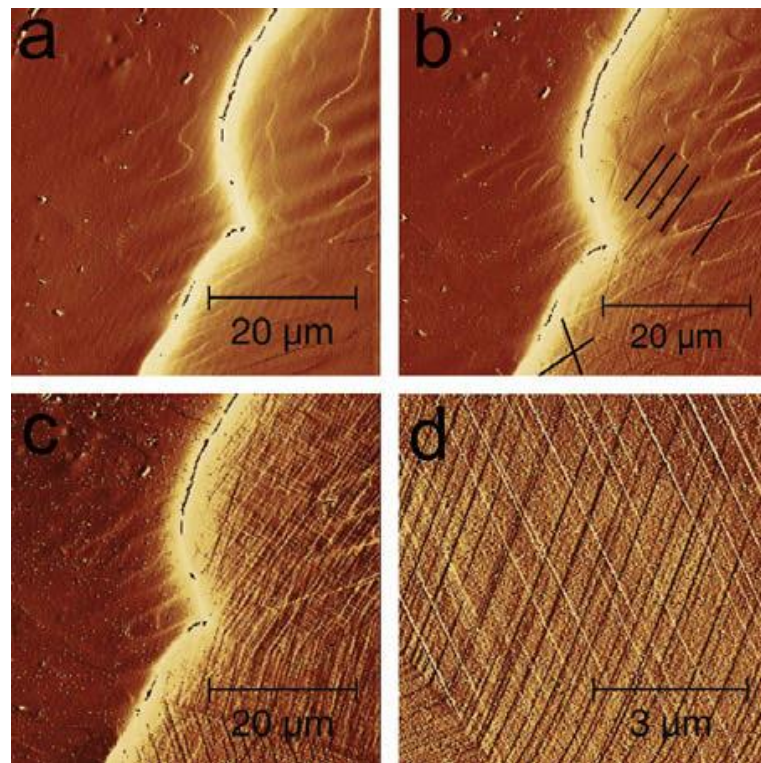


Figure 1-12 EC-AFM deflection mode images from the surface of the sample during in situ electrochemical H-charging. (a) Before H-charging at the OCP; on the left is a ferrite grain and on the right is an austenite grain which can be easily distinguished by its convex grain boundary. (b) The image of the same position after 1 h of in situ H-charging. (c) The image of the same position after 2.5 h of in situ H-charging. (d) Higher magnification image of the surface of the austenite grain. Images from reference [77].

1.5.2.3 Effect of hydrogen on dislocation configuration

The above Section briefly discussed the effects of hydrogen on dislocation mobility and density. Moreover, hydrogen can change the configuration of dislocations, more specifically, the position of dislocations. Deutges et al. [76] suggested that dislocations are likely to be distributed homogeneously in cold-rolled palladium with hydrogen solutes using transmission electron microscope, as shown in Figure 1-13. In contrast, Wang et al. [74] reported that the density of tangled dislocation increases with higher hydrogen concentration. This result suggests the repulsive interaction between dislocations gets weaker. In summary, although these two observations suggest a contradict trend of dislocation distribution, the configuration of dislocation can be changed by the presence of solute hydrogen.

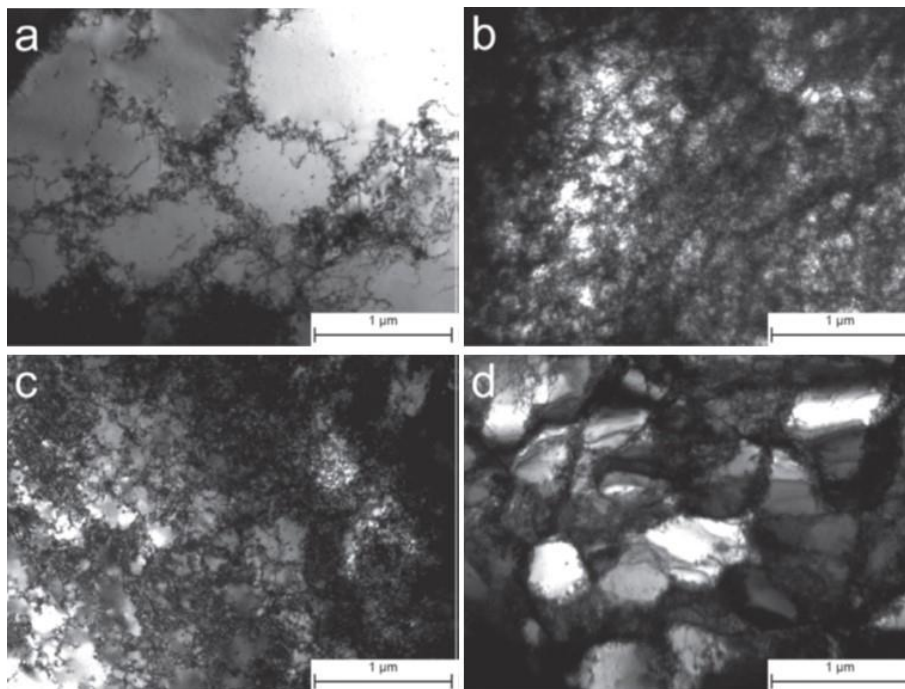


Figure 1-13 TEM micrographs of cold-rolled palladium without hydrogen (a) and with 0.1 at.% H/Pd (b), 0.5 at.% H/Pd (c) and 1.0 at.% H/Pd (d) during the cold rolling. Reduction in thickness: 50%. Cite from Ref. [76].

1.5.3 Hydrogen-boundaries interaction

A boundary is an interface between two grains or phases. The term “grain boundary” is used to define the interface between two grains while a phase boundary is the interface

between two distinct phases. For examples, in SDSS, the interface between two ferrite grains can be termed “ferrite grain boundary” while “phase boundary” can be defined to depict the interface between a ferrite and austenite grain.

Grain/phase boundaries are considered as preferential sites for diffusion and trapping of hydrogen [78-82]. In polycrystalline materials, when a finite fraction of lattice sites coincide between the two lattices, then one can define a coincidence site lattice (CSL). The relation between the number of lattice points in the unit cell of a CSL and the number of lattice points in a unit cell of the generating lattice is called Sigma (Σ). Stefano et al. [80] also reported that hydrogen trapping and diffusion strongly depend on CSL of grain boundary using first-principle calculation method. It is suggested that $\Sigma 3$ grain boundaries do not trap hydrogen and act as an obstacle for hydrogen diffusion, while $\Sigma 5$ grain boundaries are sinks for hydrogen atoms and can be fast diffusion channels for hydrogen migration. Sobol et al. [82] reported that a high hydrogen concentration can be detected at grain/phase boundaries in DSS using advanced time-of-flight (TOF) secondary ion mass spectrometry. These reports show boundaries are critical for hydrogen diffusion and trapping in polycrystalline materials.

1.6 Development of transmission Kikuchi diffraction

1.6.1 Background of EBSD

EBSD is a microstructural-crystallographic characterisation technique to study metals. For example, EBSD is able to identify phases and furthermore map phase distributions [83]. Also, an EBSD scan can provide the crystal orientation information in polycrystalline materials, which helps to understand the recrystallizations, twinning, boundary migration, and deformation behaviours [39, 84-88].

The application of EBSD has many advantages. First, EBSD requires bulk samples which can easily be prepared. Second, EBSD is fast for phase characterisation as a large region can be automatically scanned. Lastly, EBSD is easily available compared with other facilities such as X-ray diffractometer and TEM. Although EBSD owns many advantages, one major drawback is the spatial resolution which is limited to about 50 nm. Therefore, EBSD cannot be applied at the nanoscale.

1.6.2 Transmission Kikuchi diffraction

Transmission Kikuchi diffraction (TKD) is a relatively new technique which is developed from EBSD technique [89-93]. In EBSD, the Kikuchi diffraction patterns are a consequence of diffraction within a subsurface interaction volume in bulk material [94, 95]. As a result, the spatial resolution is restricted to approximately 50 nm [84, 96-100]. However, by transmitting the beam through the sample, as in TKD, the interaction volume is restricted to a narrow 'slice' of material, such that the spatial resolution limits imposed by EBSD do not apply.

The principal experimental set-ups for both EBSD and TKD are shown in Figure 1-14. TKD provides microstructural information by analysing transmitted Kikuchi patterns through a thin foil that is smaller in width than the electron beam interaction volume observed in thick (i.e. bulk) samples. Since the TKD interaction volume transverse to the thin foil is comparable to the thin-foil width, the typical full 'tear-drop' shaped interaction volume of SEM microscopy is not realised. The excitation volume (the portion of the interaction volume that is responsible for the pattern forming electrons) is, therefore, bound by the free surface through which the backscattering electrons are transmitted. Although the diameter of the beam spot on the sample surface is not critical in the resolution limit, the lower tilt angles employed in TKD (typically 20°) mean that of the excitation volume has a less elliptical shape compared with EBSD where samples are typically tilted to 70°.

In practice, the spatial resolution of TKD has been reported to be between approximately 2 nm to 10 nm [89-92, 95].

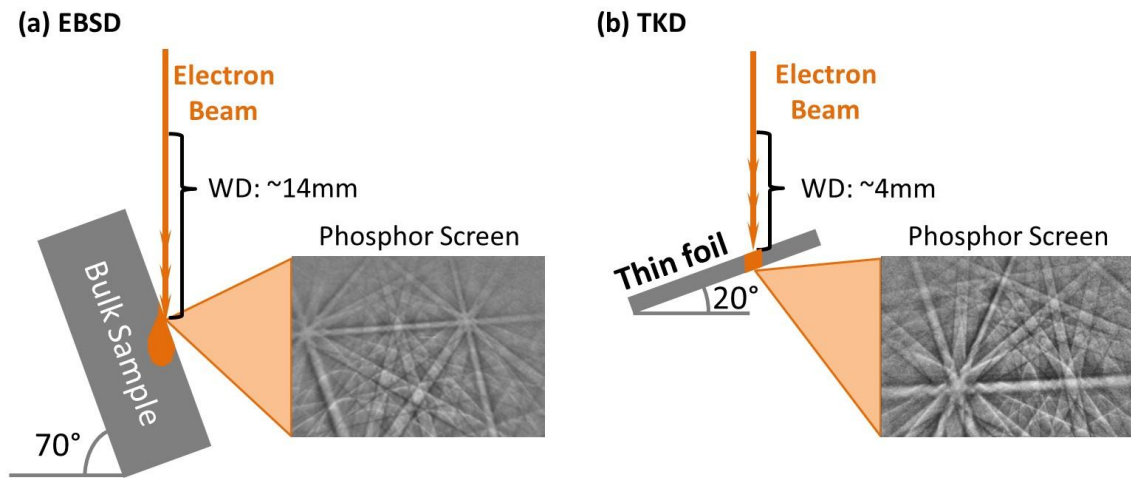


Figure 1-14 Principle set-up of (a) EBSD and (b) TKD [89-93].

1.6.3 General applications of SEM-TKD

1.6.3.1 Phase characterisation of nanocrystalline and ultra-fine-grained materials

TKD possess high spatial resolution which can be down to several nanometres. This superior feature provides TKD as a suitable tool for characterising nanocrystalline materials. Figure 1-15 shows a TKD result on phase map of a duplex stainless steel [101]. The distribution of ferrite and austenite are shown and the grain size is in order of tens of nanometres.

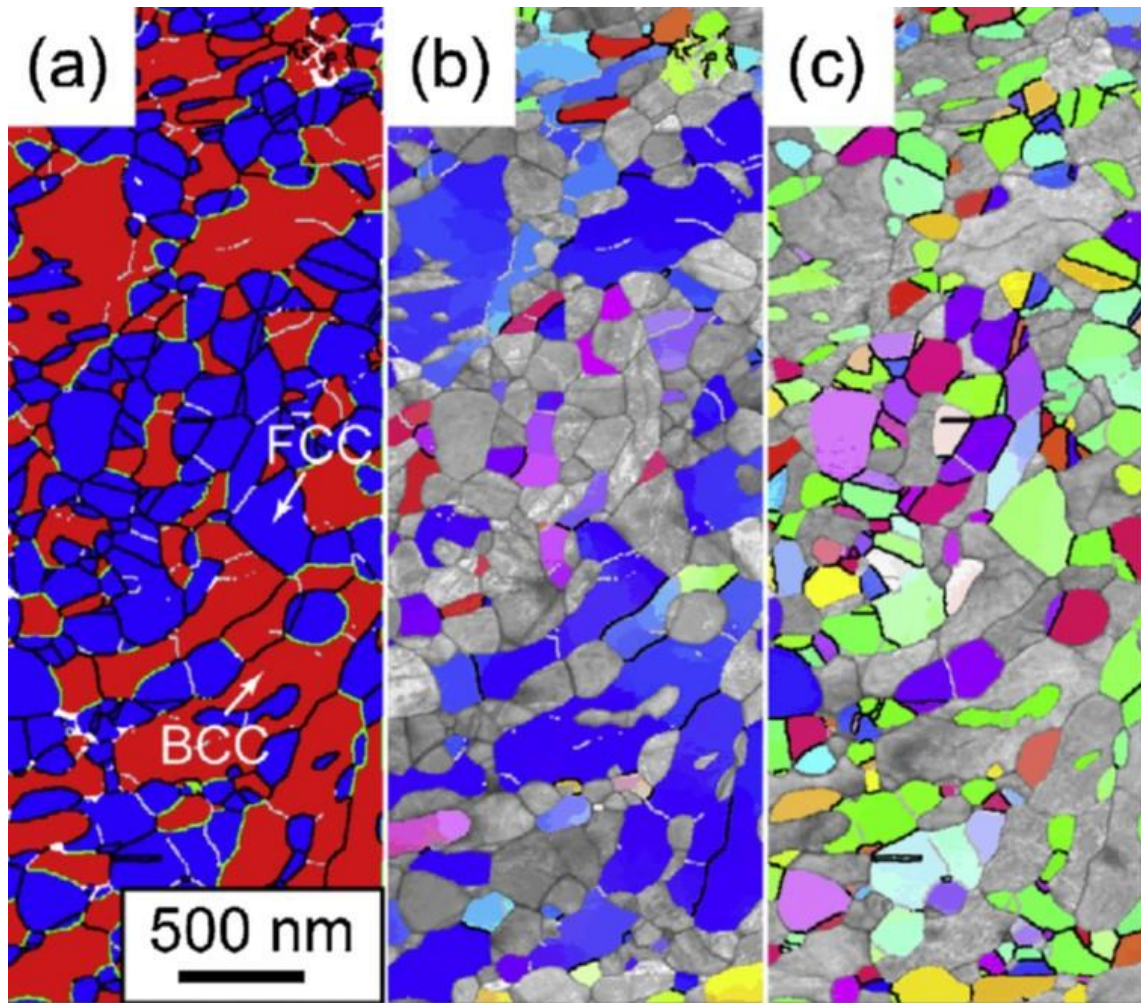


Figure 1-15 TKD results of a duplex stainless steel (a) phase map; IPF-z plot of (b) ferrite and (c) austenite [101]

1.6.3.2 Twin boundary distribution in a highly deformed alloy

When grains have lower than a hundred-nanometre grain size, these grains are beyond the characterisation capability of EBSD. Figure 1-16 shows one case where TKD is applied to characterise the twin boundary structure in a highly deformed titanium alloy [102]. Several featured grains are in nano size. Here, the presence of nano twin boundary and nano twin boundary segments are successfully mapped using TKD method.

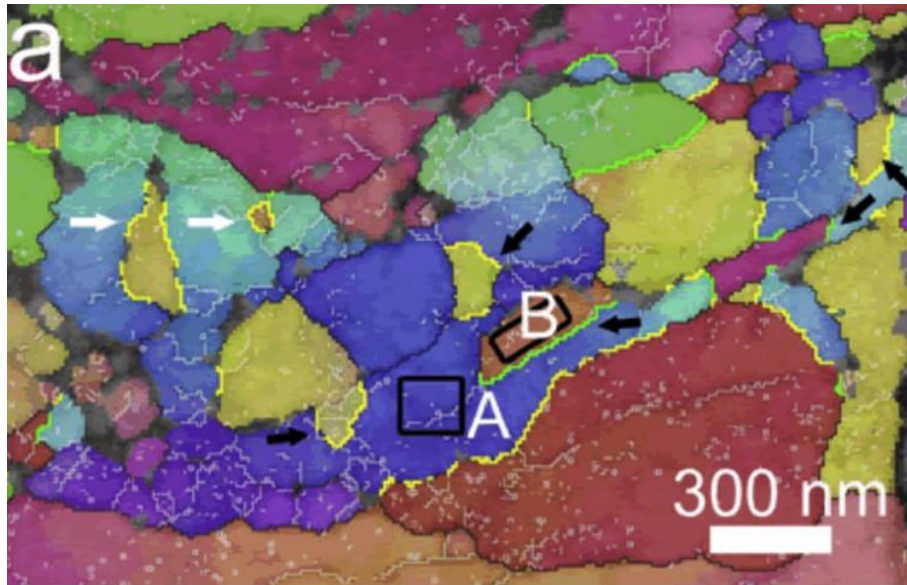


Figure 1-16 Orientation map of an ultra-fine grained titanium alloy; the black and white arrows indicating twin boundaries and twin boundaries segments [102].

Chapter 2

Experimental methods

In this chapter, detail of sample preparation, equipment and methodology will be given.

Section 2.1 details the preparation of samples;

Section 2.2 details the equipment used in this study;

Section 2.3 details the methods of modelling and experiment.

2.1 Sample preparation

2.1.1 Samples used in Chapter 3

SDSS samples used in Chapter 3 were prepared from two raw SDSS materials: one was extracted from a SDSS pipeline and another one was machined from a SDSS multi-pass weldment.

2.1.1.1 SDSS pipeline sample

The SDSS pipeline material used in this study was extracted from a UNS S32760 (Zeron 100) pipeline. Table 2-1 shows the chemical composition of SDSS pipeline sample. Samples were machined as 10×10×10 mm³ pieces for heat treatment. Solution heat treatment was performed at 1200°C for 1 hour followed by water quenching. This heat treatment was applied to remove residual stresses and to homogenise the material's microstructure. To study the phase transformation in SDSS, annealing at 800°C was applied on three SDSS samples with isothermal holding times of 6 min, 30 min, and 60 min followed by water quenching.

Table 2-1 Chemical composition of SDSS pipeline sample

Sample	Elements, wt. %								
	C	Si	Mn	P	S	Cr	Mo	Ni	Al
Pipeline	0.020	0.450	0.490	0.022	0.002	24.700	3.650	6.800	--
	As	Co	Cu	Nb	Sn	Ti	V	W	N
Pipeline	--	--	0.72	--	--	--	--	0.7	0.23

SEM samples were polished down to 0.04 µm colloidal silica. The surface of EBSD samples were ground down to 0.04 micron, followed by electron polishing using 10 wt. % HClO₄ alcohol solution at 45 V potential for 5 seconds. During electron polishing, the sample was connected to anode whilst a platinum wire was connected to cathode.

To prepare TEM samples, preliminary machining was conducted using electro-discharge wire machining, before mounting and incremental grinding to a thickness of approximately 100 µm. A 3 mm diameter foil was punched out from the 100µm thick sheet for further

thinning. Double-jet polishing with a solution consisting of 5 wt.% perchloric acid and 95 wt.% ethanol was used, before final thinning using ion milling with a 2° beam angle for 1 hour.

2.1.1.2 SDSS weldment sample

SDSS weldment sample was machined from a multi-pass welded joint. Figure 2-1 shows photomicrograph of the welded super duplex stainless steel joint in the etched condition. The grade of flange is UNS S32750 (SAF 2507) and the grade of pipe structure is UNS S32760 (Zeron 100). Table 2-2 shows the measured chemical composition of this weldment sample. A piece of TEM sample was machined from the HAZ on the flange side, as pointed by double dashed lines in Figure 2-1. The preparation procedure of TEM sample is same with the procedure detailed in Section 2.1.1.1.

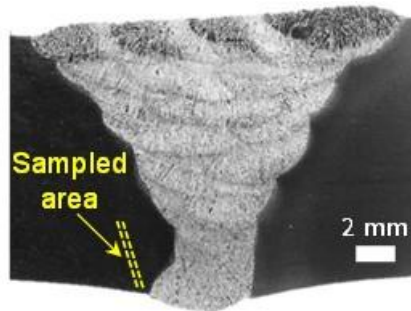


Figure 2-1 Photomicrograph of the welded super duplex stainless steel joint in the etched condition. A thin foil sample was machined from the heat-affected zone on the forging side of the joint.

Table 2-2 Chemical composition of SDSS weldment sample

Sample	Elements, wt. %								
	C	Si	Mn	P	S	Cr	Mo	Ni	Al
Flange	0.014	0.300	0.320	0.021	<0.002	24.900	3.830	6.800	0.030
Weld	0.014	0.390	0.680	0.029	0.004	25.000	3.860	8.800	<0.01
Pipe	0.032	0.540	0.720	0.019	0.009	25.100	3.560	7.000	<0.01
	As	Co	Cu	Nb	Sn	Ti	V	W	N
Flange	<0.01	0.030	0.110	<0.01	<0.005	<0.005	0.110	<0.05	0.283
Weld	<0.01	0.070	0.630	0.010	0.007	<0.005	0.050	0.520	0.210
Pipe	<0.01	0.080	0.820	0.040	<0.005	0.007	0.050	0.680	0.270

2.1.2 Samples used in Chapter 4

2.1.2.1 Raw tensile sample preparation

The raw tensile specimens were prepared from SDSS bulk pipeline material (chemical composition tabled in Table 2-2). Figure 2-2 shows a schematic representation of sample machining from the SDSS pipeline material and Figure 2-3 shows the dimension of these samples (gauge volume $35 \times 5 \times 1.2 \text{ mm}^3$). Tensile specimens were solution heat treated at 1200°C for 1 hour followed by water quenching. Sample surfaces were ground with emery paper down to 1200 grit.

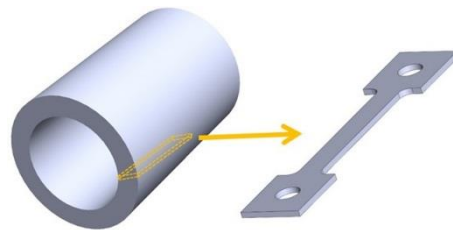


Figure 2-2 Schematic representation of sample machining from a raw pipe structure.

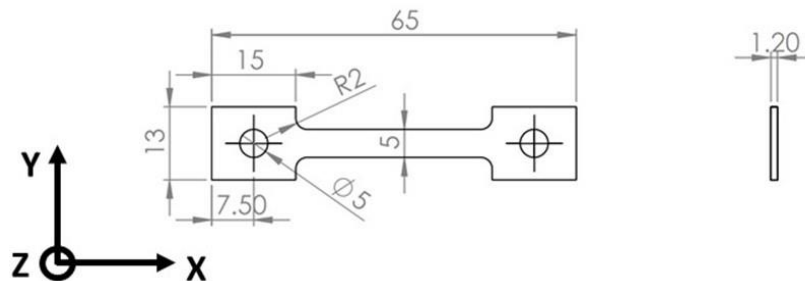


Figure 2-3 Dimensions of tensile sample; direction of x is longitudinal, y is radial and z axis is hoop; unit in mm.

2.1.2.2 Pre-straining

Three different pre-strained samples were prepared by applying 5%, 10% and 15% plastic pre-strain with a tensile strain rate of 10^{-3} s^{-1} , while unstrained samples were used as references for neutron diffraction. Figure 2-4 shows a tensile curve of the machined tensile sample and the target forces which were set to obtain pre-strain. Eight samples were prepared in total, as tabled in Table 2-3.

Table 2-3 Prepared samples in this study

Pre-strain (%)	0	5	10	15
H-free	hf-0	hf-5	hf-10	hf-15
H-charge	hc-0	hc-5	hc-10	hc-15

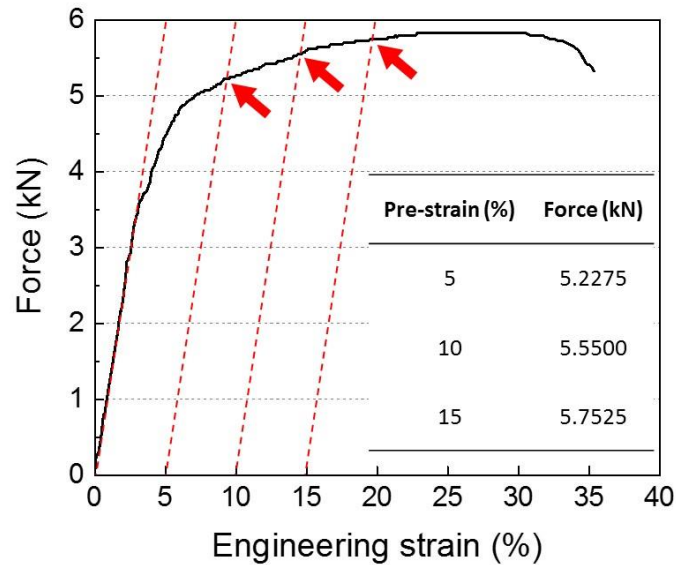


Figure 2-4 Tensile curve of sample engineering strain (%) against force (kN); the pre-strain of 5%, 10% and 15% can be achieved with 5.2275, 5.5500 and 5.7525 kN loads; uncertainty of pre-strain is measured as 0.3%.

2.1.2.3 Hydrogen charging

Samples were connected to a cathodic lead and immersed into 3.5 wt. % NaCl solution, whilst platinum wire was connected to a positive lead. Figure 2-5 shows the setup of this cell. A 50°C heating environment was created for both solution and samples to facilitate hydrogen diffusion into materials. Hydrogen charging was applied for 10 days with a 25 ± 5 mA/cm² current density.

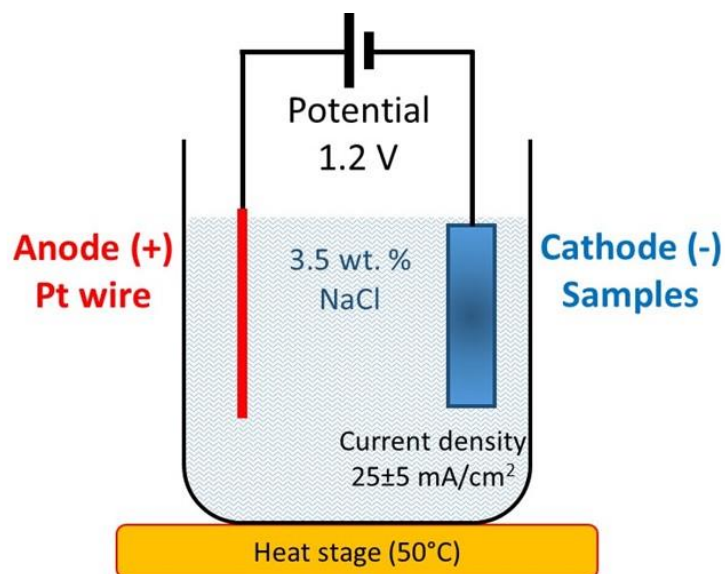


Figure 2-5 Schematic representation of hydrogen charging cell.

2.1.3 Samples used in Chapter 5

2.1.3.1 Sample preparation

Samples used in Chapter 5 were prepared as tensile sample whose dimensions and preparation routines are detailed in Section 2.1.2.1. Method of hydrogen charging is detailed in Section 2.1.2.3. Before the EBSD characterisation, the sample surface was further polished down to 0.04 micron, followed by electron polishing whose procedure is detailed in Section 2.1.1.1. A final 1-hour ion milling was performed to clean up sample surfaces by applying 5 keV with 7.0° gun tilt.

2.1.3.2 Slow strain rate test

Slow strain rate tests were carried out in Engin-X, ISIS, using a custom-built Instron stress rig with a maximum loading capability of 100 kN. The slow strain rate test was performed with a strain rate of 10^{-4} /s.

2.2 Equipment

2.2.1 Equipment used in Chapter 3

2.2.1.1 Scanning electron microscopy

Two models of scanning electron microscope (SEM) were used. A FEI Sirion 200 with an energy dispersive x-ray spectroscopy (EDS) detector was used for imaging in this Chapter. A TESCAN LM Mira 3, coupled with an EDS detector and an OXFORD Instrument EBSD detector, was used for EBSD and TKD characterisation.

2.2.1.2 Electron backscatter diffraction

OXFORD Instrument EBSD detector in a TESCAN LM Mira 3 SEM was used for EBSD characterisation. A sample tilt of 70° was setup during characterisation at accelerate voltage of 30 keV. A scanning step size of 100 nm was chosen and 2 by 2 EBSD screen binning was applied. These setups were applied by considering the quality of result and time efficiency.

2.2.1.3 Transmission Kikuchi diffraction

Similar with EBSD, TKD was performed using an OXFORD Instrument EBSD detector in a TESCAN LM Mira 3 SEM. Rather than applying a 70° sample tilt in EBSD, a 20° sample tilt was applied in TKD. This tilt was achieved using a custom-built pre-tilt holder for TKD. Scanning step sizes of 20 nm and 50 nm were applied for characterisation of Cr₂N and sigma phase, respectively. A screen binning scheme of 2 by 2 was applied. These setups were applied by considering the quality of result and time efficiency.

2.2.1.4 Transmission electron microscopy

TEM observation was performed on a JEOL 2100F at 200 kV coupled with EDS and STEM detectors. A double tilt sample holder was engaged to rotate the sample in the TEM.

2.2.1.5 Ion milling

Ion milling was applied for all TKD and TEM samples used in this study. Precision ion polishing system Gatan Model 691 and Leica EM RES102 were used.

2.2.2 Equipment used in Chapter 4

Time-of-flight (TOF) neutron diffraction experiments were performed on the ENGIN-X neutron diffractometer, ISIS, UK [103]. Figure 2-6 shows the schematic set-up of the neutron diffractometer in ENGIN-X. To conduct the experiment, the focused neutron beam fires to the sample and the diffracted signals are collected by two detectors which cover a range of horizontal $90\pm 14^\circ$ and a vertical $\pm 21^\circ$. A $4\times 4\times 2\text{ mm}^3$ instrumental gauge volume was set for neutron signal collection.

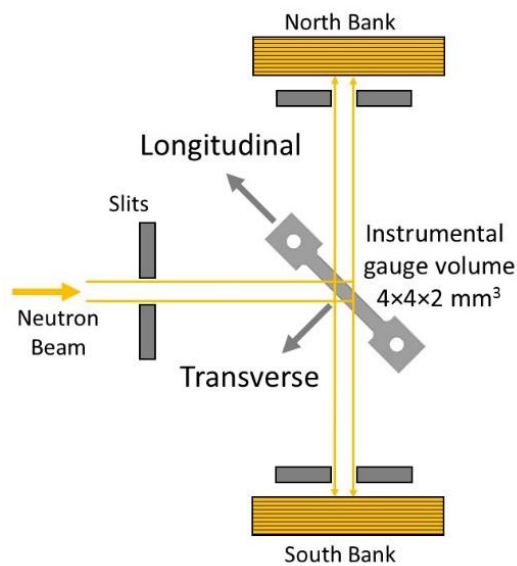


Figure 2-6 Neutron diffraction set-up in ENGIN-X, ISIS, UK [103].

2.2.3 Equipment used in Chapter 5

TESCAN LM Mira 3 coupled with EDS detector and OXFORD Instrument EBSD detector was used for SEM imaging and EBSD characterisation.

2.3 Methodology

2.3.1 Modelling of phase transformation

Evolution of phases can be calculated by the Calphad method. The Calphad stands for calculation of phase diagram and it has become a popular method for thermodynamic simulation [104]. The modelling of Calphad is based on the law that attains the lowest Gibbs energy with a given composition, temperature and pressure conditions [104]. Such that, the application of Calphad can model solidification behaviour and stable/metastable phase transformations.

A variety of packages has been developed to calculate the materials phase diagram. Thermo-Calc comes with well-developed databases to calculate the equilibrium phase diagram, moreover, the add-on package of Dictra can simulate the element diffusion process [105]. JMatPro can not only calculate equilibrium phase diagrams but also the TTT and CCT diagrams for a variety of alloys [106].

In this Chapter, Thermo-Calc (TCFE6 database) was used to calculate equilibrium phase diagram (chemical composition listed in Table 2-1 was applied). Dictra (MOBFE2 database) was used for diffusion simulation. The chemical compositions of Cr, Ni, Mo and Fe (balance) were applied for the Dictra simulation according to Table 2-1. JMatPro 8.0 was used to calculate time-temperature-transformation (TTT) diagrams and continuous cooling transformation (CCT) diagrams (chemical composition listed in Table 2-1 was applied).

2.3.2 Using neutron diffraction to measure dislocation density in Chapter 4

2.3.2.1 Advantages of using neutron diffraction technique

Neutron diffraction has its own advantages compared with X-ray diffraction method. The neutron diffraction can be a complementary method of X-ray diffraction for determining

lattice or molecular structure owing to the high penetration capability of the neutron beam. As neutron has high penetration capability, the lattice structure deep inside materials can be analysed. For example, the bulk samples stereo residual stress analysis can be achieved using neutron diffraction. Besides, neutrons interact with matter differently to x-rays. While the intensity of X-ray diffraction is dependent of atomic number of element, i.e. a high intensity with heavier element, neutrons interact directly with the nucleus of the atom. Thus, the neutron diffraction is sensitive to scatter materials with lower atomic number atoms.

2.3.2.2 Time-of-flight neutron diffractometry

The neutron beam sources can be classified as monochromatic or white beams. The monochromatic neutron beam is confined to an extremely narrow range of neutron flight time. Compared with a monochromatic neutron beam, the white neutron beam source introduces neutrons within a range of flight time. Therefore, this diffraction technique is sometimes termed as Time-of-Flight (TOF) neutron diffraction.

TOF technique is a general method for determining the kinetic energy of a traveling neutron by measuring the time it takes neutrons to fly between two fixed points whose distance is known. To observe the diffraction of a given wavelength of radiation, the Bragg diffraction condition must be satisfied, as shown in Figure 2-7. The Bragg's Law defines:

$$\lambda = 2d_{hkl} \sin \theta \quad (2-1)$$

where λ is neutron wavelength; d_{hkl} is interplanar spacing; θ is scattering angle.

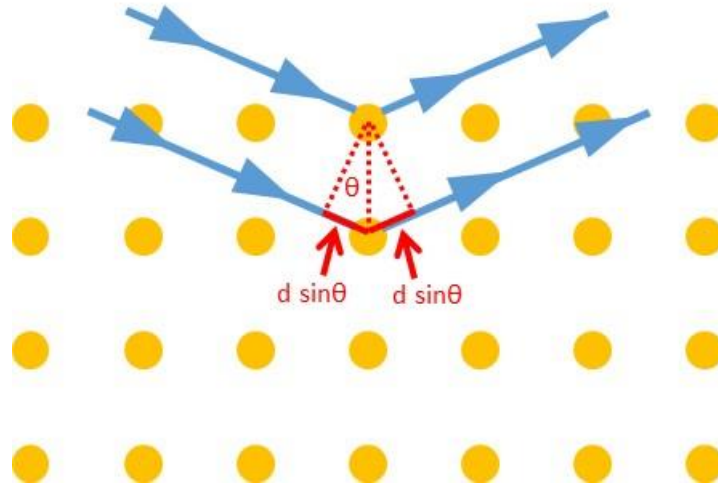


Figure 2-7 Schematic diagram of Bragg diffraction

In TOF neutron diffractometry, the wavelength of the neutron corresponding to its flight time t over a distance L is given by:

$$\lambda = ht/(m_n L) \quad (2-2)$$

where h is Planck's constant, m_n is neutron mass. Combining the above two equations, the relation between flight time and interplanar spacing can be determined as:

$$t = 2m_n L/h \times \sin \theta \times d_{hkl} \quad (2-3)$$

Thus, the diffraction peaks can be observed when the interplanar spacing satisfy the above equation.

2.3.2.3 Determination of dislocation density by TOF neutron diffraction

In 1955, Williamson et al. [107] developed a model to measure the dislocation density using X-ray spectrometry. Based on this principle, in 2013, Christien et al. [108] proposed a dislocation density measurement method for neutron diffraction, which has been successfully applied to calculate dislocation density in a range of materials [109-111]. In 2015, Christien et al. [112] modified the materials elastic energy using the Faulkner equation to give a more accurate estimation comparing with other experimental

measurement methods. In this study, this modification is adopted and a brief derivation process is described here.

The peak broadening Δd of neutron diffraction is related to interplanar d spacing, grain size t and elastic strain ε according to Williamson-Hall equation [113]:

$$\frac{\Delta d}{d} = \frac{d}{t} + \varepsilon \quad (2-4)$$

The peak broadening is usually determined by the increase of full width at half maximum (FWHM). In Equation 2-4, the grain size term d/t contributes an approximately 10^{-5} for the overall peak broadening ratio $\Delta d/d$ with an average size of tens of micron grain size in SDSS in this study. By comparison, the overall peak broadening ratio $\Delta d/d$ is in the order of 10^{-3} , which is much larger than the grain size term d/t contribution. Therefore, the overall peak broadening $\Delta d/d$ can be approximately equal to the elastic strain term ε :

$$\frac{\Delta d}{d} = \varepsilon \quad (2-5)$$

The total elastic energy U stored in the material can be calculated using the Faulkner equation [114]:

$$U = \frac{15}{4} \frac{E}{(1+\nu)} \varepsilon^2 = \frac{15}{4} \frac{E}{(1+\nu)} \left(\frac{\Delta d}{d}\right)^2 \quad (2-6)$$

where E is Young's modulus and ν is Poisson's ratio. The elastic energy per unit length of dislocation (u) can be estimated using the following equation for both edge and screw dislocations [115]:

$$u = \frac{Gb^2}{4\pi} \ln \frac{r_1}{b} \quad (2-7)$$

where G is shear modulus, r_1 is the effective elastic field radius at a dislocation core and b is the burger's vector. For SDSS, some parameters can be assumed that $r_1=100$ nm,

$b=0.248$ nm for ferrite and $b=0.254$ nm for austenite. As the value $\ln \frac{r_1}{b} \approx 2\pi$, the dislocation density can be derived from the Equation 2-6 and Equation 2-7, giving Equation 2-8:

$$\rho = \frac{U}{u} = \frac{15E}{2Gb^2(1+\nu)} \left(\frac{\Delta d}{d}\right)^2 \quad (2-8)$$

Typical values of $E/G=2.5$ ($E=200$ GPa, $G=80$ GPa) and $\nu=0.3$ are applied for both austenite and ferrite in this study. The standard peak width reference was obtained from the hydrogen free unstrained sample. In general, an intrinsic 10^{12} m^{-2} dislocation density can be assumed for standard peak width. The peak width can be quantified by the measurement of FWHM. The FWHM can be measured by a variety of methods. Among these methods, a Voigt scheme is one accessible and accurate method to measure the FWHM. The FWHM measurement by Voigt scheme is a built-in function in single-peak-analysis of OpenGENIE program whose programming detail can be found in reference [116].

2.3.3 Using TKD to measure geometrically necessary dislocation in Chapter 5

2.3.3.1 Notion of GND

Dislocation is classified into two types: statistically stored dislocations (SSD) and geometrically necessary dislocations (GND) [100, 117-122]. In 1953, Nye [118] proposed a basic theory to link the strain gradient with the dislocation density, where relevance of GND to strain gradient was firstly suggested. Further work by Ashby [121] gave a material deformation based GND notion, stating: “*the gradients of deformation require that dislocations be stored...*”. Quantification of GND density is drawing more attention after knowing a number of dislocations is closely associated with the materials microstructure change and/or deformation behaviour [100, 118-121].

2.3.3.2 Calculation scheme of GND: from EBSD to TKD

Quantification of GND density on mesoscale has been achieved using EBSD [97, 100, 122-125]. One popular method to obtain GND density value from EBSD is using KAM from EBSD result. KAM values are obtained directly from EBSD map pattern data, which is a popular method to measure the local misorientation. As for TKD, the same principle can be applied to GND measurement by using KAM values which is obtained from TKD map data. Figure 2-8 shows a schematic diagram of KAM averaging procedure. A KAM value is calculated by averaging crystal orientation differences between the host pixel and adjacent neighbouring pixels. In this study, schemes of the first order (3×3 pixel) and second order (5×5 pixel) KAM maps were used to study the local misorientation. The difference in orientation between the host pixel and neighbouring pixel above 2° is excluded in the calculation. This 2° was suggested to distinguish the host grain from adjacent grains [97].



Figure 2-8 A schematic diagram of the KAM measurement. For the first order (i.e. 3×3 pixel) measurements, the local orientation is calculated between the host pixel (in red) and the nearest pixels (in yellow). Similarly, the second order (5×5 pixels) measurement of KAM will be calculated between the host pixel and the nearby pixels in both blue and yellow.

Kubin and Mortensen's model [126] was applied to quantify GND density from KAM values. The Kubin and Mortensen model assumes that a series of twist sub-grain boundaries was assumed in the cylinder to correlate the GND density ρ_g with the misorientation angle

θ . A pair of perpendicular arrays of screw dislocations was also assumed to accompany the two twist sub-grain boundaries. Thus, the following equation can be used to calculate the GND density from KAM:

$$\rho_{gnd} = \frac{2\theta}{bd_{GND}} \quad (2-9)$$

where θ is the misorientation curvature; b is Burgers vector, an estimation of 0.248 nm is made for ferrite and it is 0.254 nm for austenite; d_{GND} is the unit length.

2.3.3.3 Potentials and advantages of TKD-GND application

As a first step to apply TKD on dislocation detection, a comparison is made here between TKD-GND and some well-established dislocation detection methods with respect to dislocation detection range and spatial resolution. Figure 2-9 shows a comparison between TKD-GND and these methods. For bulk samples, the methods of X-ray and neutron diffraction have been widely applied to measure the dislocation density in-situ or ex-situ with probe size from hundreds of microns to several millimetres [75, 76, 108, 127, 128]. Dislocation detection with finer spatial resolution can be achieved by quantifying the dislocation etch pits (DEP). However, this is an imprecise method to determine the dislocation density based on the observation of etch pits by acidic etching on a clean sample surface [129]. EBSD can be used to measure the GND density with the probe size limited to about 100 nm [97, 100, 122-125, 130], while TEM is capable to visualise dislocation lines and thus quantify dislocation density at the nanoscale [44, 62, 74, 131, 132]. However, a spatial resolution-detection gap exists, as shown in Figure 2-9. Therefore, the development of the TKD technique can effectively fill the gap between EBSD and TEM: the GND density distribution at the nanoscale can be effectively characterised using the TKD-GND method. By taking the advantage of TKD, it is proposed that the TKD-GND method can be further applied to characterise GND in highly deformed ultrafine grains, martensitic materials and nanocrystalline materials at the nanoscale [37-43].

Experimental methods for dislocation detection

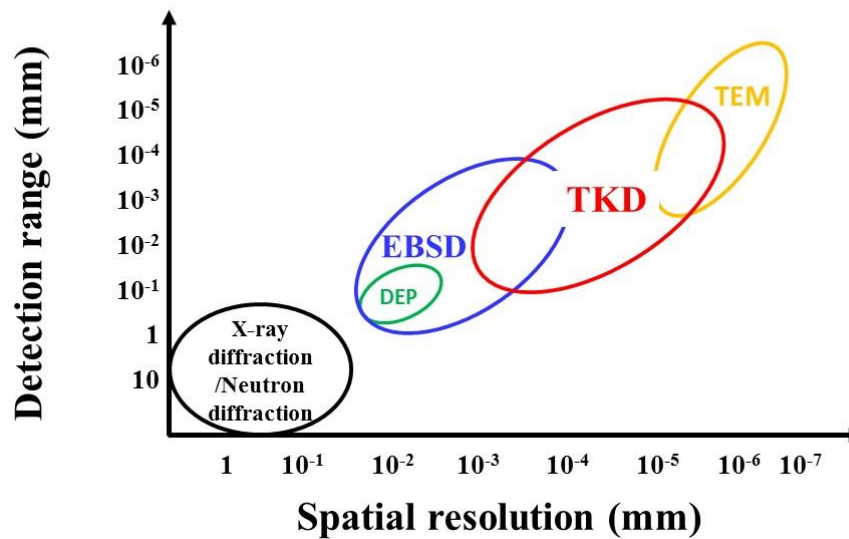


Figure 2-9 Experiment methods for dislocation detection [44, 62, 74, 97, 100, 122-125, 129-132].

2.3.3.4 Spatial resolution and uncertainty of TKD-GND measurement

TKD has been shown to have a spatial resolution on the scale of 2 to 10 nm [89-92, 95]. Although the spatial resolution of TKD can vary depending on materials, thicknesses, and quality of sample preparation in the scanned area, the high spatial resolution of TKD technique has given rise to the development of the TKD-GND density measurement method.

When employing a TKD-GND method, the accuracy of the TKD-GND measured values is critical to final resolution. One uncertainty of the TKD-GND measured values comes from the TKD angular resolution. The angular resolution of TKD is generally accepted to be of the order of 0.5° to 1.0° angular error, which is similar to that of EBSD [89]. For example, if a step size 20 nm is set for TKD scanning, a GND density error of 10^{14.7} m⁻² (corresponding to 0.5° angular error) to 10¹⁵ m⁻² (corresponding to 1.0° angular error) can be estimated according to error estimation equation $\rho_{gnd}^{error} \approx \theta/bd$ [99].

2.3.3.5 Comparison of dislocation characterisation using TKD and TEM

Figure 2-10 shows the calculated TKD-GND density where a similar overall distribution of GND is suggested by both first order and second order averaging schemes. Figure 2-11 shows a GND density statistical comparison between the two schemes. Second order calculation scheme shows a slightly lower level of GND density compared with first order calculation scheme. Compared to the average dislocation density determined by TEM, the second order TKD-GND density provide a closer average value than that of the first order. This is owing to second order scheme averaged more pixels, thus resulting a lower lattice curvature noisy background. Therefore, the second order scheme had better agreement with the average dislocation density determined by TEM.

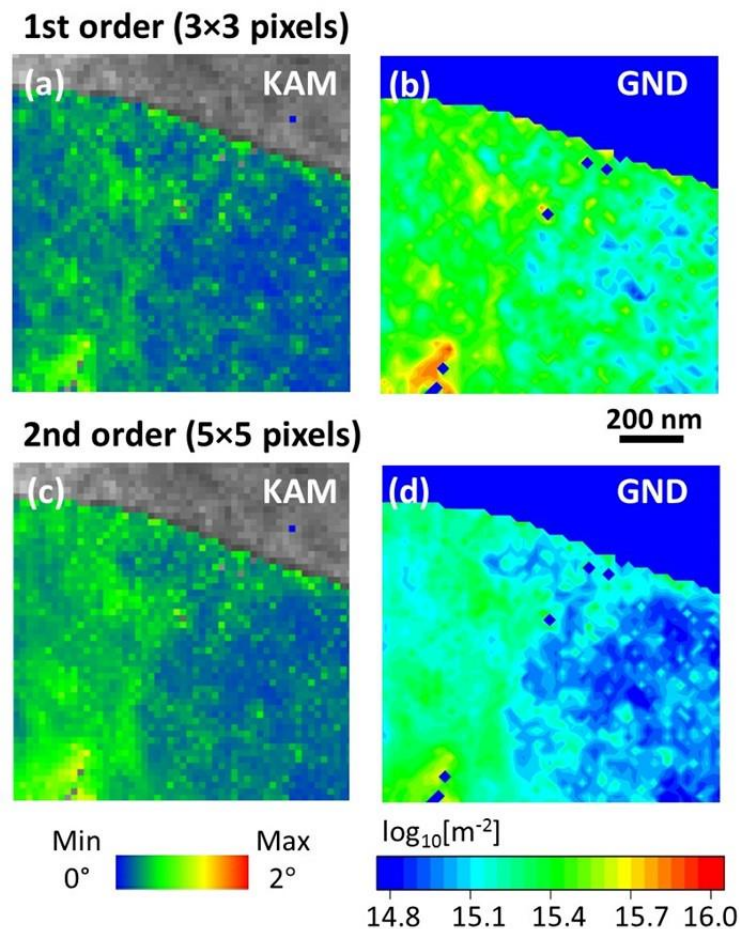


Figure 2-10 KAM and GND density maps of a selected area within a ferrite grain: first order results of (a) KAM and (b) GND; second order results of (c) KAM and (d) GND. Invalid pixels of GND are shown in blue.

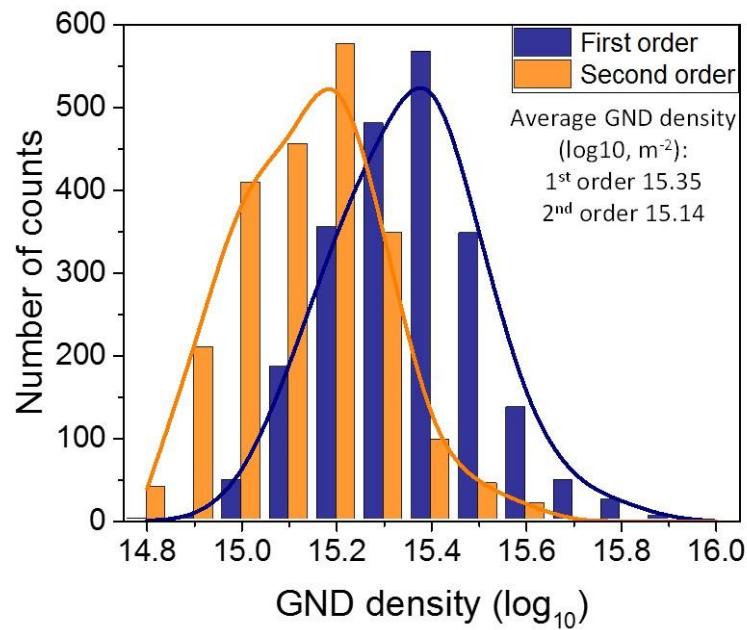


Figure 2-11 Histogram of scanned GND density values in local area using first order and second order calculation schemes.

As TEM not only provides an average dislocation density, but also able to image the dislocation lines distribution, we employ TEM to image the dislocation lines in TKD scanned area to validate the dislocation distribution of TKD-GND results. Figure 2-12 show the observation of dislocation lines using TEM under different diffraction conditions. It should be noted that the thickness of this area has a slope towards the left edge of the region which is measured to 85nm in thickness. Consequently, the dislocation lines on the left thinned region are difficult to be observed using TEM as the principle of observation is based on Bragg diffraction where a typical thickness range from 100 nm to 300 nm is desirable. Despite these difficulties, several clear and intense dislocation lines were directly imaged in the TEM, as circled in red in Figure 2-12. The observations agree with the TKD-GND density result. Although this is an isolated result, it appears the dislocation rich areas can be revealed by using the TKD-GND method. To further validate the moderate dislocation density differences, TEM observations were made in two different TKD-GND measured regions, as shown in Figure 2-12 (c) Since this area is too thin to obtain the local

thickness, a qualitative comparison is made here. Dislocation lines in Figure 2-12 (c) were highlighted by white dashed lines, and the Area-1 was found to exhibit a greater number of dislocation lines than the Area-2, which means that TEM confirms the Area-1 has higher dislocation density than the Area-2.

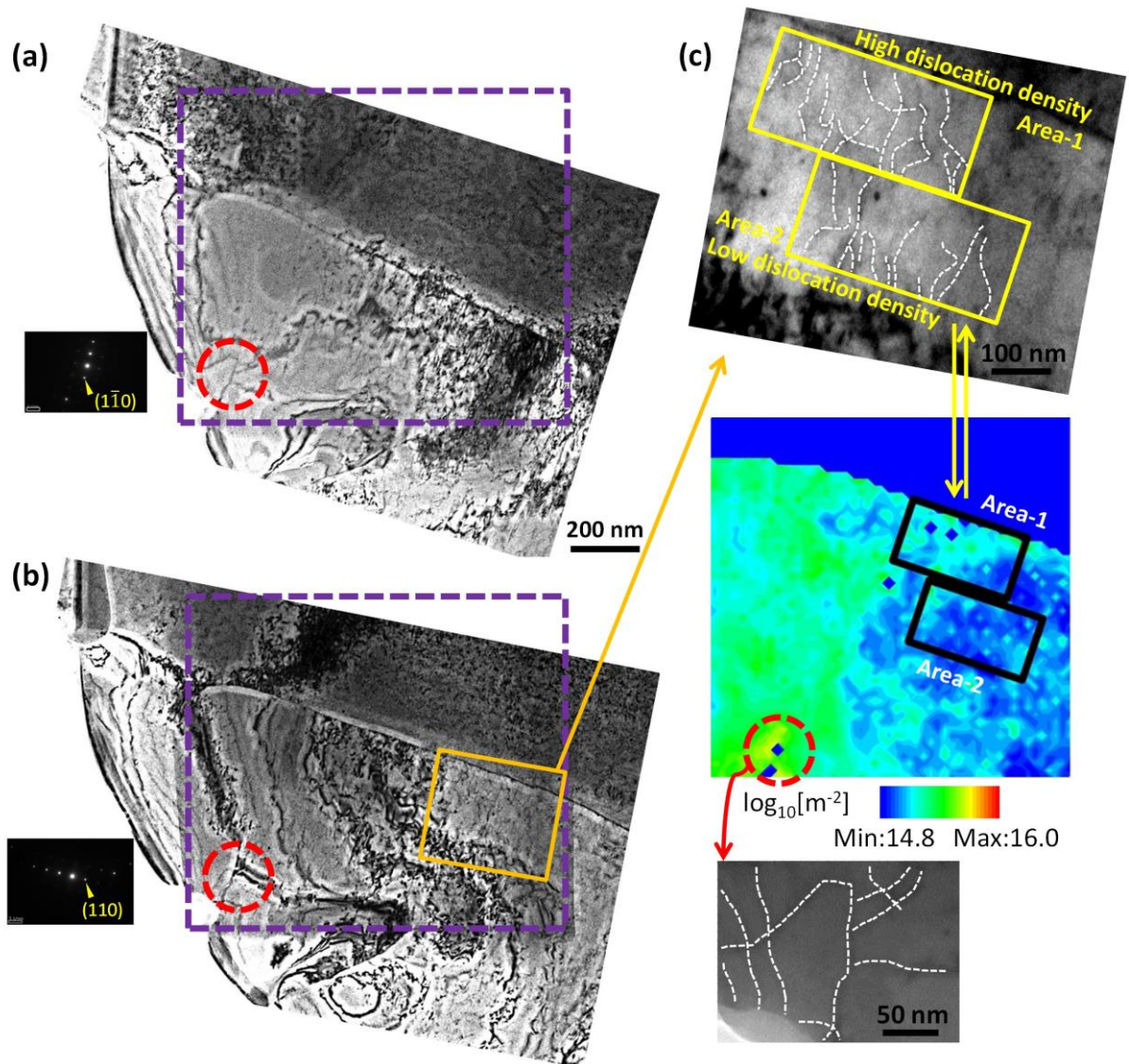


Figure 2-12 Bright field imaging by TEM under different diffraction conditions (a) $g//(\bar{1}\bar{1}0)$ and (b) $g//(\bar{1}10)$. Visibility of dislocation under different diffraction conditions is given in Fig. 7. The TKD scanned area is bound by the purple box. (c) a closer view of the dislocation lines; two regions, Area-1 and Area-2, are illustrated for comparison; the red circle area in TKD-GND result shows high density of dislocations, which is consistent with the TEM observation; dislocations in (c) were highlighted by white dashed lines.

The line intersection measurement method was used to assess the accuracy of the dislocation density determined by TKD-GND. Since the TKD scanned area is too thin to have a clear observation of dislocation lines, a region in same ferrite grain close to the TKD

scanned area was selected for dislocation density measurement by TEM observation. Figure 2-13 shows the results of TEM observations within this area. To measure the thickness of the region, the CBED pattern under two-beam condition was used, which reveals a sample thickness of approximately 85 nm. The overall average dislocation density was found to be approximately $10^{15.1}$ ($=1.26 \times 10^{15}$) m^{-2} . This is slightly lower than the dislocation density measured using the TKD-GND method where an average GND density of $10^{15.35}$ ($=2.2 \times 10^{15}$) m^{-2} was obtained for first order scheme and $10^{15.14}$ ($=1.4 \times 10^{15}$) m^{-2} for second order scheme.

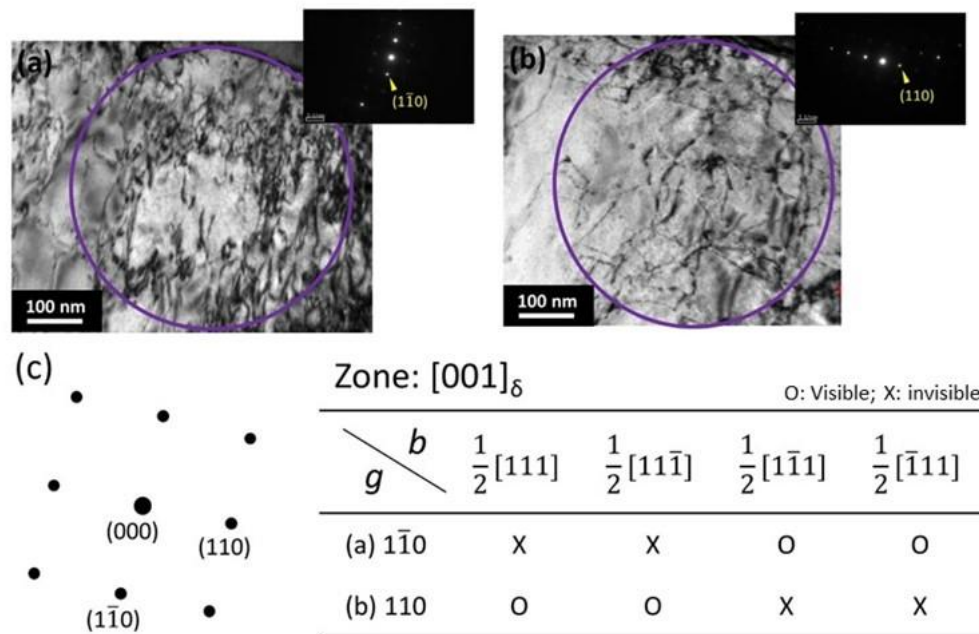


Figure 2-13 TEM bright field images of dislocations under different diffraction conditions (a) $g//(1\bar{1}0)$ and (b) $g//(110)$ with the incident beam direction approximately parallel to zone axis $[001]$; (c) schematic representation of zone-axis pattern with tabled dislocation visibility; dislocation is invisible when $g \cdot b = 0$.

2.3.3.6 Dislocation density determination using TEM

Using a TEM it is possible to observe dislocation lines directly and to determine the average dislocation density in a region using TEM line intersection method [74, 133]. Average dislocation density was determined using the following equation [74, 133]:

$$\rho = (n_v/L_v + n_h/L_h)/t \quad (3-2)$$

where n_v is the number of intercepted dislocations by a random length L_v along vertical direction, and similarly n_h and L_h are the parameters obtained along horizontal direction. The thickness t can be obtained by a variety of ways. In this study, the thickness is measured by using the method of convergent beam electron diffraction (CBED) in a two-beam condition, whose detail can be found in reference [134].

Chapter 3

Phase transformation in super duplex stainless steel

SDSS is a type of highly alloyed steel with balanced phases of ferrite and austenite. This microstructure combination is desirable to deliver good mechanical properties and corrosion resistance. However, these superior properties can be degraded by the presence of precipitates e.g. σ phase, χ phase, carbides and nitrides.

In this chapter, the phase transformations of SDSS are discussed by employing modelling and microscopy characterisation. Section 3.1 details equilibrium phase transformation. Section 3.2 presents the characterisation of precipitates in isothermal heat treated SDSS. Section 3.3 details the characterisation of precipitates in HAZ of a weldment. Section 3.4 summaries the Chapter.

3.1 Equilibrium phase transformations of SDSS

Section 1.2 introduced that SDSS is a type of highly alloyed steel in which chromium and nickel are the main alloy elements. Figure 3-1 shows an equilibrium Fe-Cr-Ni phase diagram for 68.0 wt. % Fe [135]. With a typical 25.0 wt. % Cr content in this system, a combination microstructure of ferrite and austenite can be achieved when temperature below 1350°C. A balanced, about half ferrite and half austenite, microstructure combination can be obtained between 1250°C to 1100°C. This temperature range has been suggested for quenching in the treatment of most of the SDSS.

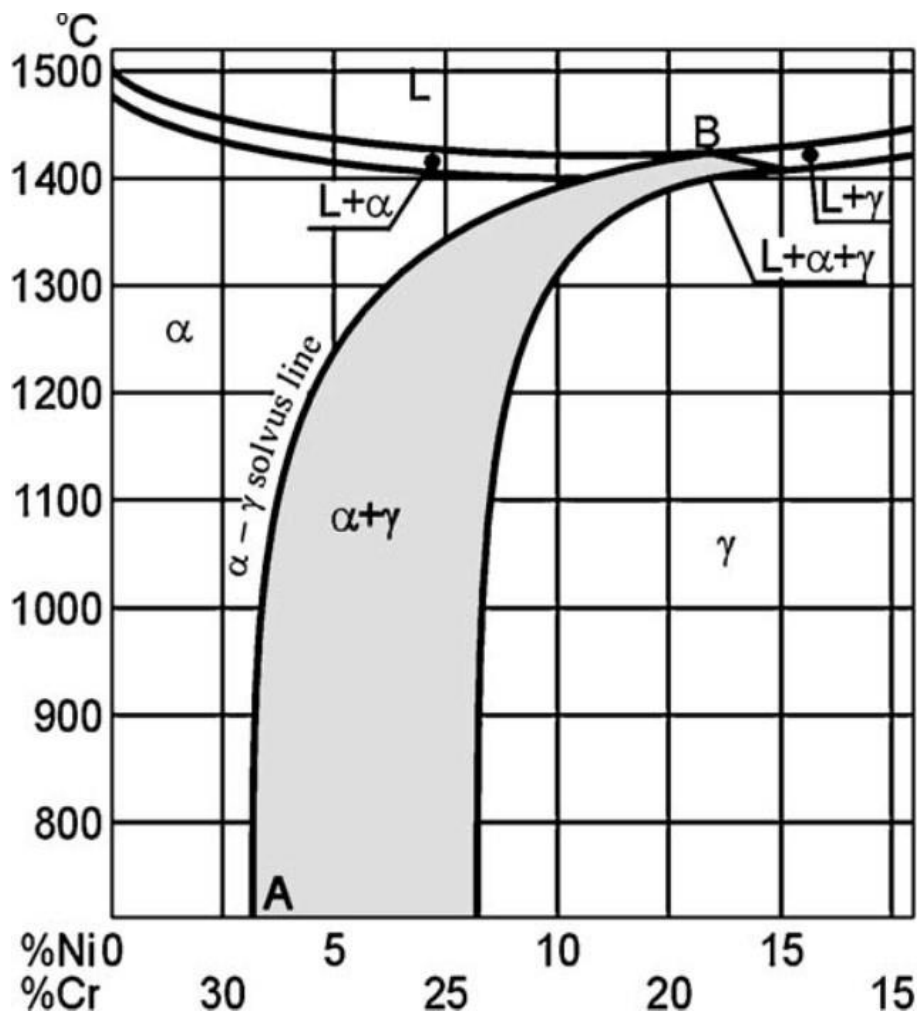


Figure 3-1 Fe-Cr-Ni equilibrium phase diagram for 68 wt. %Fe [135].

3.2 Precipitation in super duplex stainless steels

Zeron 100 is a type of SDSS that has wide application in industry. For Zeron 100, a desirable phase fraction of ferrite and austenite can be achieved between 1050°C and 1250°C, as shown in Figure 3-2. When the temperature drops below 1050°C, Cr₂N and σ phase starts precipitation. While in the temperature range between 900°C and 600°C, ferrite phase has much less proportion in the equilibrium condition. Instead, enrichment of σ phase and χ phase is realised in this temperature range as well as Cr₂N nitrides and M₂₃C₆ carbides.

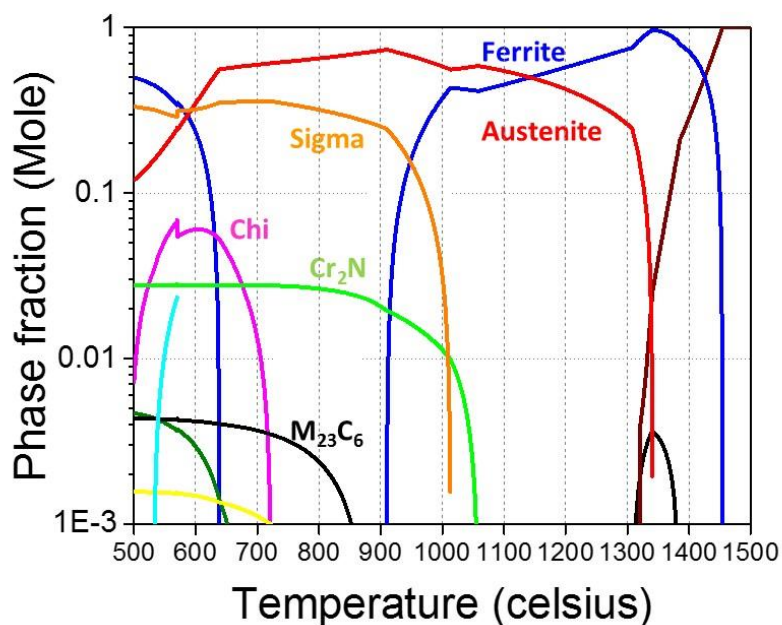
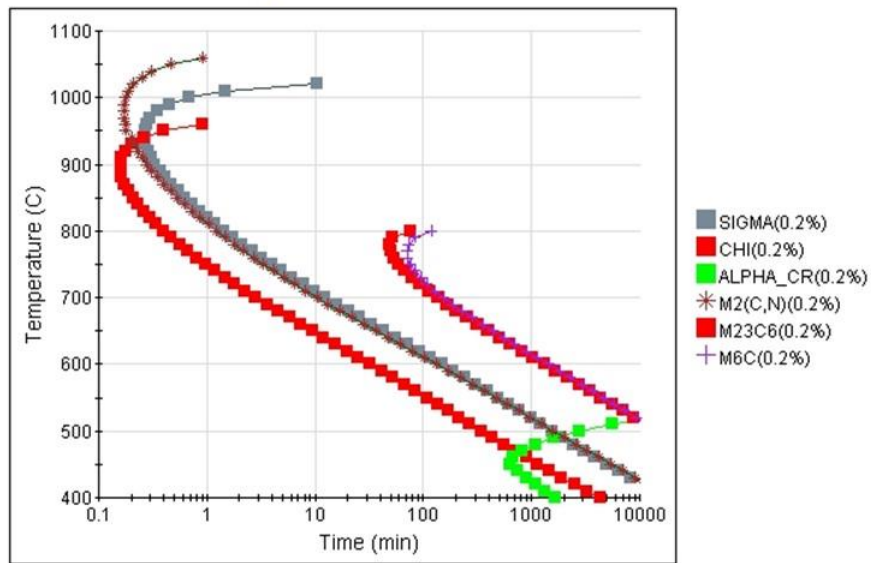


Figure 3-2 Equilibrium phase diagram of Zeron 100, calculated by Thermo-Calc (TCFE-6 database).

3.2.1 Isothermal phase transformation

JMatPro 8.0 package was used here to calculate the TTT diagram which can be used to predict the precipitation fraction in a fixed ageing temperature. Figure 3-3 shows the isothermal transformation in a temperature range from 1100°C to 400°C. Precipitates of σ phase, χ phase, and Cr₂N have great proportions within 1000°C to 700°C whilst alpha-chromium only present below 500°C.

TTT Duplex Stainless Steel



TTT Duplex Stainless Steel

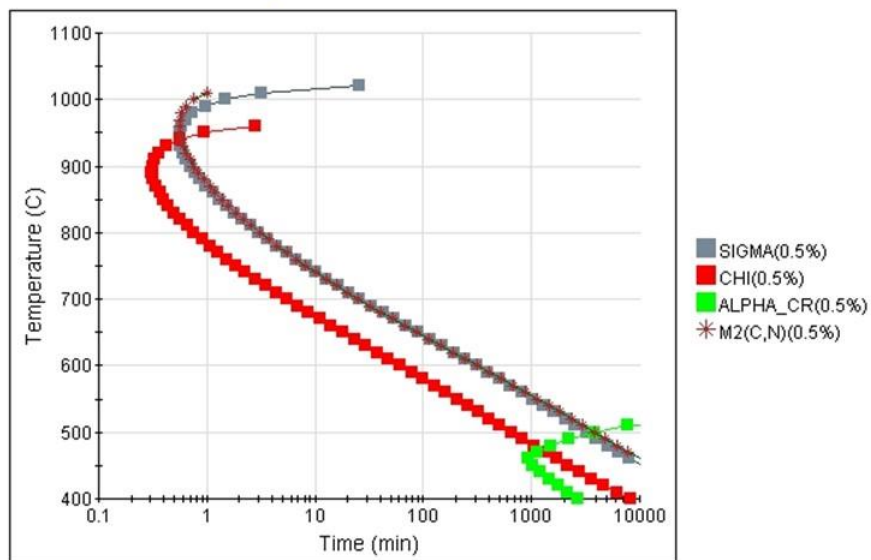


Figure 3-3 TTT diagram of SDSS, phase fraction is in weight percentage.

3.2.2 Element concentration in precipitates

A variety of precipitates can be facilitated in SDSS and they have different element concentrations. Figure 3-4 shows the calculated chemical concentration of different phases using JMatPro 8.0 package. σ phase possesses high chromium content whilst χ phase is predicted as a molybdenum rich precipitate. Though austenite is a matrix phase, it possesses

high nickel content and low chromium content compared with ferrite. This character can be used to identify secondary austenite phase precipitation in a ferrite matrix.

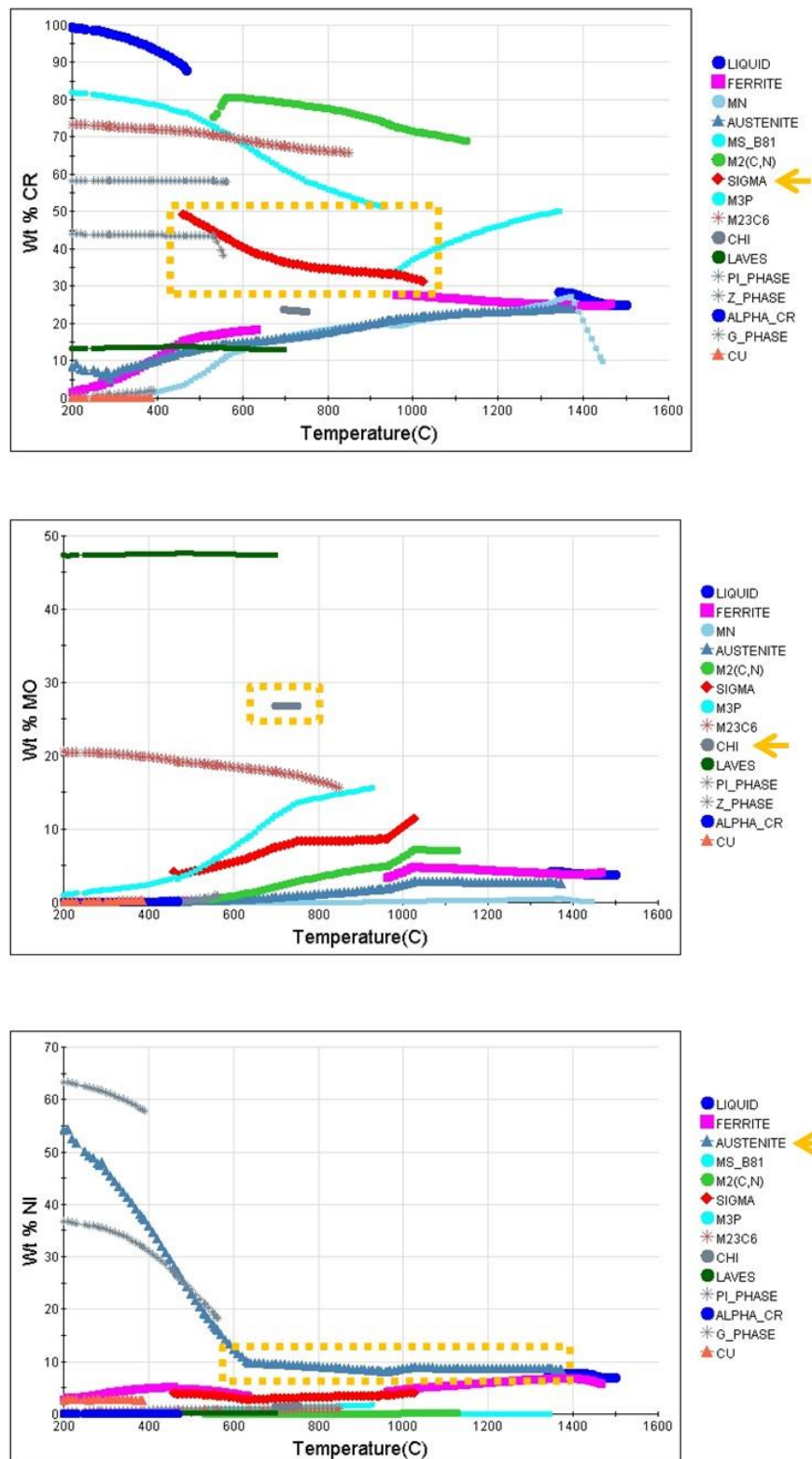


Figure 3-4 Element concentration in different phases, calculated by JMatPro.

3.2.3 Precipitation by isothermal heat treatment

The above section has discussed the modelling of phase evolution which the precipitation can be facilitated below 1050°C. To further study the morphology and their precipitation mechanisms, bulk Zeron 100 pipeline samples were used: an isothermal heat treatment at 800°C was applied after a solution treatment at 1200°C for 1 hour. The sample preparation detail is shown in Section 2.1.1.

Figure 3-5 shows the phase evolution of SDSS by 800°C isothermal heat treatment with varies ageing time. Figure 3-5 (a) shows the morphology using SEM after solution treatment and no precipitates can be observed. With a 6-min ageing at 800°C, as shown in Figure 3-5 (b), a small volume of χ phase can be observed that precipitates at boundaries. In this view, the area ratio of χ phase is measured to about 2.0 (± 0.4) %. Figure 3-5 (c) shows the microstructure after 30 min ageing at 800°C. The precipitation of χ phase seems to have kept to the same volume whereas σ phase presents has a 3.0 (± 0.6) % area ratio. Figure 3-5 (d) shows the obtained microstructure with 60 min ageing at 800°C. The σ phase has a large precipitation volume in the matrix, a 16.0 (± 4.0) % area ratio is measured. It should be noted that the precipitation of nitrides and carbides is not observable at this magnification.

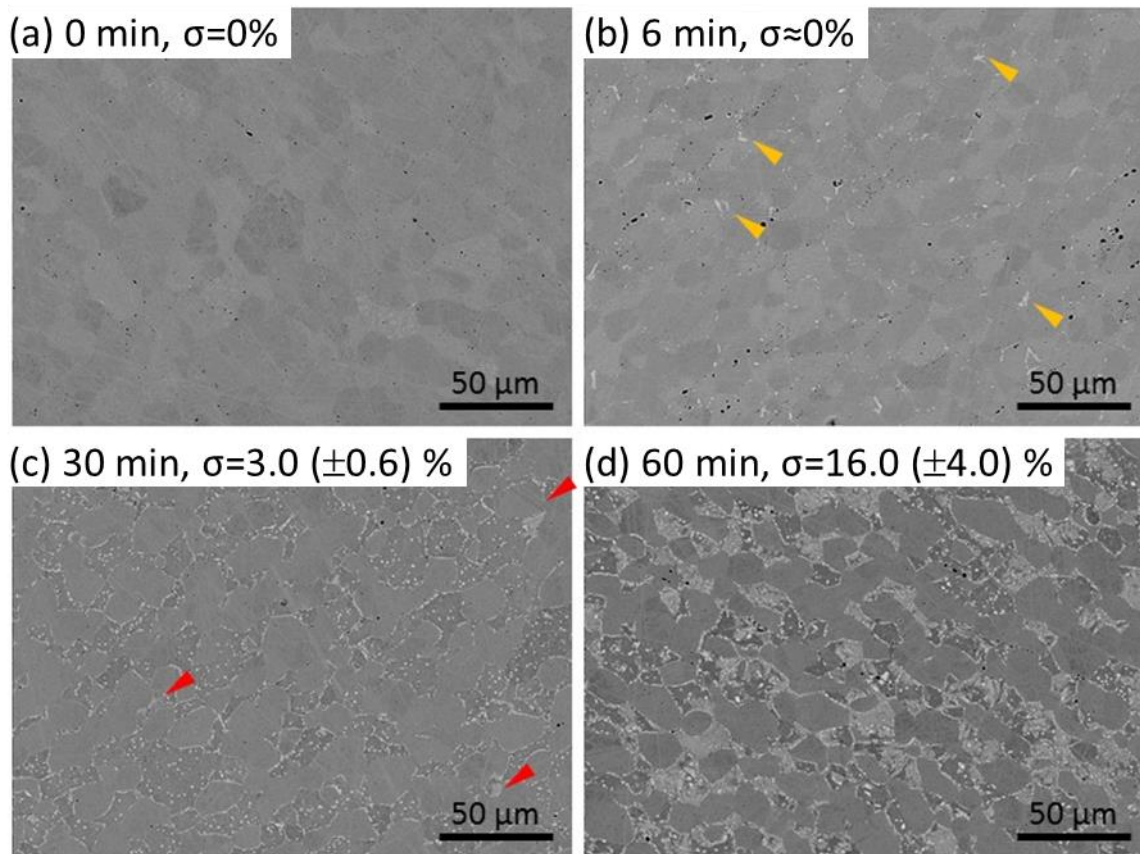


Figure 3-5 Phase evolution of SDSS by 800°C isothermal heat treatment with heat ageing time of (a) 0 min, (b) 6 min, (c) 30 min, (d) 60 min; orange and red arrows point to the precipitation of χ phase and σ phase, respectively; images obtained by SEM under BSE mode.

3.2.4 Precipitation of sigma phase

σ phase is a well-known chromium rich deleterious phase in super duplex stainless steels. With the precipitation of σ phase in the matrix, its brittle mechanical property and the facilitation on chromium depleted phases formation can result in a considerable reduction of materials strength and corrosion resistances, respectively.

3.2.4.1 Effect of σ phase precipitation on mechanical properties

A Charpy impact test was performed to determine the effect of σ phase precipitation on the impact energy absorbed by a material during fracture. The sample was machined as $10 \times 10 \times 55 \text{ mm}^3$ with a V-notch according to standard ISO 148 [136]. The experiment was performed on an impact test machine with maximum energy load of 500 J.

Figure 3-6 shows an impact energy reduction with an increase of σ phase precipitation whose fraction is measured according to the results in Figure 3-5. It can be seen that the original impact energy 180 J can be dramatically degraded to 18 J with 3.0% σ precipitation. A further reduction of impact energy is realised with higher σ phase precipitation.

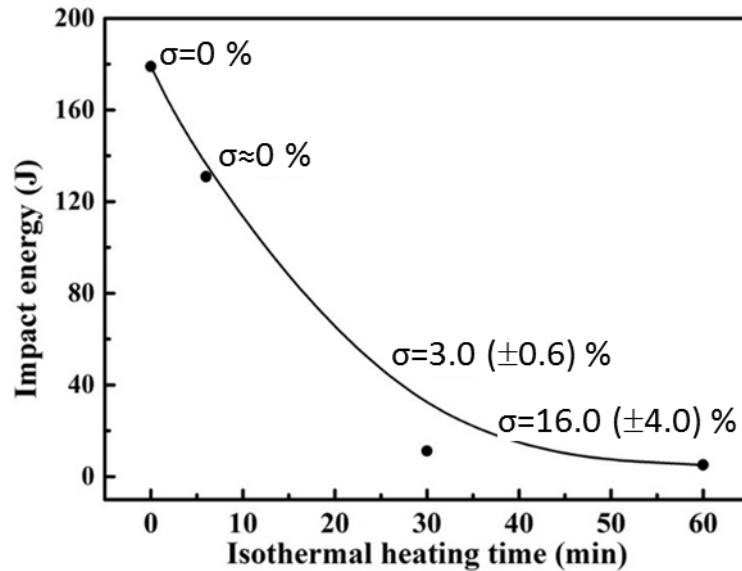


Figure 3-6 Impact energy of SDSS against varies ageing times at 800°C.

3.2.4.2 STEM-EDS characterisation of σ phase

Figure 3-7 shows σ phase precipitation on a ferrite-ferrite grain boundary using STEM. Three STEM-EDS point tests were performed. Point 1 and point 2 located on intergranular σ phase and intragranular σ phase, respectively. However, a high chromium content 31.4 wt. % was detected on intergranular σ phase (Point 1 located) whilst 28.5 wt. % chromium content was detected on intragranular σ phase (Point 2 located). This result suggests a chemical difference exist between the intergranular σ phase and the intragranular σ phase. Also, the result suggests the formation of adjacent chromium depleted secondary austenite dendrites are accommodated with these intragranular σ dendrites. A STEM-EDS was performed on a secondary austenite where a 23.4 wt. % chromium content is obtained.

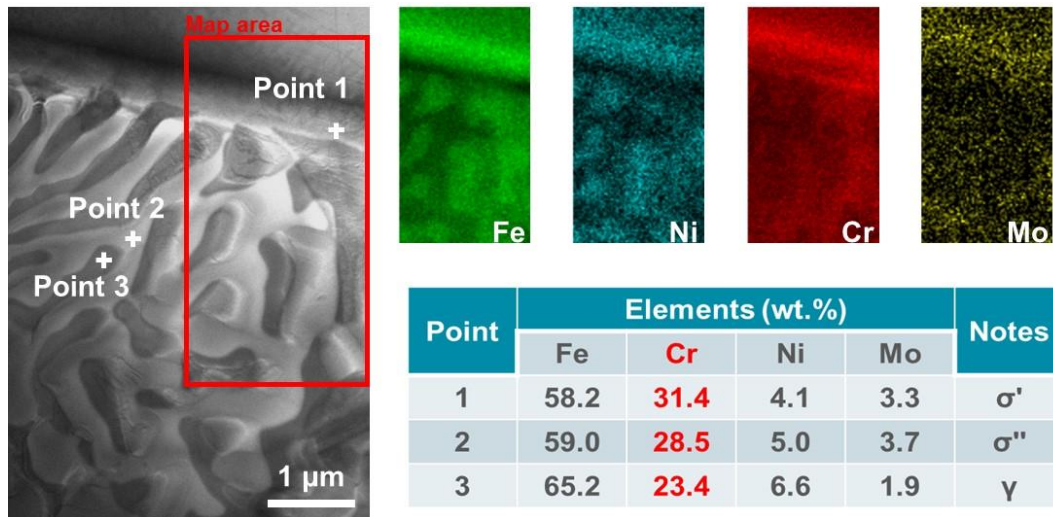


Figure 3-7 TEM bright field image of σ phase precipitation at a ferrite-ferrite grain boundary; EDS map was obtained from the red boxed area; EDS point tests were performed on three points with EDS results tabled.

3.2.4.3 TKD map of sigma phase precipitation

Above STEM characterisation and STEM-EDS chemical examination has implied the precipitation of chromium rich σ phase is accommodated with chromium depleted secondary austenite dendrites. To further detail the phase distribution, TKD method is engaged here for this purpose. Figure 3-8 shows a TKD result of σ phase precipitation at a ferrite grain boundary in an SDSS with an ageing treatment at 800°C for 1 hour. The result shows the phase distribution of σ phase and secondary austenite along a ferrite-ferrite grain boundary. Dimensions of these σ phases and secondary austenite grains are of sub-micron size. Here, an intragranular σ phase is identified along ferrite-ferrite grain boundary, which shows a correspondence to the STEM result in Figure 3-7.

Besides the identified σ phase and secondary austenite, a small volume of χ phase is measured in this area. These χ precipitates have nano-size dimensions which are hard to find using conventional TEM method.

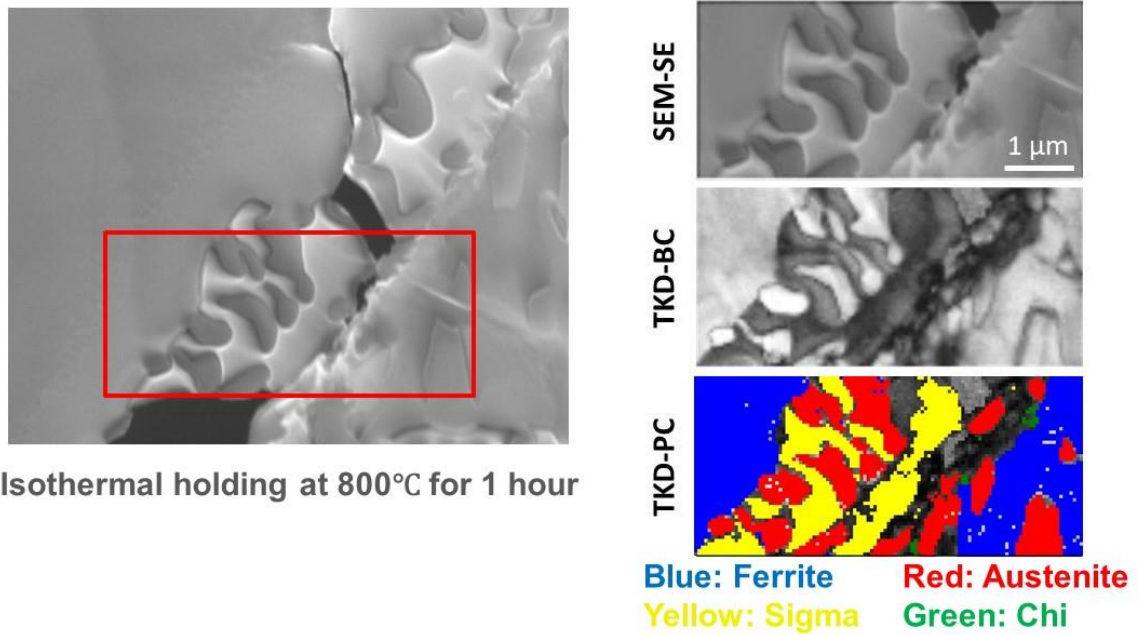


Figure 3-8 TKD result of σ phase precipitation at a ferrite-ferrite grain boundary.

3.2.4.4 A precipitation mechanism of σ phase

As suggested by the STEM and TKD results above, a mechanism of σ phase precipitation can be proposed. Figure 3-9 shows the proposed precipitation evolution of σ phase over time. In the first stage, as the result shown in Figure 3-5, the precipitation of χ phase is present which is earlier than the precipitation of σ phase. In the following stage, an intergranular σ phase is formed after χ phase precipitation at a ferrite-ferrite grain boundary. In the third stage, the growth of adjacent intragranular σ phase starts after the formation of this intergranular σ phase. A typical chemical composition difference between them is a lower chromium content in intragranular σ phase compared with intergranular σ phase. Finally, precipitation of both intragranular and intergranular σ phases are present at this ferrite-ferrite grain boundary.

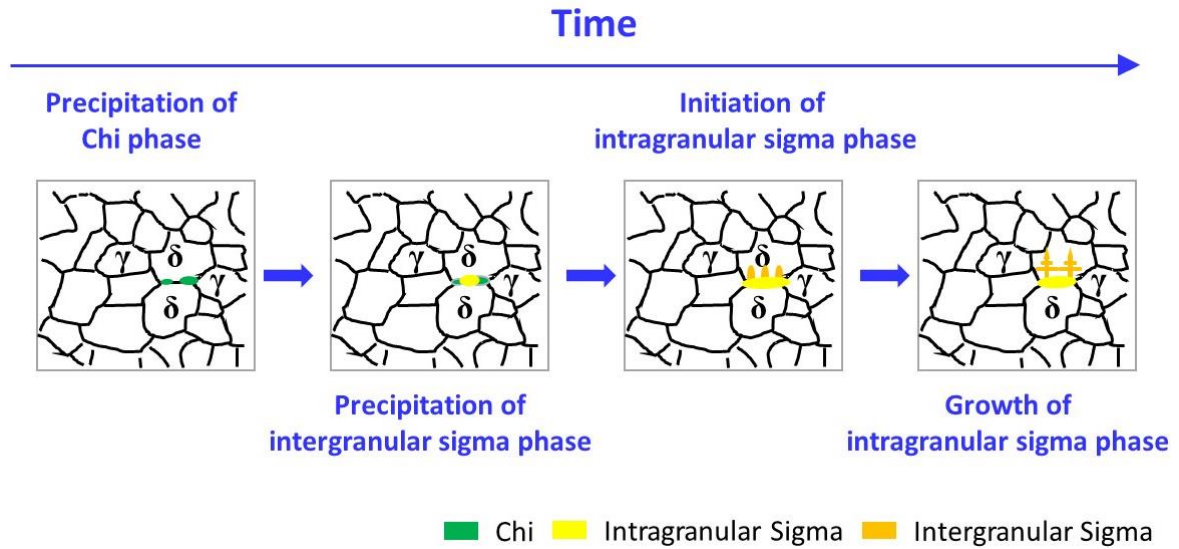


Figure 3-9 A proposed mechanism of σ phase precipitation at a ferrite-ferrite grain boundary.

3.2.5 Precipitation of chi phase

In SDSS, χ phase is a metastable phase whose precipitation occurs in the temperature range from 850°C to 720°C and it can be a stable phase between 720°C and 500°C according to equilibrium phase diagram in Figure 3-2 and TTT diagrams in Figure 3-3, respectively.

Figure 3-5 shows the precipitation of χ phase is present after a 6-min ageing at 800°C. An approximate saturation of χ phase is realised with 30 min ageing. Figure 3-10 shows an EBSD study of χ phase precipitates at a phase boundary where a submicron dimension of χ phase precipitates is scanned.

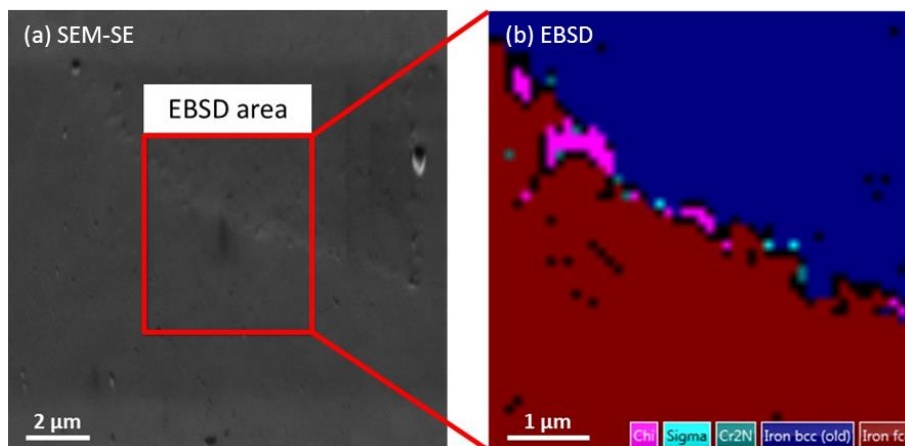


Figure 3-10 Characterisation of χ phase at a phase boundary: (a) scanning area shown in SEM-SE and (b) EBSD result.

3.2.6 Precipitation of nitrides and carbides

Nitrides and carbides are common precipitates in steels. In SDSS, a limited content of nitrogen is added to improve the weldability and balance the austenite and ferrite phase fraction, whilst the addition of carbon content is restricted to lower the tendency of precipitation.

3.2.6.1 Nitrides

As it has been mentioned in Section 1.2.3.2, the alloying of nitrogen is a strong austenite stabilizer and it can improve the materials weldability by reducing the tendency of grain coarsening. However, the alloying of nitrogen increases the tendency of nitrides formation.

Figure 3-11 shows a TEM bright field image of Cr_2N precipitates in ferrite matrix which is facilitated by ageing at 800°C for 1 hour. It shows these Cr_2N rods having a width about 100 nm and several hundred nanometres in length.

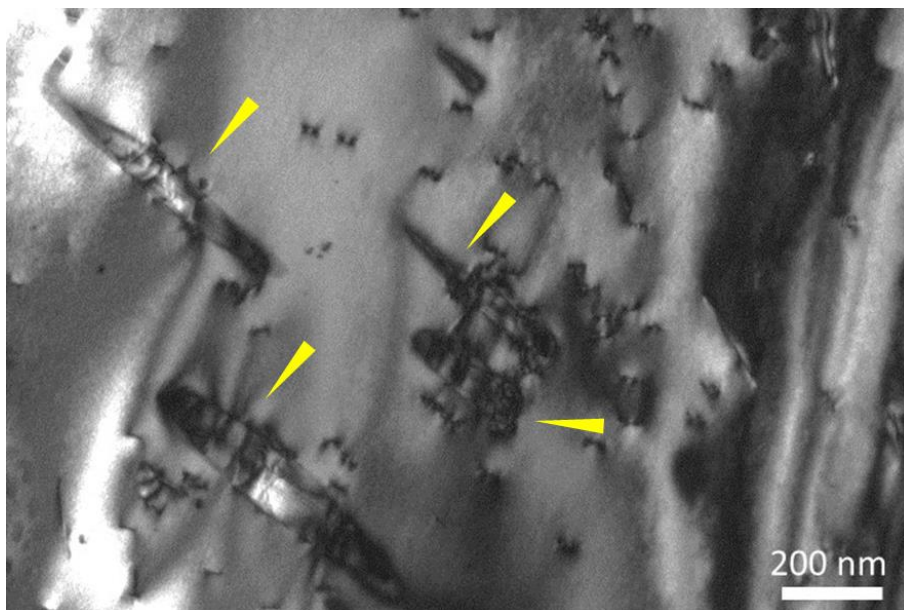


Figure 3-11 TEM bright field image of rod Cr_2N precipitates (yellow arrows pointed) in the ferrite matrix.

Figure 3-12 shows a TEM bright field image of Cr_2N precipitates at a phase boundary which is facilitated by ageing at 800°C for 1 hour. The morphology of these Cr_2N precipitates is similar to the Cr_2N in Figure 3-11.

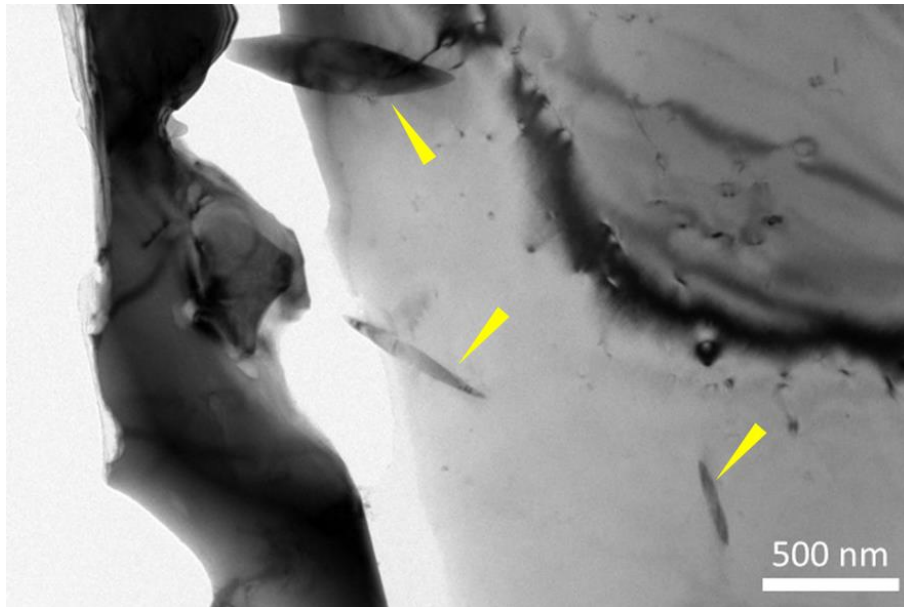


Figure 3-12 TEM bright field image of rod Cr_2N precipitates (yellow arrows pointed) at phase boundary; part of austenite has been polished off during sample preparation.

3.2.6.2 Carbides

With the advances in metallurgy, the carbon content has been limited to a very low proportion in steel. In SDSS, a carbon content is normally alloyed at less than 0.03 wt. %. Such minimisation of carbon content has largely reduced the drawbacks by carbides precipitation. Nevertheless, it has been found that the precipitation of carbides has an effect on facilitating nitrides precipitation. Figure 3-13 shows a STEM image which reveals a row of Cr_2N rods on lamellar M_{23}C_6 along a ferrite-austenite phase boundary.

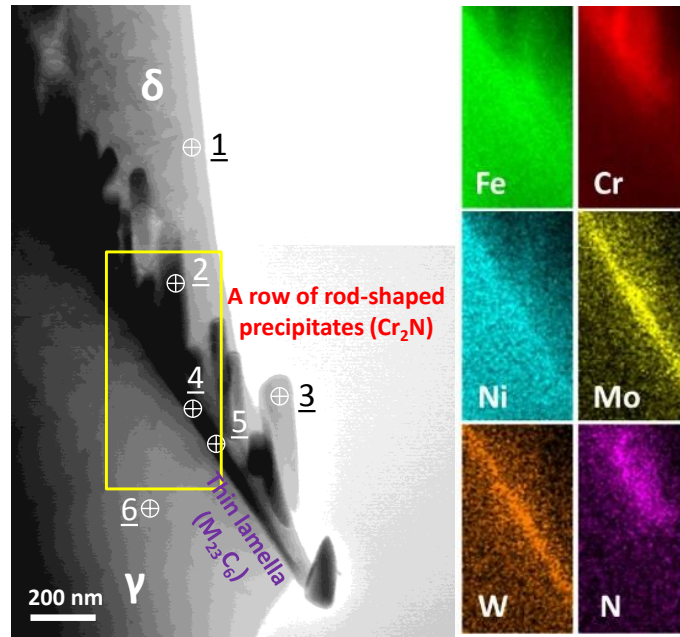


Figure 3-13 STEM observation of rod-shaped precipitates on a thin lamellar precipitate, and the corresponding EDS examination results are shown in Table 1; EDS mapping, results on right side, was performed to examine the highlighted area (yellow box).

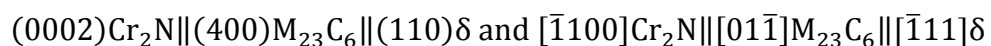
Table 3-1 shows the STEM-EDS result of the Cr_2N and M_{23}C_6 . High chromium contents are measured from the Cr_2N while high molybdenum and tungsten are measured from M_{23}C_6 lamella precipitate.

Table 3-1 STEM-EDS results of the Cr_2N and M_{23}C_6 .

Method	Spot	Elements (Wt. %)					Position
		Fe	Cr	Ni	Mo	W	
STEM-EDS	1	58.2	29.2	5.1	3.9	0.8	δ -ferrite
	2	34.0	54.8	2.9	4.1	0.7	Rods (Cr_2N)
	3	18.1	72.1	1.4	4.0	-	Rods (Cr_2N)
	4	49.6	25.9	5.4	12.0	4.0	Lamella (M_{23}C_6)
	5	49.7	27.6	5.8	10.4	3.2	Lamella (M_{23}C_6)
	6	60.9	26.1	7.7	2.7	-	γ -austenite

High resolution TEM image is able to image the lattice spacing and further determine the lattice structure. Here, this method is used to determine the lattice orientations of ferrite matrix, Cr_2N rods and M_{23}C_6 . Figure 3-14 shows the result of high resolution TEM images.

The orientation relationship can be determined as:



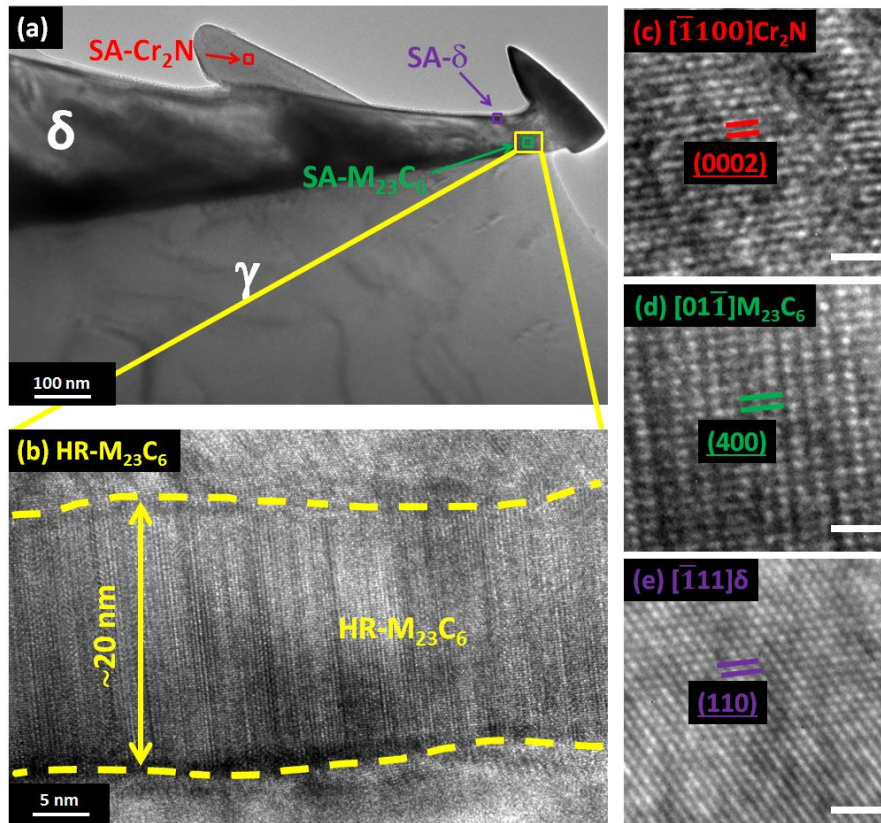


Figure 3-14 (a) low magnification TEM image of the grain boundary, which shows Cr₂N rods ‘seating’ on the vicinity lamellar M₂₃C₆; (b) high magnification image of the lamellar M₂₃C₆ from the yellow boxed area which shows the width of this M₂₃C₆ is ~20 nm; HR images of (c), (d) and (e) are taken from the square boxed selected areas (SAs) with corresponding colours; scale bars for HR images on the right side are 1 nm; the predominant orientation relationship can be confirmed as (0002)Cr₂N|| (400)M₂₃C₆|| (110)δ and $[\bar{1}100]$ Cr₂N|| $[01\bar{1}]$ M₂₃C₆|| $[\bar{1}11]$ δ

SADP is used to further determine the orientation relationship between ferrite and austenite, and the result is shown in Figure 3-15. The orientation relationship between ferrite and austenite can be determined:

$$(202)\delta \parallel (3\bar{1}1)\gamma \text{ and } [\bar{1}11]\delta \parallel [\bar{1}14]\gamma, \text{ with } 3.2^\circ \text{ misorientation}$$

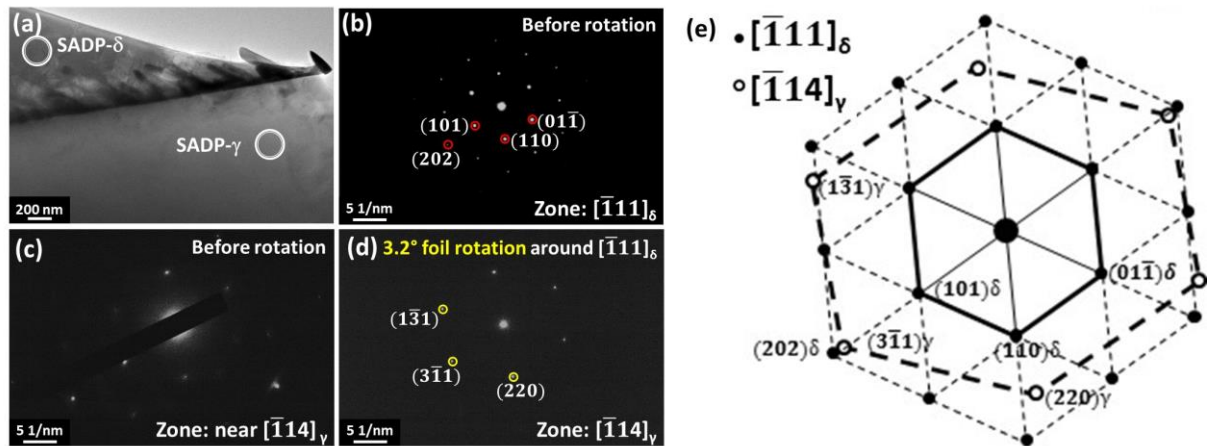


Figure 3-15 (a) TEM image indicating SAs of austenite and ferrite; (b) SADP of ferrite in zone axis $[\bar{1}11]_{\delta}$; (c) SADP- γ near zone $[\bar{1}14]_{\gamma}$; (d) clear $[\bar{1}14]_{\gamma}$ austenite SADP after 3.2° rotation around $[\bar{1}11]_{\delta}$; (e) Schematic representation of ferrite and austenite diffraction pattern, revealing austenite does not have a direct orientation relationship with either ferrite or $M_{23}C_6$

3.3 Precipitates in HAZ of a weldment

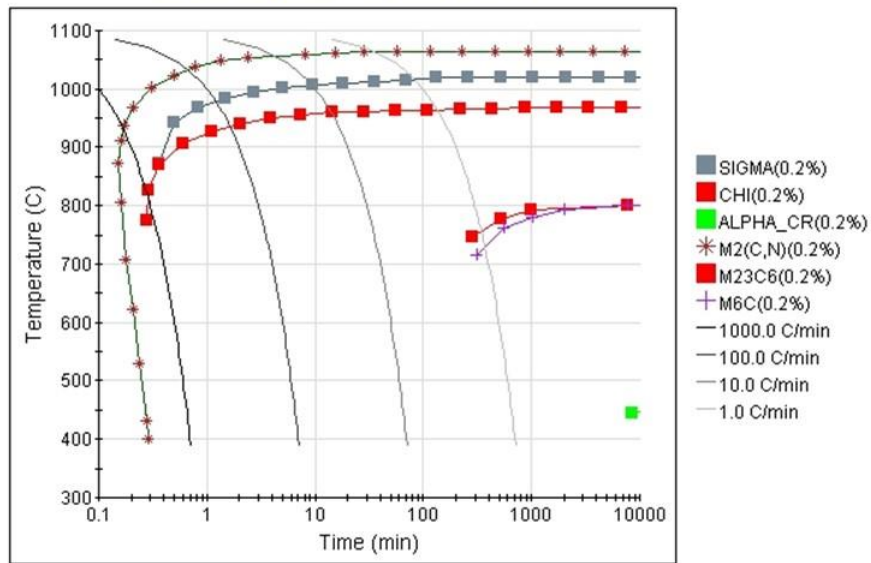
A desirable SDSS possess a balanced ratio of ferrite and austenite phases without precipitates. However, the precipitates can be facilitated when SDSS exposed to certain temperature range. The application of welding can introduce a heat input in the melting zone and then introduce a temperature gradient in the weldment. The term of HAZ is used to specify the area that materials microstructure altered by the heat input.

3.3.1 Continuous cooling transformation

A CCT diagram is often applied for heat treatment of metals when a controlled cooling rate is planned. Also, the CCT diagram can be used to guide the phase transformation in the HAZ of the welding. Here, the JMatPro package is applied again to calculate CCT diagrams [106].

Figure 3-16 shows a CCT diagram of Zeron 100. The CCT diagram predicts Cr_2N has a faster precipitation rate than other precipitates. In the following section, the Cr_2N precipitation in HAZ will be discussed.

CCT Duplex Stainless Steel



CCT Duplex Stainless Steel

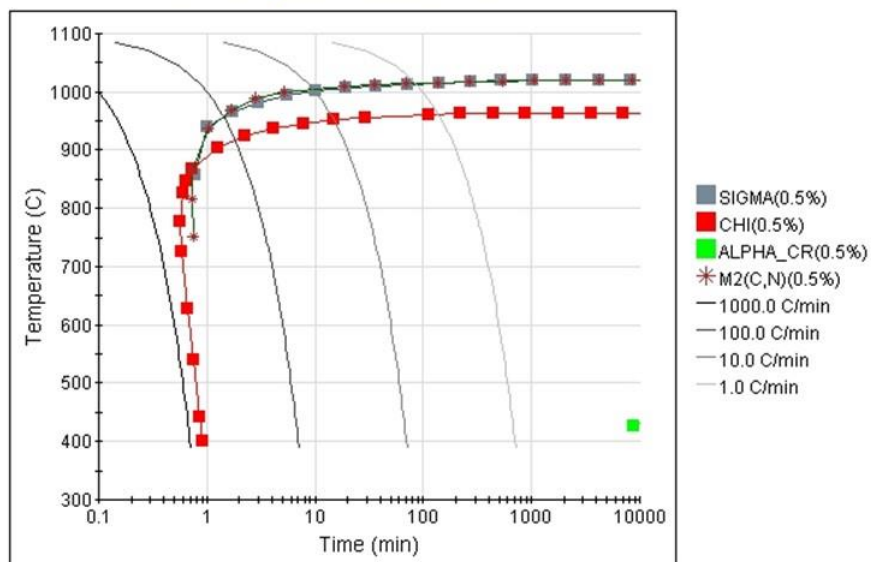


Figure 3-16 CCT diagram of SDSS, phase fraction is in weight percentage.

3.3.2 Precipitates in HAZ of a weldment

Welding is a popular fabrication process which is often used to join materials. By introducing a heat input, the fusion zone undergoes a melting and then solidification. The microstructure in fusion zone and HAZ is altered by the heat input, which may result in a grain growth and precipitation.

3.3.2.1 Microstructure change in HAZ

A serviced weldment is studied where the raw photomicrograph and chemistry are shown in Section 2.1.1. Figure 3-17 (a) shows the morphology of flange using SEM. The island-shaped grains with the convex feature are austenite while the rest is ferrite. Figure 3-18 (b) and (c) show the morphology of HAZ using SEM. Both cap and root of HAZ have microstructure changes where irregular grain/phase boundaries features are revealed. An obvious grain coarsening is imaged in HAZ cap area. Similar to HAZ cap region, a grain coarsening is also realised in the microstructure of HAZ root area but narrower than HAZ cap region.

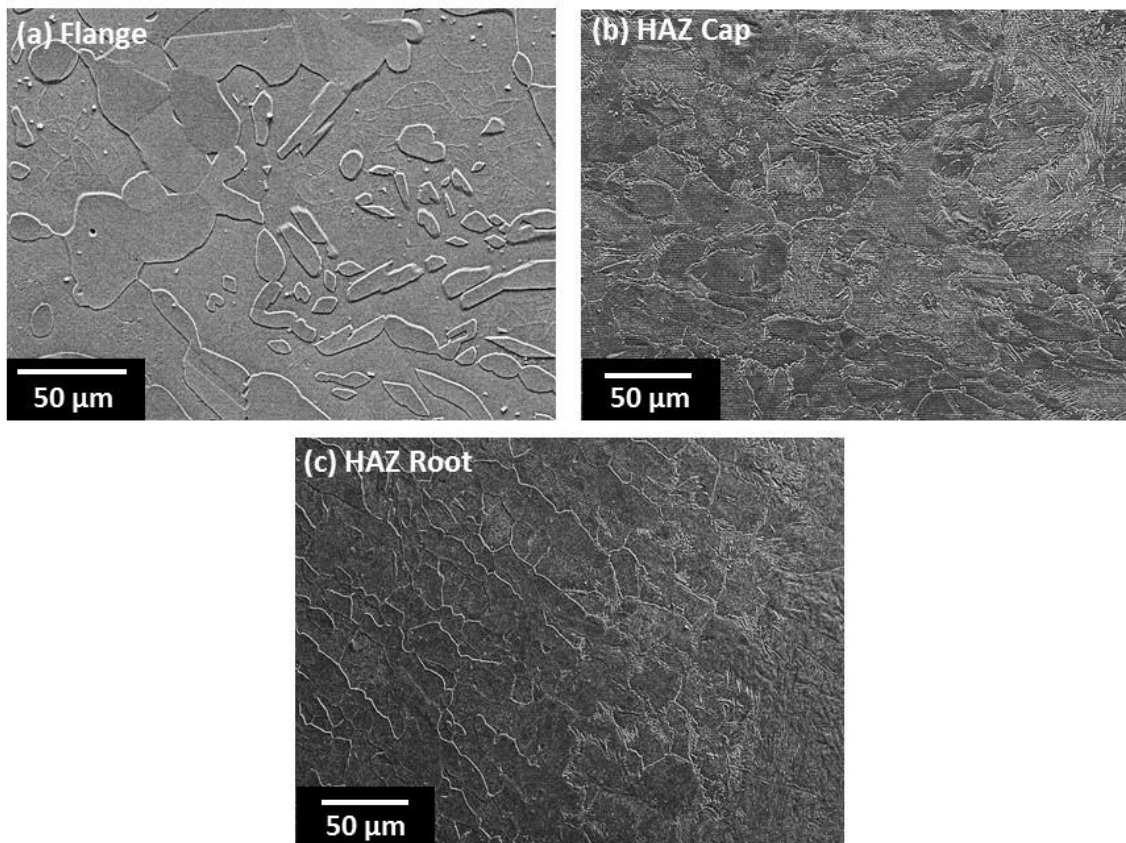


Figure 3-17 SEM images show the morphology of (a) Flange; (b) HAZ Cap and (c) HAZ Root.

3.3.2.2 Precipitates in HAZ

Figure 3-18 shows the identified precipitates in the HAZ of the weldment with corresponding SEM-EDS results shown in Table 3-2. Austenite possess higher nickel

content than ferrite while ferrite has higher chromium content than austenite. The precipitates of σ phase show an even higher chromium content than ferrite. χ phase has a high molybdenum content but a relatively low chromium concentration.

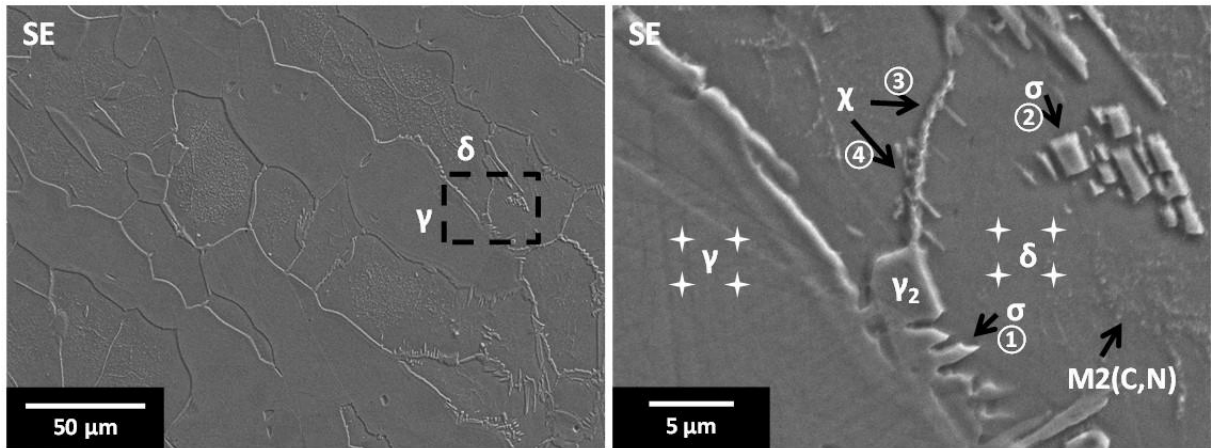


Figure 3-18 Precipitates in HAZ of the weldment.

Table 3-2 SEM-EDS results performed in HAZ of a weldment

	Point selected area	Cr (wt.%)	Fe (wt.%)	Ni (wt.%)	Mo (wt.%)
γ	Average (4 points)	23.8	63.6	8.7	3.9
δ	Average (4 points)	25.7	64.5	6.0	3.8
σ	Point 1	29.1	60.5	4.8	5.6
	Point 2	28.7	62.5	3.8	5.0
χ	Point 3	25.3	62.7	6.4	5.6
	Point 4	27.4	60.2	6.4	6.0

Figure 3-19 shows an enlarge SEM image that a row of nano-size Cr_2N is precipitated at a phase boundary. The size of Cr_2N is small and it is not possible to use EDS to test its chemical composition.

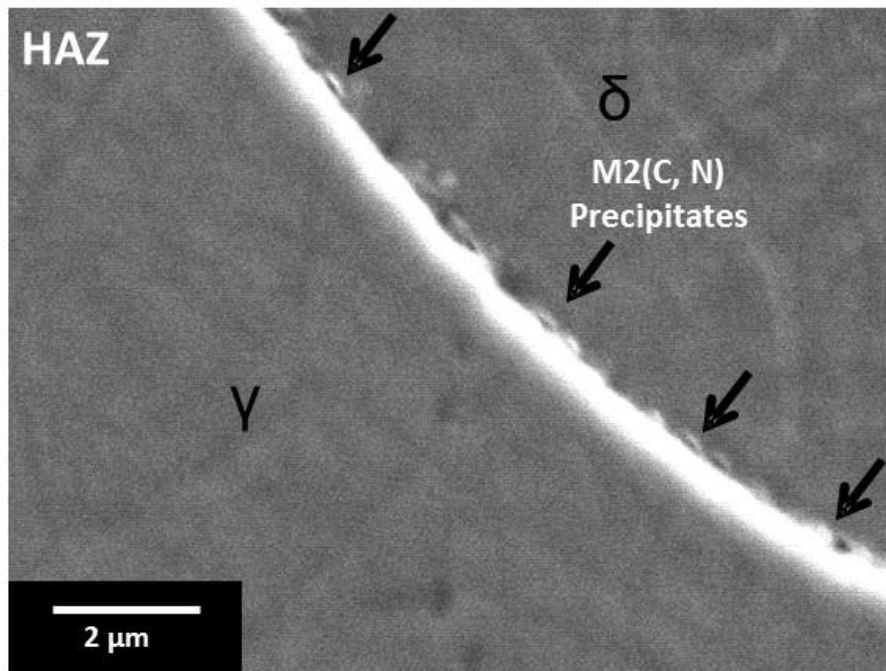


Figure 3-19 Cr₂N precipitates at austenite-ferrite phase boundary, imaged by SEM in SE mode.

3.3.3 Precipitation of chromium nitrides

As it has been shown above, the dimension of Cr₂N precipitates is about 100 nm to 200 nm. As this dimension is too small to be studied using SEM, the TEM is used to further characterise its precipitation in HAZ.

3.3.3.1 Embryo of Cr₂N

Figure 3-20 shows a chromium rich precipitate at a ferrite-austenite phase boundary and Table 3-3 shows the corresponding STEM-EDS results. The STEM-EDS reveals a 46.1 wt. % chromium content in this precipitate while the adjacent matrix only possesses about 24 wt. % chromium contents. Figure 3-21 shows another two chromium rich precipitates at a ferrite-austenite phase boundary. An EDS map scan was performed in the masked area. The result shows two areas have higher chromium and nitrogen concentration. This result suggests these two sites are the embryo of the precipitation of chromium nitrides.

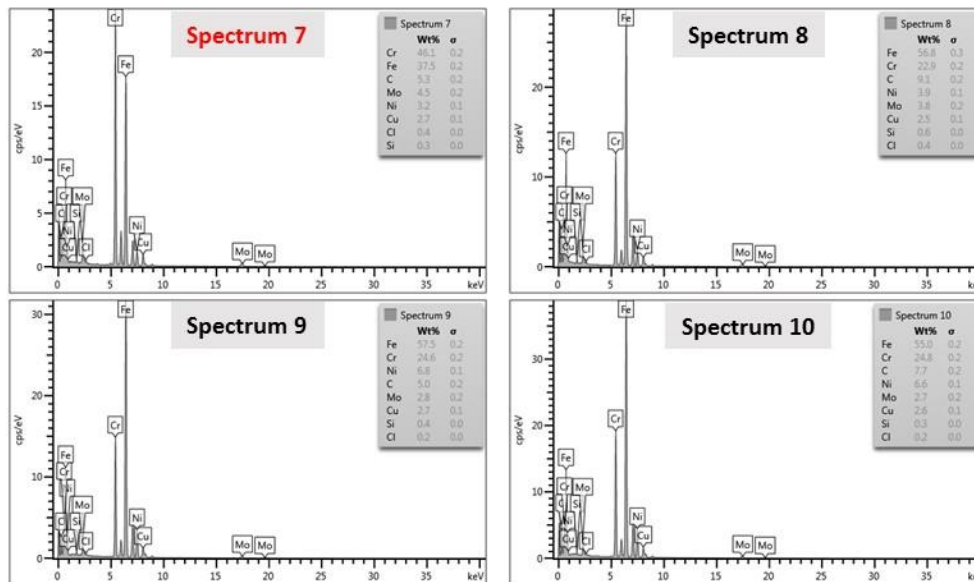
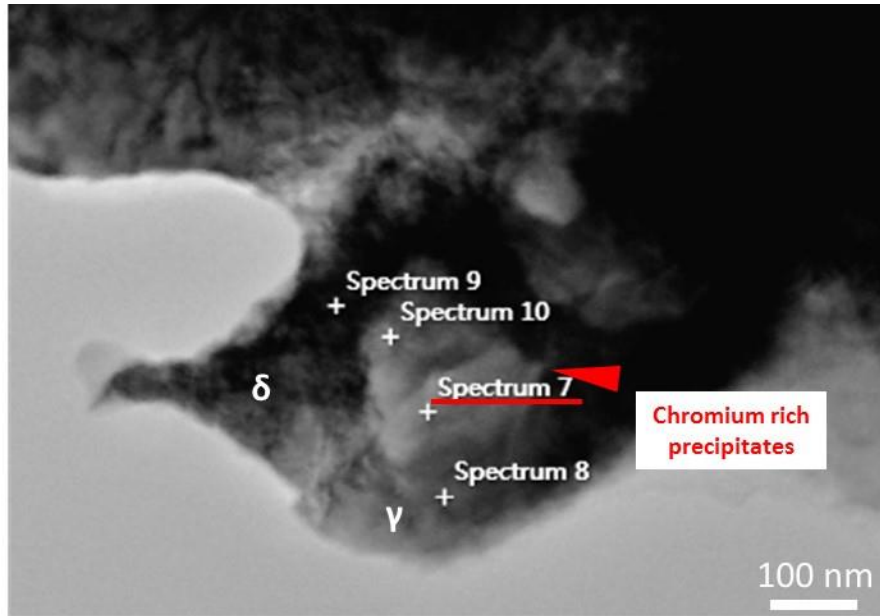


Figure 3-20 STEM image of a chromium rich precipitate at a boundary; four STEM-EDS spot tests were performed across the precipitate; spectrum 7 shows a high chromium content 46.1 wt. % while the matrix only has approximately 24 wt. % chromium contents.

Table 3-3 STEM-EDS result of chromium rich precipitates

Spectrum	Chemical composition (wt. %)				
	Fe	Cr	Ni	Mo	Others
7	37.5	46.1	3.2	4.5	C 5.3; Cu 2.7; Cl 0.4; Si 0.3
8	56.8	22.9	3.9	3.8	C 9.1; Cu 2.5; Cl 0.4; Si 0.6
9	57.5	24.6	6.8	2.8	C 5.0; Cu 2.7; Cl 0.2; Si 0.4
10	55	24.8	6.6	2.7	C 7.7; Cu 2.6; Cl 0.2; Si 0.3

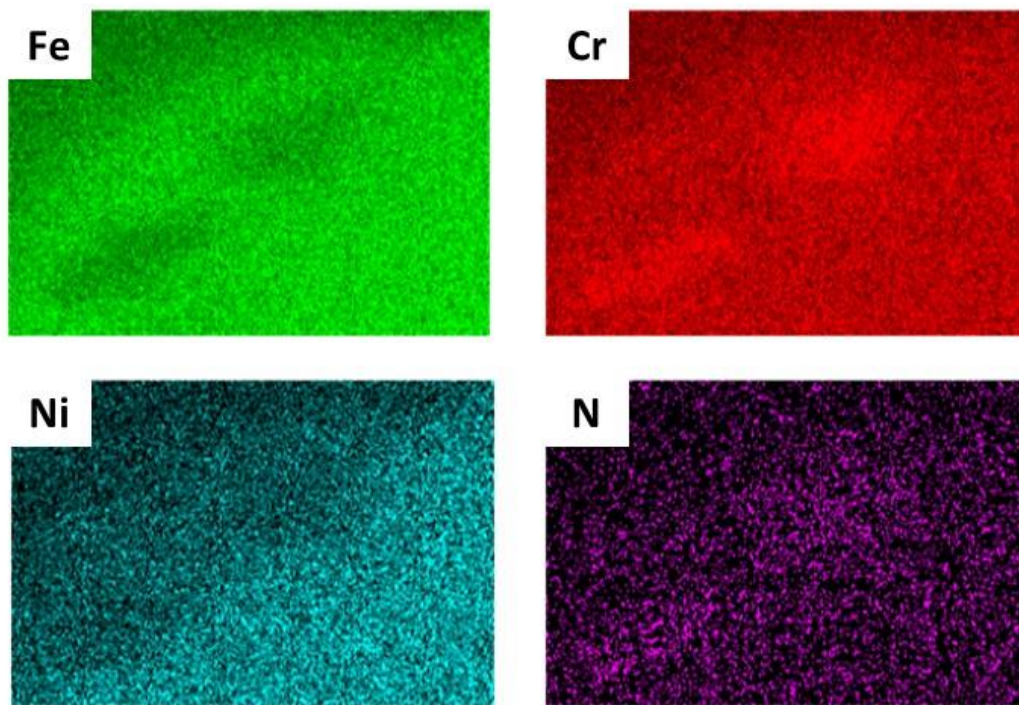
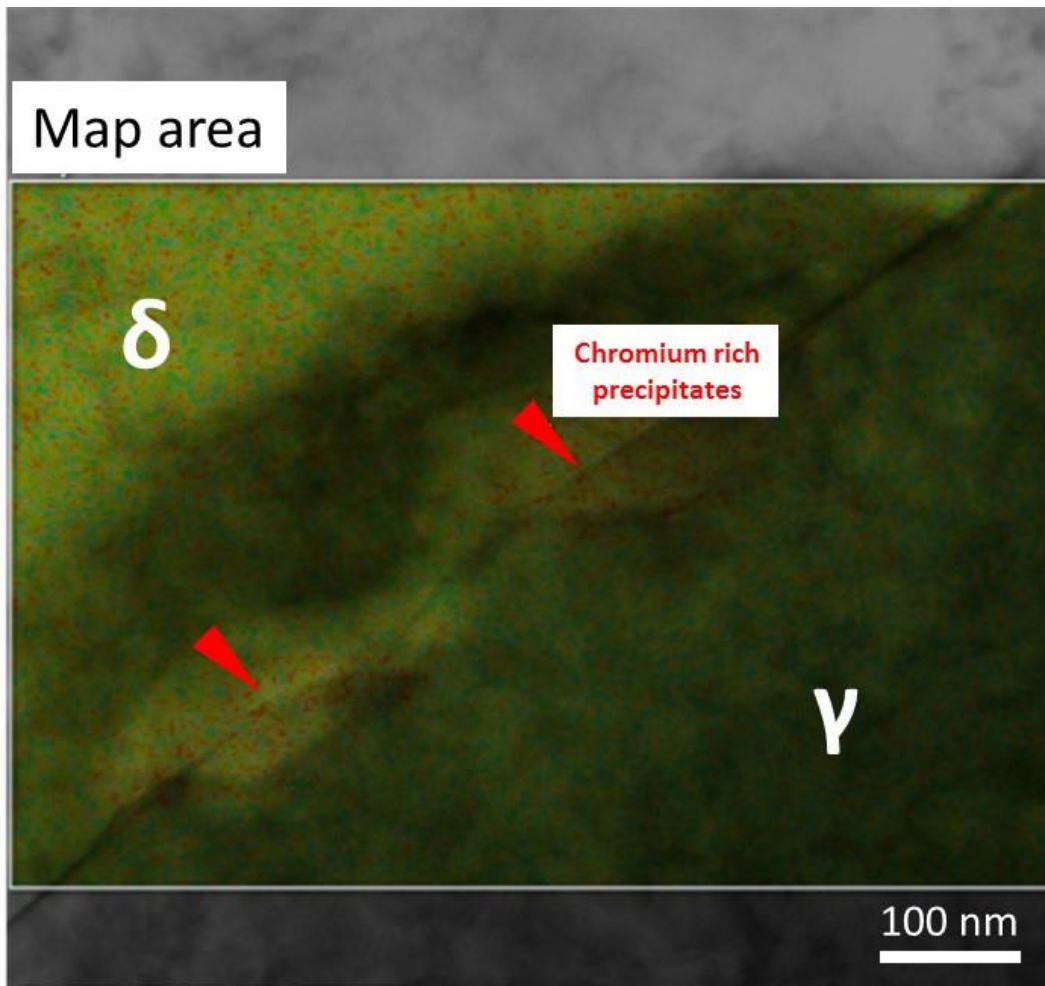


Figure 3-21 STEM image of chromium rich precipitates at a phase boundary; STM-EDS map scan is obtained from the masked area.

3.3.3.2 Precipitation of Cr_2N at ferrite-ferrite grain boundary

Figure 3-22 shows an array of Cr_2N precipitates along a ferrite-ferrite grain boundary.

These nano-size Cr_2N precipitates are closely aligned.

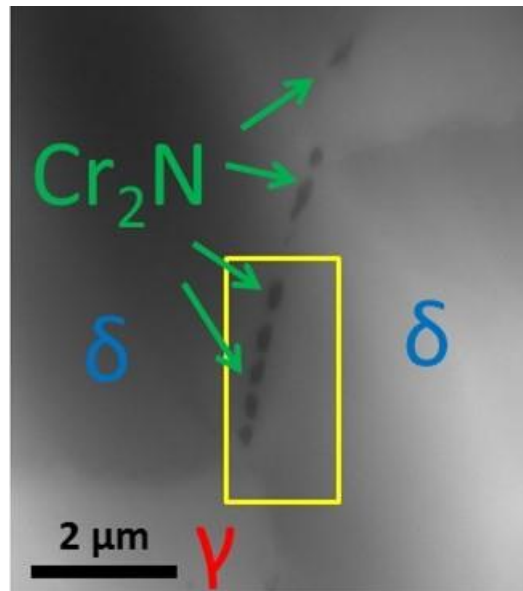


Figure 3-22 Cr_2N precipitates at a ferrite-ferrite grain boundary, imaged by BSE mode in SEM.

Figure 3-23 shows the experiment result of Cr_2N precipitates at a ferrite-ferrite grain boundary using TKD. The overall indexed rate of this TKD scan is over 95% with a step size of 20 nm. Figure 3-23 (a) shows that a close aligned Cr_2N array was identified at this ferrite-ferrite grain boundary. Figure 3-23 (b) is the grain boundary map which marks the grain boundaries with varies angles ranges. A misorientation profile is performed near this ferrite-ferrite grain boundary and the profile result is showed in Figure 3-23 (c). It can be seen the pixel to pixel misorientation values are lower than 2° except a low angel grain boundary with about 4° misorientation. Figure 3-23 (d) and (e) are KAM maps using first order and second order schemes, respectively. The second order scheme suggests a higher order of misorientation than first order scheme. The corresponding GND maps are shown in Figure 3-23 (f) and (g).

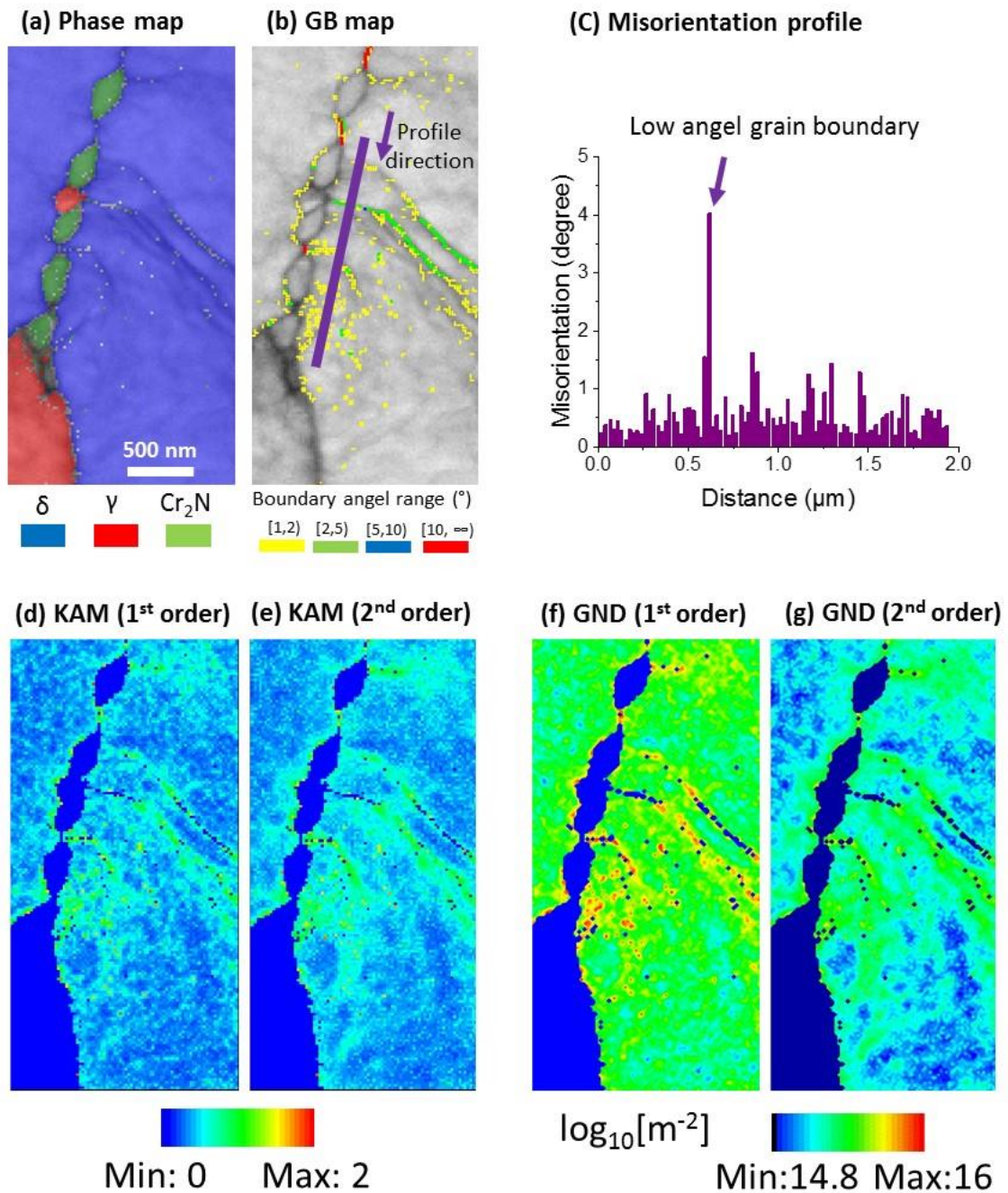


Figure 3-23 TKD Results of Cr_2N precipitates at a ferrite-ferrite grain boundary: (a) Phase map; (b) Grain boundary map, result of misorientation line profile is shown in (c); (d) and (e) are KAM maps using 1st and 2nd order scheme, respectively; (f) and (g) are GND maps using 1st and 2nd order scheme, respectively; invalid pixels of GND are shown in blue.

According to the GND distribution shown in Figure 3-23, in the regions near the Cr_2N , a high GND density is detected. This result shows that the GND of the adjacent region can be affected by the Cr_2N precipitates at the ferrite-ferrite grain boundary. Besides, as

Equation 1-3 suggested, the local material can be strengthened by the high dislocation density, which delivers a distinct mechanical property around Cr_2N precipitates.

3.3.3.3 Precipitation of Cr_2N at ferrite-austenite phase boundary

Figure 3-24 shows a TKD result of Cr_2N at a ferrite-austenite phase boundary. Figure 3-24 (a) shows the observed images using BSE modes. A dark contrast indicates Cr_2N precipitates. Figure 3-24 (b) shows the phase map of this phase boundary where several Cr_2N are detected. Figure 3-24 (c) and (d) shows KAM and GND density maps, respectively.

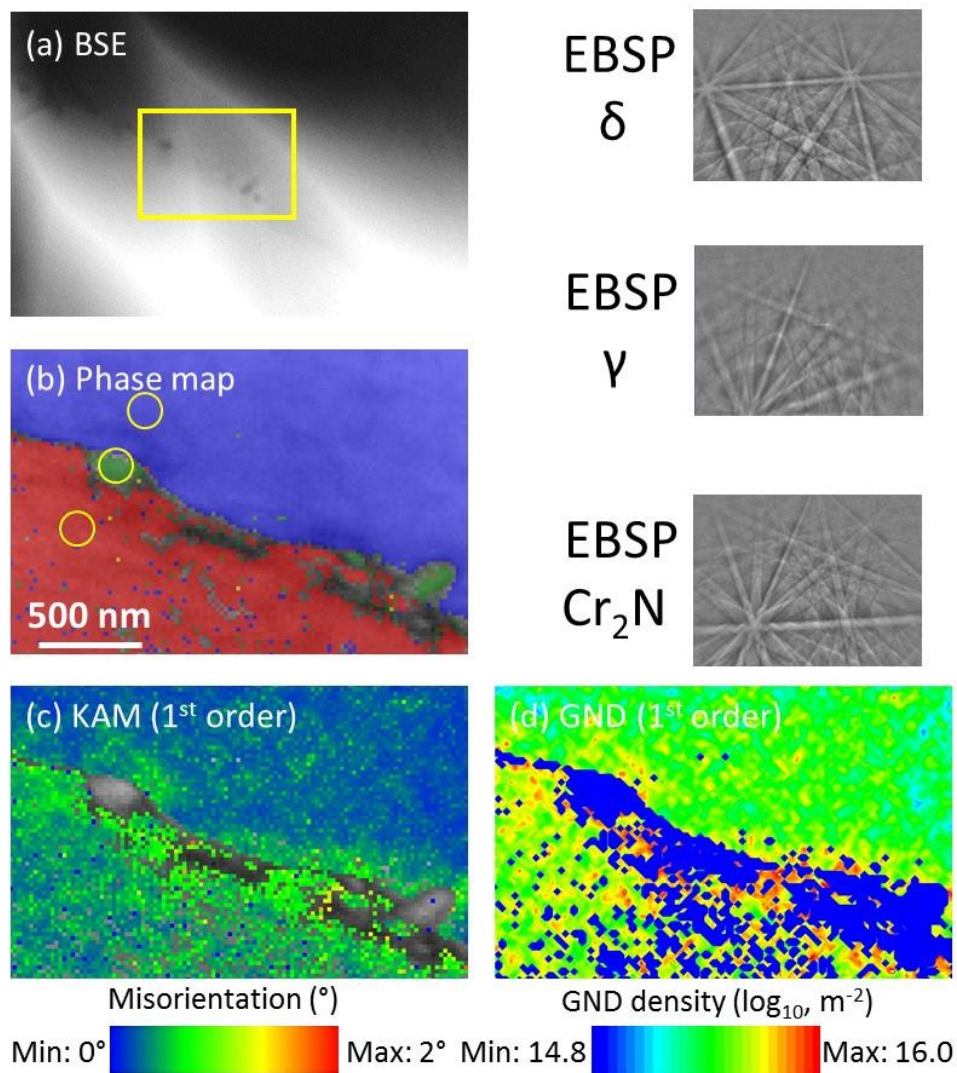


Figure 3-24 Cr_2N precipitates at a ferrite-austenite phase boundary; (a) BSE image and TKD scanning performed in yellow boxed area; (b) Phase map, EBSPs of ferrite, Cr_2N and austenite are shown on the right side; (c) KAM map and (d) GND map, calculated by first order scheme.

3.3.3.4 Chemistry of Cr₂N in weldment sample

Figure 3-25 shows a STEM image of formed Cr₂N precipitates. A 45.5 wt. % chromium content is measured for this Cr₂N. To further characterise the liner element evolution across the Cr₂N, an EDS line profile is performed. The result suggests a high chromium content in the Cr₂N and no obvious chromium depleted zone is detected around this Cr₂N.

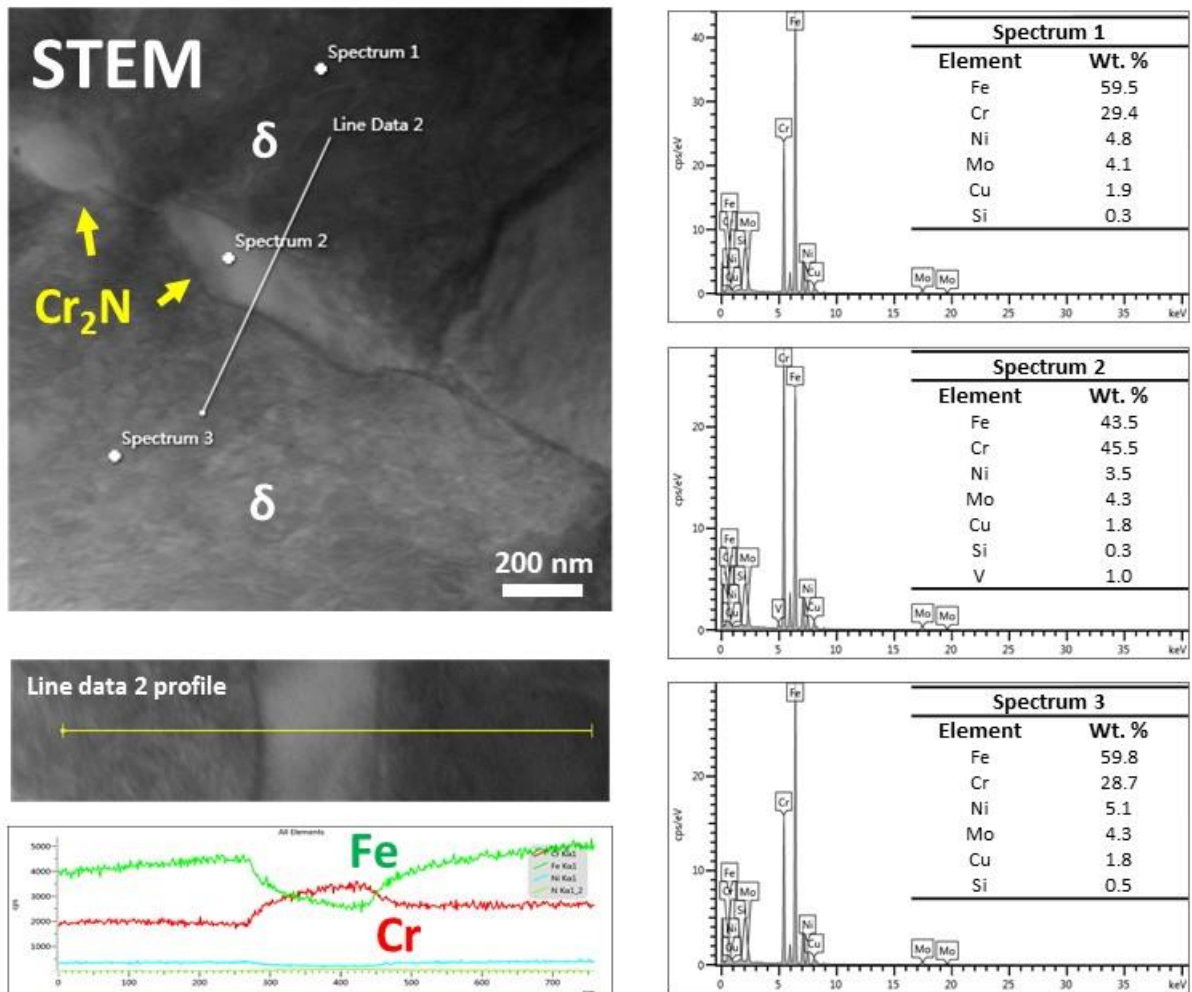


Figure 3-25 STEM-EDS results of a Cr₂N at a ferrite/ferrite grain boundary; a 45.5 wt. % chromium was examined from Cr₂N by using Point EDS; EDS line profile result of chromium, iron, nickel and nitrogen elements cross the Cr₂N is shown as above.

Figure 3-26 shows a TEM bright field image that a row of Cr₂N precipitates at a ferrite-ferrite grain boundary. Cr₂N precipitates are in dark contrast and the size of these Cr₂N precipitates are about 200 nm to 300 nm. Four SADPs are also obtained across a Cr₂N.

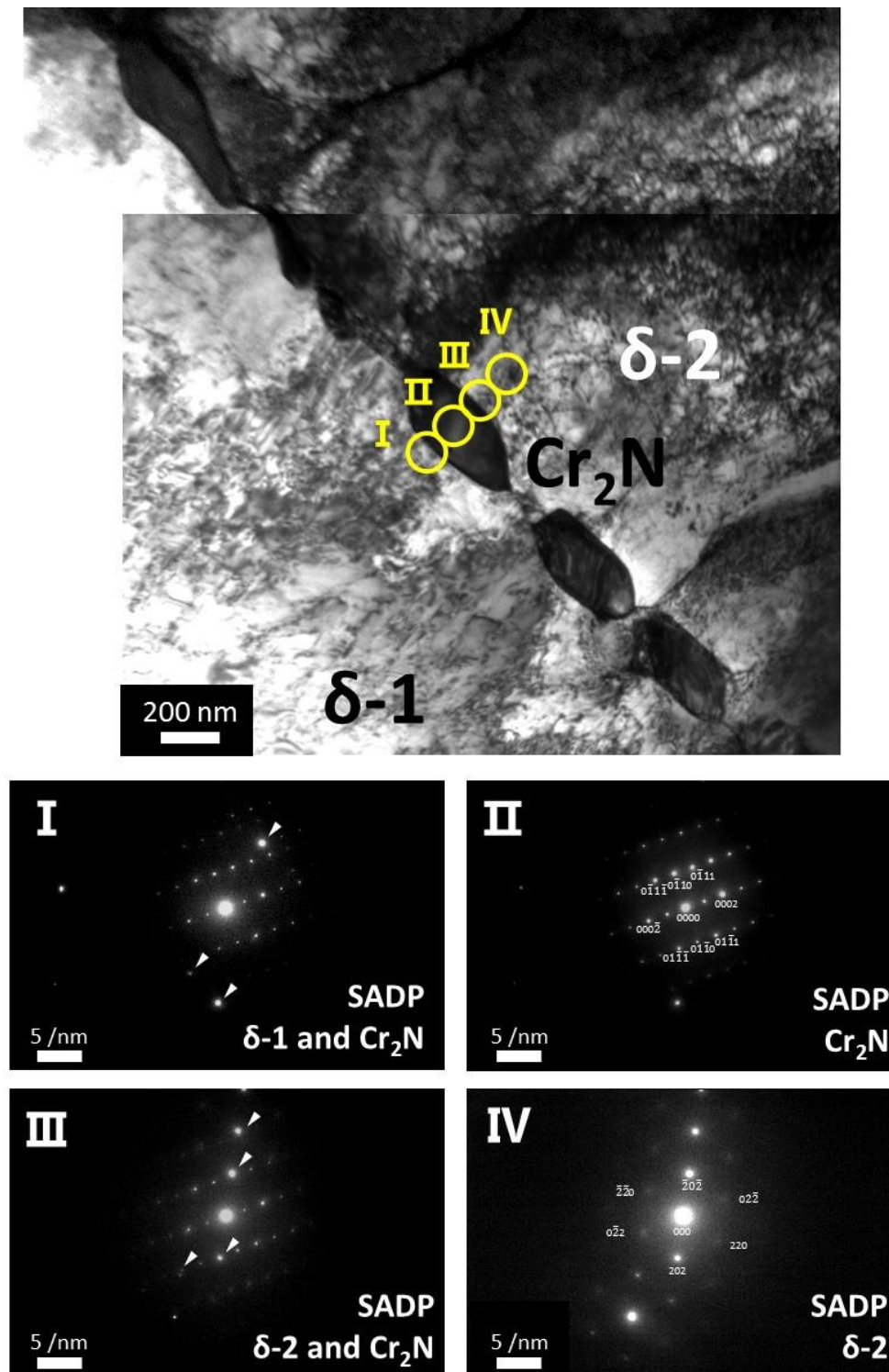


Figure 3-26 Cr₂N precipitates at a ferrite-ferrite grain boundary; SADP is obtained from yellow rings and results show in figures I to IV; white arrows point the diffraction spots from ferrite contribution.

3.3.3.5 Thermodynamics of chromium nitrides precipitation

Figure 3-27 shows a modelling result that Cr_2N precipitation at a ferrite-austenite phase boundary using Dictra package. The initiate temperature of modelling is 1473 K and a homogenisation of chromium and nitrogen is achieved before cooling. Then a cooling rate of 5 K/min is set for modelling. Initially, there is no phase change before 1025°C. When it comes to temperature range 1025-1000°C, Cr_2N start to precipitate with a dramatic element variation. The result suggests that, in the initiated Cr_2N , an over 85 wt. % chromium and over 10 wt. % nitrogen contents exist. With a further cooling, the Cr_2N starts coarsening and higher chromium and nitrogen contents are achieved in the Cr_2N .

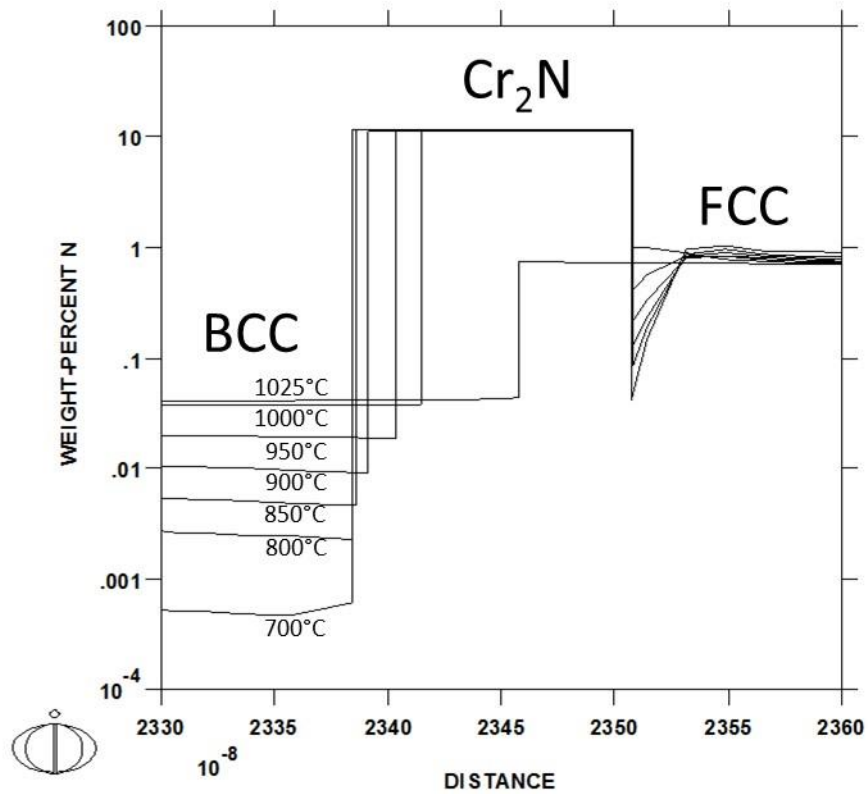
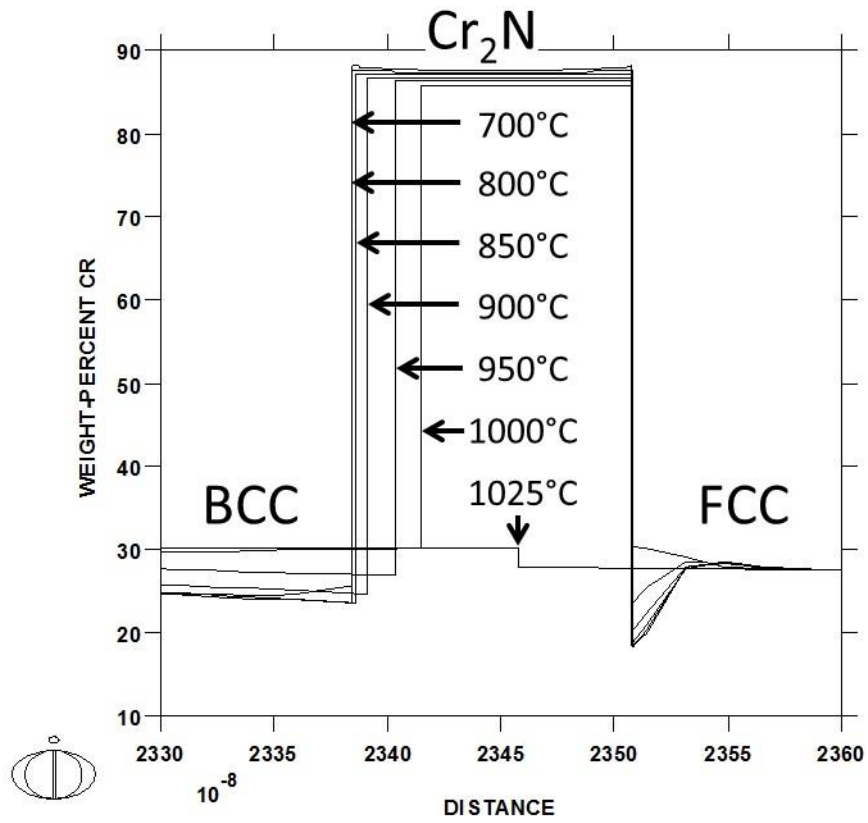


Figure 3-27 Dictra modelling of Cr_2N precipitation at a ferrite-austenite phase boundary; evolution of (a) chromium concentration and (b) nitrogen concentration; the unit of distance is a metre.

3.4 Chapter summary

In this Chapter, experiments of and results in precipitation and characterisation of σ phase, χ phase, nitrides and carbides in isothermal heat treatment samples and a weldment have been presented. Key outcomes are:

- The SEM results reveal a tiny amount of σ phase can be formed within 6 min ageing at 800°C. When the sample has 30 min ageing at 800°C, σ phase has an obvious precipitation at both grain boundaries and phase boundaries. Compared with σ phase, precipitation of χ phase is faster whose presence is detected in the sample with 6 min ageing at 800°C. A moderate increasing of precipitation volume is realised in samples with 30 min and 1-hour ageing at 800°C. This result is comparing well with the thermodynamic modelling of σ phase and χ phase evolution in such conditions.
- The volume and size of nitrides and carbides precipitation are small. In the sample with 30 min ageing at 800°C, the rod-like Cr_2N are preferred to precipitate at boundaries and in the ferrite matrix. Their dimensions are about 200 nm to 300 nm in length and tens of nanometres in width. A lamellar M_{23}C_6 is characterised at a phase boundary with a thickness of about 20 nm. The presentation of such M_{23}C_6 seems able to dramatically facilitate the Cr_2N precipitation.
- In the HAZ of the weldment, the precipitation of σ phase, χ phase and nitrides is detected. In addition, nano-size Cr_2N precipitates were characterised at both ferrite-ferrite grain boundaries and ferrite-austenite phase boundaries.

Chapter 4

Effect of hydrogen charging on dislocation multiplication in pre-strained super duplex stainless steel

Dislocations are one of common types of line defect in crystalline materials. A dislocation density of 10^{10} to 10^{12} m^{-2} exists in most annealed crystalline materials. However, this amount of intrinsic dislocation density does not always remain unchanged. For example, the plastic deformation can introduce more dislocations in materials because of the strain hardening phenomenon which has been reviewed in Section 1.3.2. Also, recent studies have reported that dislocation density can be increased by hydrogen charging.

In this chapter, the effect of hydrogen charging on dislocation multiplication in super duplex stainless steel is studied. Section 4.1 predicts the hydrogen concentration after hydrogen charging. Section 4.2 shows the results of dislocation density measurement in hydrogen-free and hydrogen-charged pre-strain samples. Section 4.3 discusses the effect of hydrogen charging on dislocation multiplication in pre-strained SDSS. Section 4.4 summaries the chapter.

4.1 Modelling of hydrogen concentration after hydrogen charging

Section 1.4.4 has discussed the diffusion behaviour of hydrogen in SDSS. Here, we apply Fick's law to model the hydrogen concentration against penetration depth. The following parameter is applied:

- Hydrogen diffusivity: $5.0 \times 10^{-15} \text{ m}^2/\text{s}$ (slowest limit), $1.0 \times 10^{-14} \text{ m}^2/\text{s}$ and $5.0 \times 10^{-14} \text{ m}^2/\text{s}$ (fastest limit)
- Surface hydrogen concentration: 40 ppm
- Bulk hydrogen concentration: 2 ppm
- Hydrogen charging time: 10 days

Figure 4-1 shows the modelling result of hydrogen concentration through the 1.2 mm thickness of this sample. This result suggests the hydrogen can be critically charged to reach the centre of samples. Therefore, in this work, it is validated that the samples with 1.2 mm thickness can pick up hydrogens with 10 days charging.

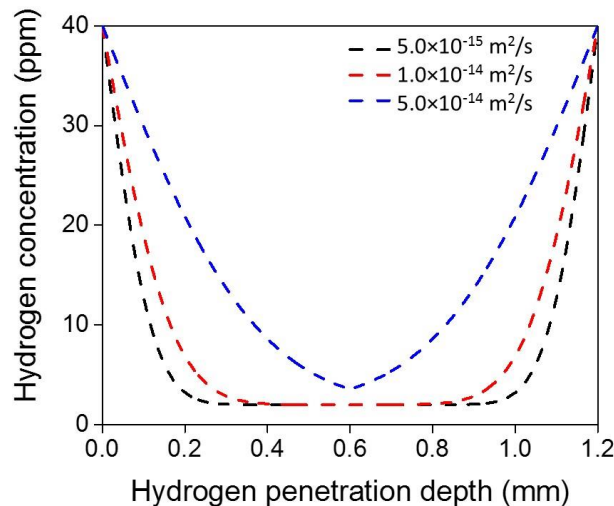
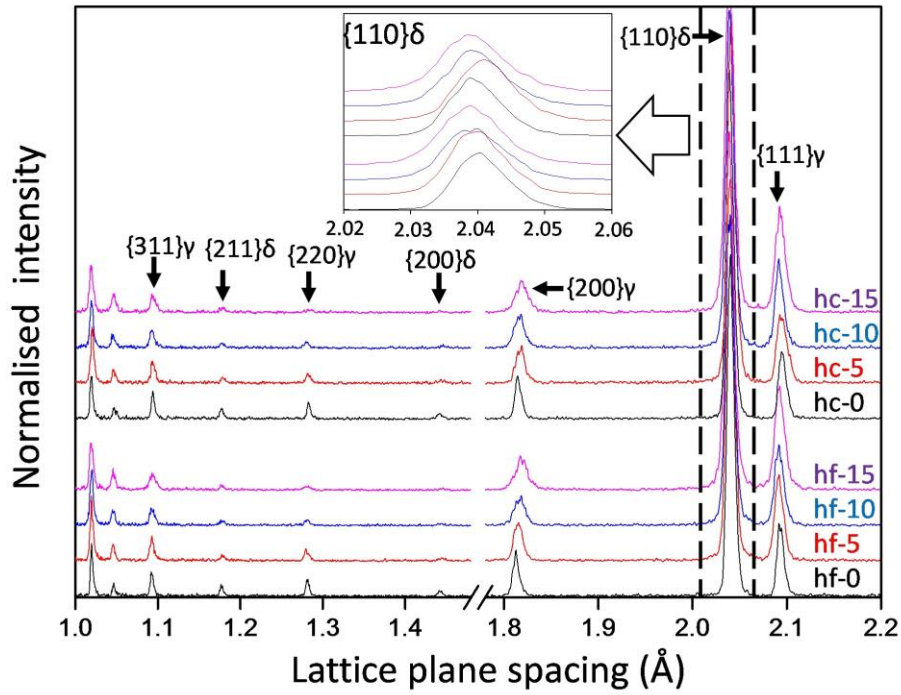


Figure 4-1 Hydrogen concentration against sample depth with 10 days hydrogen charge. Hydrogen diffusivity values of $5.0 \times 10^{-15} \text{ m}^2/\text{s}$, $1.0 \times 10^{-14} \text{ m}^2/\text{s}$ and $5.0 \times 10^{-14} \text{ m}^2/\text{s}$ are applied for modelling. Hydrogen concentrations of 40 ppm and 2 ppm is assumed for surface and bulk, respectively.

4.2 Results of dislocation density as a function of pre-strain

Figure 4-2 shows the TOF neutron diffraction data. North bank collects diffraction signals along the longitudinal sample direction, where peaks of $\{111\}\gamma$ and $\{110\}\delta$ have strong signals. Due to this sample texture effect, peaks of $\{111\}\gamma$ and $\{110\}\delta$ were selected for dislocation density determination from North bank. From the South bank signal, the dislocation density of δ -ferrite was linearly averaged from the values of dislocation density determined from peaks of $\{110\}$, $\{200\}$ and $\{211\}$, while peaks of $\{111\}$, $\{200\}$, $\{220\}$ and $\{311\}$ were chosen for austenite. The total dislocation density was calculated by averaging the measured values of dislocation density from both longitudinal and transverse directions.

(a) Longitudinal



(b) Transverse

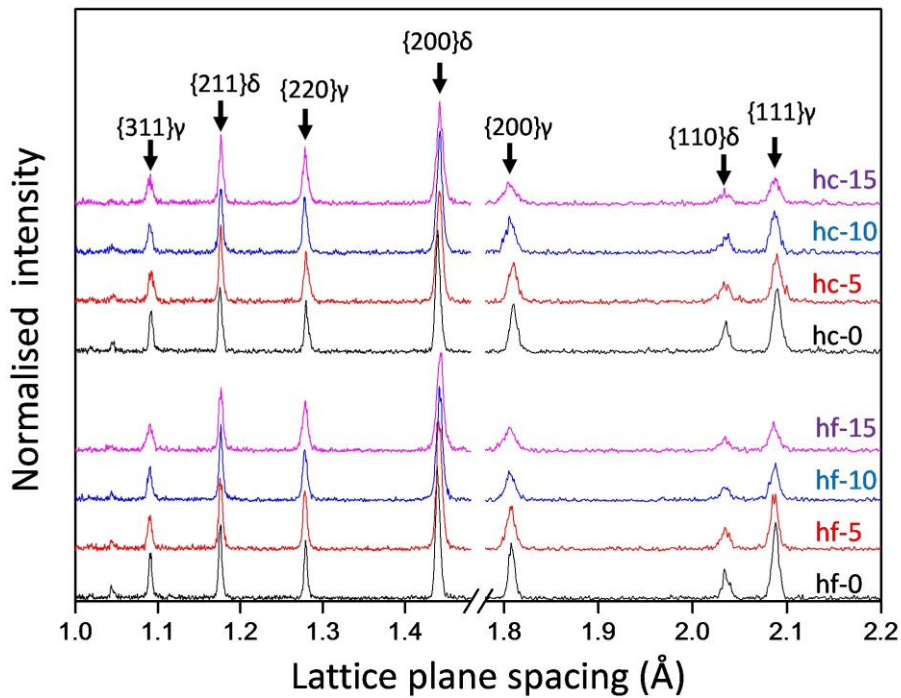


Figure 4-2 Neutron diffraction spectrum patterns of (a) lattice plane normal to sample longitude direction, signal collected from North bank; (b) lattice plane normal to sample transverse direction, signal collected from South bank. Abbreviations of hf and hc stand for hydrogen free and hydrogen charged, respectively. The numbers 0, 5, 10, and 15 represent the percentage of pre-strain.

Figure 4-3 shows the dislocation density results for austenite and ferrite, with different pre-strain and hydrogen charging conditions. The application of pre-strain can strength the material by introducing more dislocations in the material according to the dislocation strengthening mechanism. In the unstrained sample, an order of 10^{13} m^{-2} dislocation density was introduced into the austenite phase after hydrogen charging. Meanwhile, the dislocation density in ferrite increased, albeit to a lesser degree, resulting in a dislocation density of $5 \times 10^{12} \text{ m}^{-2}$. A similar trend was revealed in the samples with 5% pre-strain. Such results suggest that solute hydrogen increases dislocation density for both austenite and ferrite. However, when 10% or 15% of pre-strain was applied, the hydrogen has insignificant effect on increasing dislocation density in both austenite and ferrite.

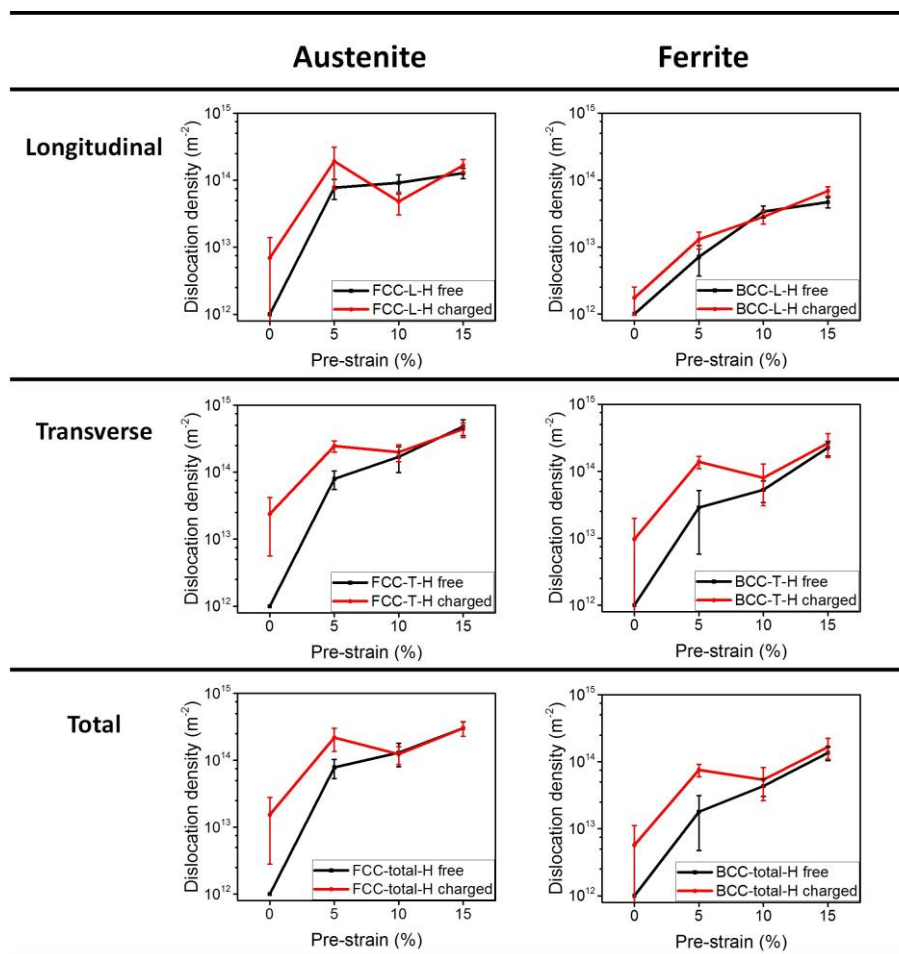


Figure 4-3 Dislocation density in austenite (face centre cubic, FCC) and ferrite (body centre cubic, BCC) as a function of different pre-strain; abbreviation of L and T strand for longitudinal and transverse, respectively; overall dislocation density is calculated by linearly averaging the values of dislocation density determined from both directions.

4.3 The multiplication and annihilation of dislocation

In metals, defects can be removed or rearranged by changes of stress or thermal states. A multiplication of dislocations can also be triggered by sources of Frank-Read, double cross slip, vacancy disc and boundaries [137]. Meanwhile, the dislocation annihilation takes the place when a dislocation slips off from the material or when a positive dislocation encounters a negative dislocation. The summation of dislocation multiplication and annihilation is referred to as materials dynamic recovery.

4.3.1 Athermal storage of dislocation

The stored dislocation density is calculated at equilibrium of athermal storage of dislocation and recovery [138]:

$$\frac{d\rho}{d\varepsilon} = \frac{d\rho^+}{d\varepsilon} + \frac{d\rho^-}{d\varepsilon} \quad (6-1)$$

Where the term $d\rho^+/d\varepsilon$ is dislocation multiplication and term $d\rho^-/d\varepsilon$ is dislocation annihilation. The change of dislocation density can be achieved by imbalance between dislocation multiplication and annihilation.

4.3.2 Source of dislocation multiplication

According to Figure 4-3, the dislocation multiplication is detected within no pre-strain and 5% pre-strain samples for both ferrite and austenite. In SDSS, the Frank-Read type source is suggested to account for dislocation density multiplication [77]. The critical shear stress required to activate the source is:

$$\tau = u \frac{2Gb}{l_d} \quad (6-2)$$

Where G is the shear modulus, l_d is the segment length and u is the unit of dislocation line energy.

Residual interface stress always exists due to the property differences between the austenite and ferrite phases. In as-quenched SDSS, austenite has a tensile stress and ferrite has a compressive stress [139]. Kirchheim et al. [12, 140] suggest the dislocation line energy can be reduced by the presence of solute hydrogen. Therefore, the critical shear stress required for the Frank-Read source is reduced, thus leading to dislocation multiplication.

Nevertheless, the increased dislocation length from Frank-Read dislocation source can be hindered in the samples with 10% and 15% pre-strain. A quenching process can introduce a residual stress between ferrite and austenite in SDSS [139]. This residual stress is important for Frank-Read dislocation source multiplication in samples without pre-strain and 5% pre-strain. By comparison, in the samples with 10% and 15% pre-strain, a large-scale plastic deformation is introduced. Johansson et al. [141] reported that the plastic deformation in ferrite and austenite behaves homogeneously at high macroscopic strains. Therefore, the introduced plastic deformation can diminish the residual stress between the two phases from the as-quenched condition. During the releasing of loading, as the mechanical properties of ferrite and austenite are close at the room temperature [141, 142], the releasing of loading can lead to a low residual stress state in samples with 10% and 15% pre-strain. As a result, the source of dislocation multiplication is reduced and achieves an equality of dislocation multiplication and annihilation in the samples with 10% and 15% pre-strain.

4.3.3 Saturation of dislocation density

Kocks and Mecking [143] proposed a systematic model to evaluate dislocation density within conditions of varying temperature and strain. If we only consider the strain effect, the net storage rate of dislocation can be written as [143-145]

$$\frac{d\rho}{d\varepsilon} = M_T(k_1\sqrt{\rho} - k_2\rho) \quad (6-3)$$

Where M_T is Taylor's factor. k_1 is storage constant. k_2 is dynamic recovery constant which is proportional to the critical dislocation annihilation distance. Both k_1 and k_2 are positive values. As $k_2\rho$ possesses a higher order of term ρ than $k_1\sqrt{\rho}$, with increasing strain, the increase of dislocation density tends to slow down and finally achieve a dislocation saturated status. In the present study, hydrogen is showed to give a rise to an increase in dislocation density in unstrained and 5% pre-strained samples, but not after the application of 10% and 15% pre-strain, which is likely due to this dislocation saturation phenomenon.

4.4 Chapter summary

In this Chapter, study and results on effects of hydrogen charging on dislocation multiplication in pre-strained SDSS are presented. Key outcomes are:

- With the concentration of solute hydrogen, the activation of dislocation multiplication in super duplex stainless steel is a function of pre-strain. The multiplication of dislocation density occurs in samples with less than 5% pre-strain. The dislocation multiplication is hampered when the level of pre-strain reaches 10%.
- The condition of residual stress in SDSS is important for dislocation multiplication. It is proposed that, in samples with less than 5% pre-strain, the dislocation multiplication can be activated by the residual stress from the as-quenched condition. In contrast, in samples with more than 10% pre-strain, the residual stress can be diminished by the large-scale plastic deformation. Consequently, the source of dislocation multiplication is reduced in samples with 10% and 15% pre-strain.
- The theory of dynamic recovery can be applied to depict the evolution of dislocation density in pre-strained SDSS. Hydrogen activates the dislocation multiplication in samples with less than 5% pre-strained samples, but not after the application of 10%

and 15% pre-strain. This implies a dislocation saturation phenomenon with a greater pre-strain.

Chapter 5

Effect of hydrogen on crack propagation

SDSS possess about half ferrite and half austenite. Though the two phases have similar mechanical property, they exhibit different resistance to hydrogen embrittlement. In the past decades, a number of studies have been published in the area of the fracture behaviour of SDSS with hydrogen solute. It has been found that ferrite is sensitive to HAC while austenite acts as hydrogen trapping and crack trapping phase to HAC, the mechanism of crack nucleation and crack propagation is still not clear in these duplex structure materials.

In this Chapter, the effect of hydrogen on the fracture behaviour of SDSS is investigated using EBSD. Section 5.1 discusses the effect of hydrogen on fracture behaviour in SDSS. Section 5.2 shows the EBSD characterisation result of microcrack in SDSS samples with and without hydrogen. Section 5.3 discusses the trapping mechanism of crack in both austenite and ferrite in SDSS. Section 5.4 summaries the chapter.

5.1 Hydrogen assisted crack propagation in SDSS

Fracture behaviour in SDSS is complex because both of ferrite and austenite are in the microstructure. The ferrite and austenite behave distinctly differently in HAC. In SDSS, it has been suggested that ferrite has lower resistance to hydrogen embrittlement than austenite [2, 5, 51, 146]. In hydrogen environment, a dominant fracture mechanism is a cleavage for ferrite and ductile micro-mechanism rules the fracture along austenite grains [147]. Austenite has a higher capability to trap secondary crack tips than ferrite [148]. Though these studies have provided a general understanding of HAC in SDSS, the mechanism of HAC propagation is still not clear, e.g. the crack propagation and trapping mechanism. In this work, the EBSD is engaged to study the HAC propagation and trapping mechanism in SDSS.

5.2 Effect of hydrogen on cleavage behaviour

In this section, the characterisation result of samples following slow strain rate tests, with and without hydrogen, will be shown and discussed with respect to HAC propagation and trapping mechanism in SDSS.

5.2.1 Fracture behaviours in hydrogen free and hydrogen charged samples

A distinct fracture behaviour can be observed in the necking area of hydrogen free and hydrogen charged samples after tensioning. Figure 5-1 shows the fracture on the side surface in the necking area of hydrogen free sample after tensioning using optical microscopy (OM). As can be seen the shear marks are formed towards the fracture surface, demonstrating the good plasticity of sample without hydrogen. Also, there are few secondary cracks can be observed, which also suggests this sample possesses a good plasticity.

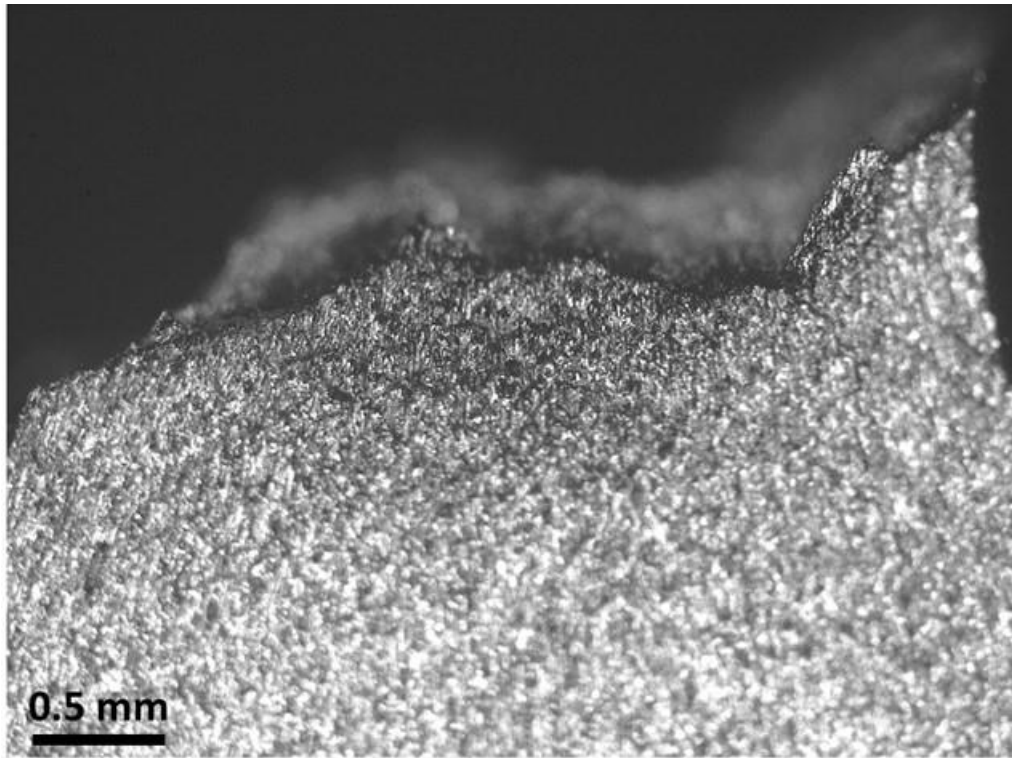


Figure 5-1 Fractures on the side surface in the necking area of hydrogen free sample after tensioning, imaged by OM; stress was applied vertically.

Figure 5-2 shows the fracture behaviour in the necking area of hydrogen charged sample after tensioning. The width of this necking is much wider than it shows in hydrogen free sample. Meanwhile, a high density of secondary cracks lies horizontally near the fracture surface. These two facts indicate a plasticity loss in the hydrogen charged sample.

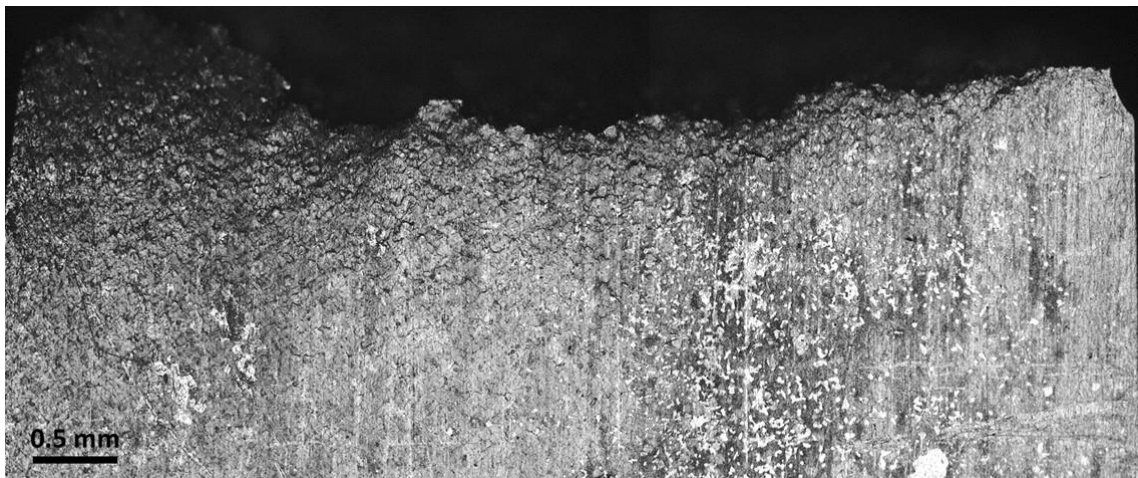


Figure 5-2 Fractures on the side surface in the necking area of hydrogen charged sample after tensioning, imaged by OM; stress was applied vertically.

5.2.2 EBSD result of fracture behaviour in hydrogen free sample

Figure 5-3 shows an EBSD result of a crack tip in a hydrogen free sample. In this EBSD scanned area, a microcrack was identified in a ferrite grain which located between two austenite grains. The crack direction points to the sample fracture surface and has an approximately 30° inclined angle to tensile direction. Figure 5-3 (a) shows a SEM secondary electron (SE) micrograph where a crack was identified. Figure 5-3 (b) shows the indexed phase map. The index rate in ferrite is much higher than in austenite. Figure 5-3 (c) and (d) show the KAM maps using 1st order and 2nd order calculation schemes, respectively. Figure 5-3 (e) and (f) show the calculated GND density maps using 1st order and 2nd order calculation schemes, respectively. According to Figure 5-3 (e), two dislocation emission lines were characterised, where a high GND density $> 10^{15} \text{ m}^{-2}$ was measured ahead of the crack tip.

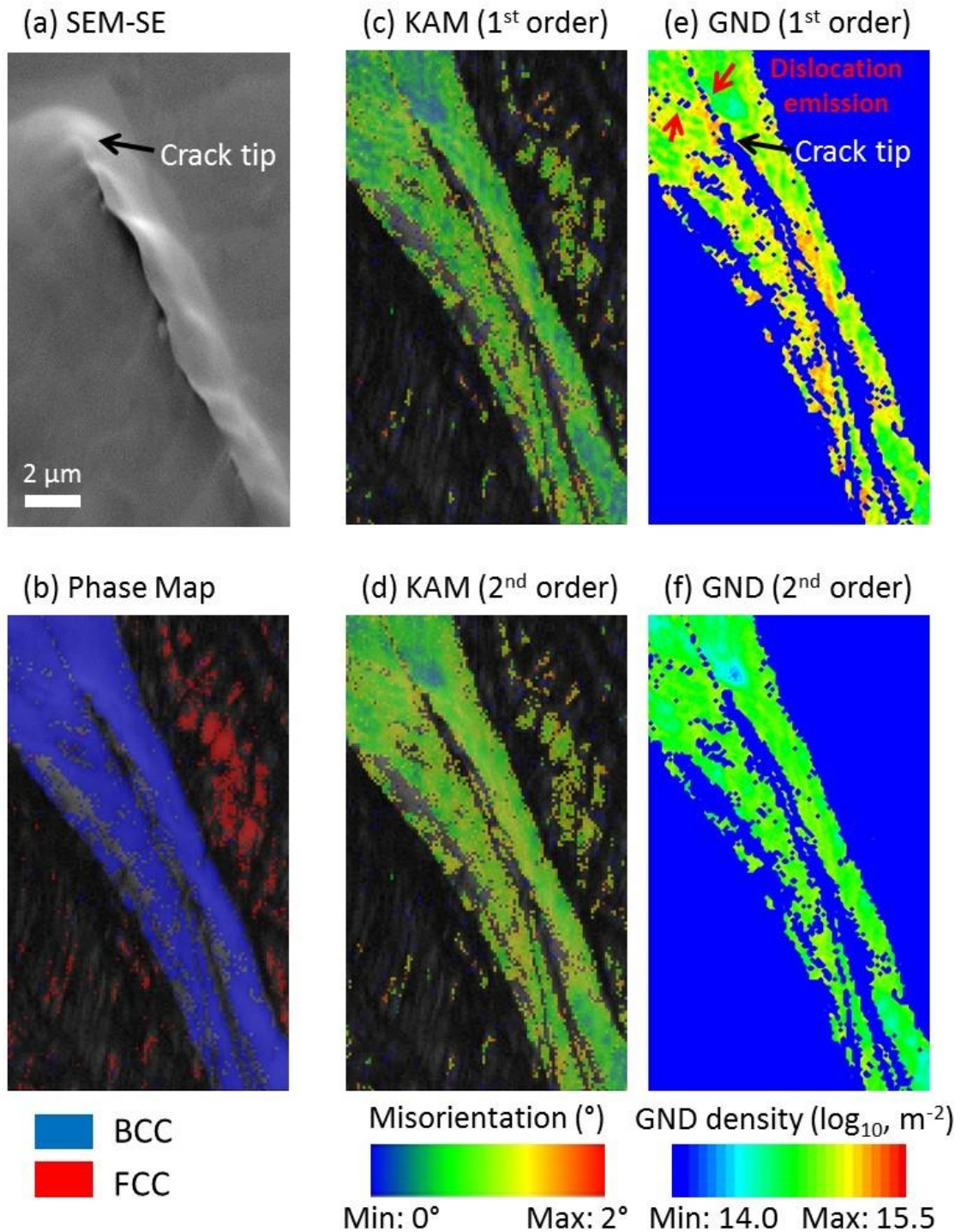


Figure 5-3 EBSD maps of a crack tip in a hydrogen free sample: (a) SEM-SE micrograph ; (b) Phase map; (c) and (d) are KAM maps using first order and second order calculation schemes, respectively; (e) and (f) are calculated GND density using first order and second order schemes, respectively. Invalid GND density values are shown in blue. Tensile stress applied vertically.

Figure 5-4 shows another EBSD result of a crack tip in a hydrogen free sample. Like the previous result in Figure 5-3, the crack exists in a ferrite grain. Figure 5-4 (a) shows the SEM-SE micrograph. A dark contrast area is measured ahead of the crack tip, which means

a severe plastic deformation exists in the local area. Figure 5-4 (e) and (f) show GND density maps using 1st order and 2nd order schemes, respectively. This result shows a high GND density ahead of this crack tip.

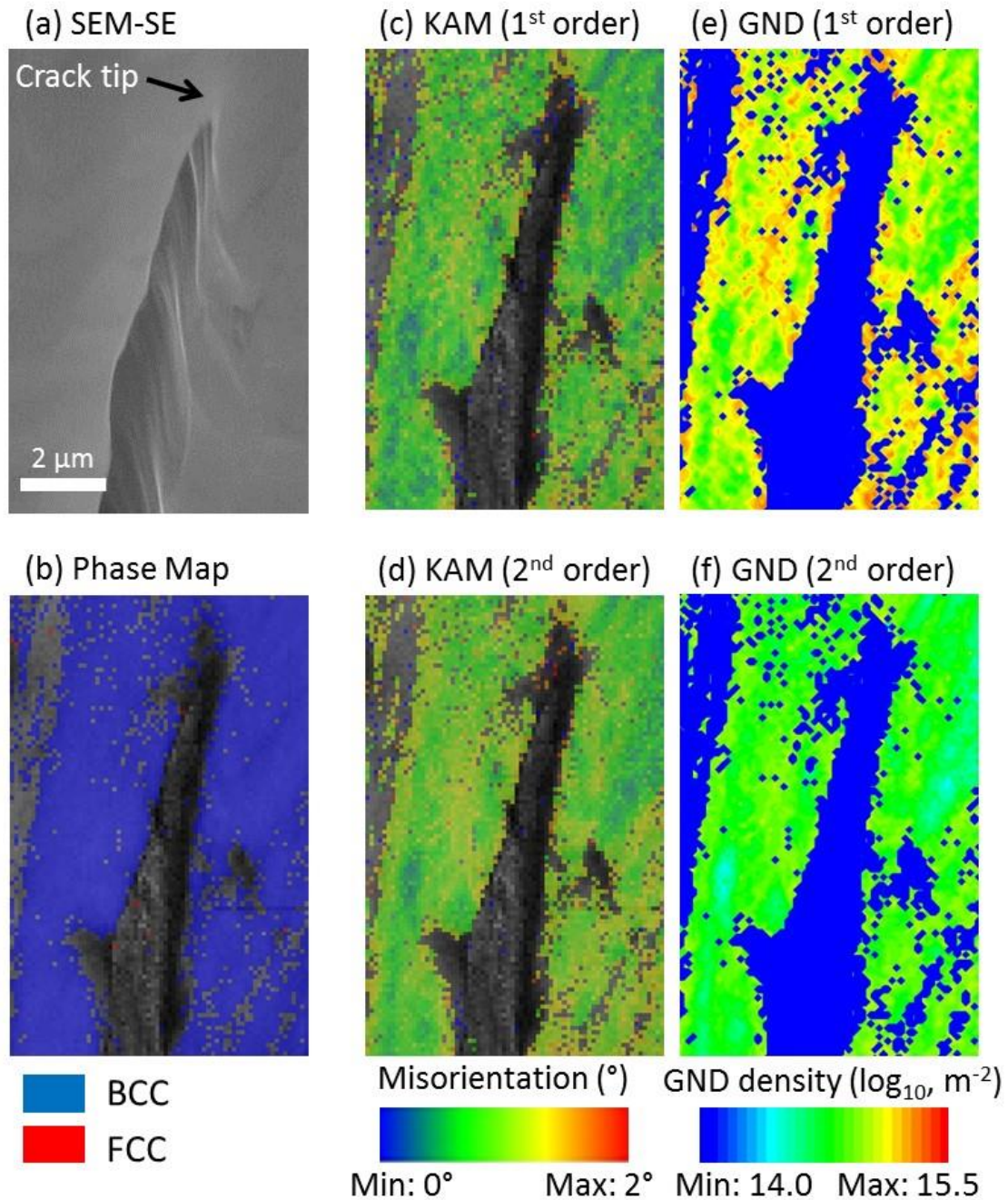


Figure 5-4 Another EBSD scan result of a crack tip in a hydrogen free sample: (a) SEM-SE micrograph; (b) Phase map; (c) and (d) are KAM maps using first order and second order calculation schemes, respectively; (e) and (f) are calculated GND density using first order and second order schemes, respectively. Invalid GND density values are shown in blue. Tensile stress applied vertically.

5.2.3 EBSD of fracture behaviour in hydrogen charged sample

Section 5.2.2 shows the EBSD characterisation results of microcrack tips in hydrogen free SDSS sample. Here, the EBSD characterisation results of microcrack tips in hydrogen charged SDSS sample is presented to compare with the previous results.

5.2.3.1 Characterisation of crack propagation at mesoscale

Figure 5-5 shows an EBSD result (1 μm scanning step size) of a crack in the hydrogen charged sample after slow strain rate test. Figure 5-5 (a) shows that cracks lie horizontally on the surface. Figure 5-5 (b) shows phase map of this crack. In general, they propagated throughout ferrite phase and the crack tips can get trapped in austenite grains.

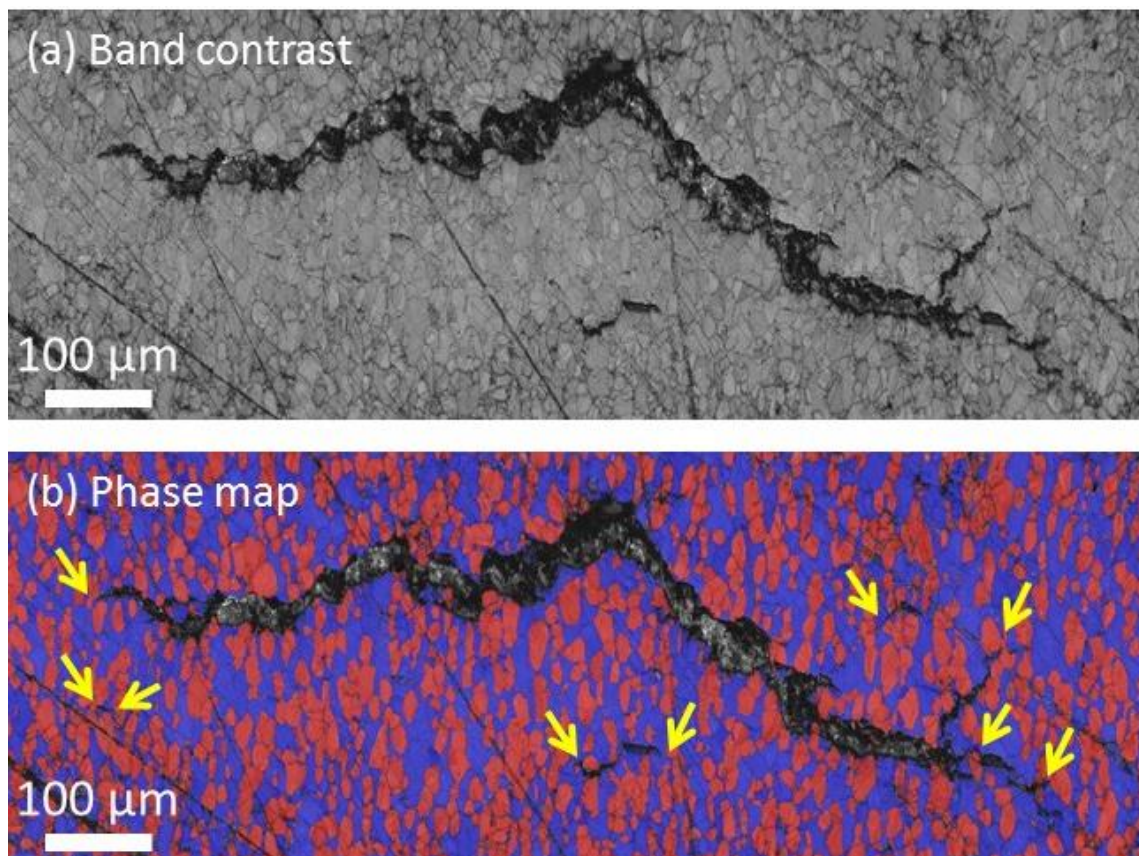


Figure 5-5 EBSD characterisation of a mesoscale crack in the hydrogen charged sample after tensioning: (a) band contrast map; (b) Phase map, the ferrite phases are in blue and austenite phases are in red; yellow arrows point to crack tips which get trapped in the austenite phase. Tensile stress applied vertically.

5.2.3.2 Trapping of crack propagation in austenite phase

Figure 5-6 shows an EBSD result that a microcrack gets trapped in austenite in the hydrogen charged sample after tensioning. This transgranular microcrack nucleates from ferrite and finally penetrates an austenite grain. At this crack tip, two microstructure changes are observed. Figure 5-6 (c) shows that a sub-grain boundary is formed above the crack tip whilst dislocations are emitted along a bottom line where a high dislocation $>10^{15}$ m^{-2} density is measured. Besides, a special $\Sigma 3$ grain boundary was measured ahead of the crack tip according to the CSL grain boundary plot in Figure 5-6 (d).

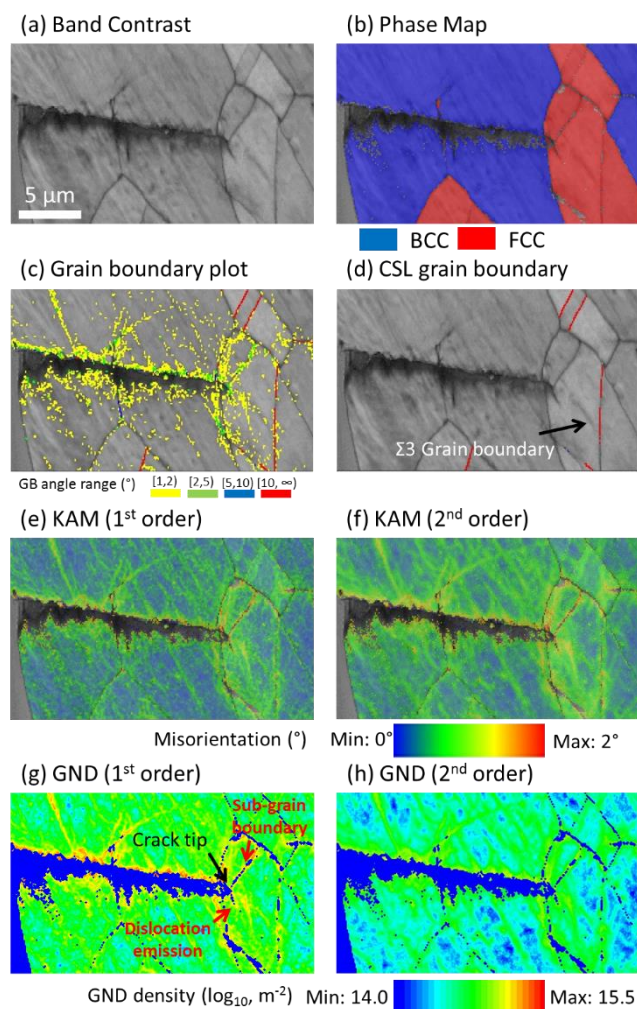
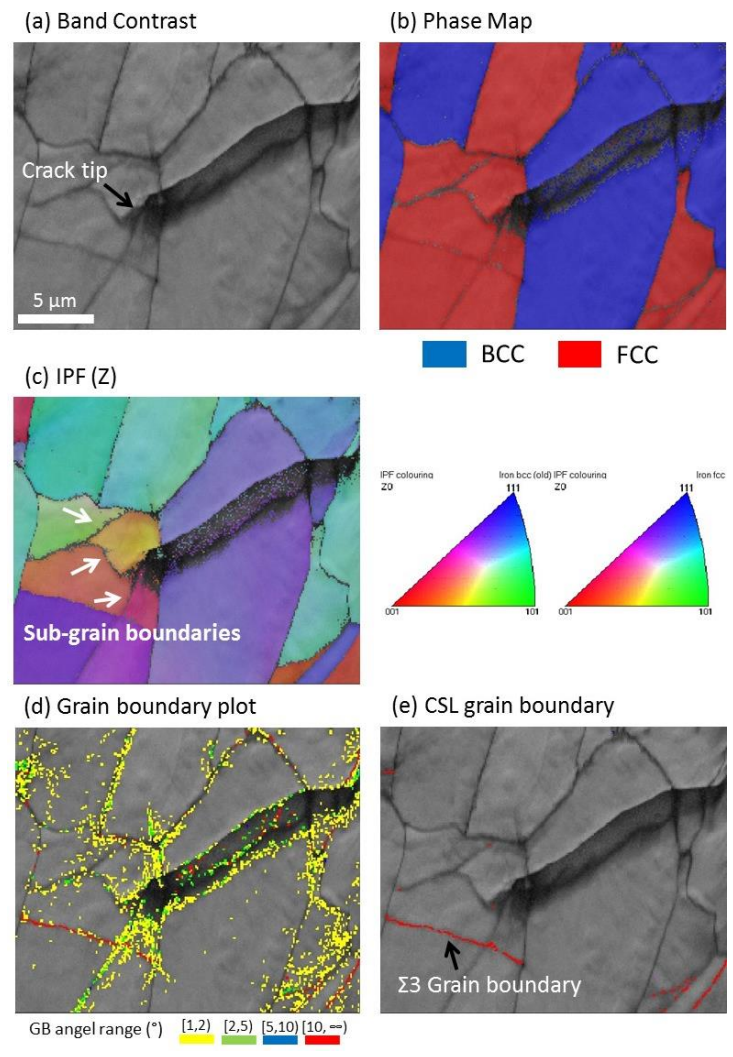


Figure 5-6 EBSD result of a microcrack that gets trapped in austenite in the hydrogen charged sample after tensioning: (a) Band contrast; (b) Phase map; (c) Grain boundary plot; (d) CSL grain boundary; (e) and (f) KAM map using first order and second order calculation schemes, respectively; (g) and (h) are calculated GND density using first order schemes and second order calculation schemes, respectively. Invalid GND density values are shown in blue. Tensile stress applied vertically.

Figure 5-7 shows an EBSD result of austenite sub-grain boundary formation in the hydrogen charged sample after tensioning. According to Figure 5-7 (b), this microcrack propagates through ferrite and get trapped in the austenite phase. Figure 5-7 (c) and (d) shows the IPF (Z) colour map and grain boundary plot where several secondary grain boundaries are measured ahead of the crack tip. Figure 5-7 (e) shows a $\Sigma 3$ grain boundary formed ahead of this crack tip, which shows a similar result as in Figure 5-6. This result suggests that the formation of sub-grain boundaries can hinder the crack propagation. According to the GND density maps in Figure 5-7 (f) and (g), there is no obvious trace of dislocation emission lines presented in austenite grains ahead of this crack tip.



(Figure continue to next page)

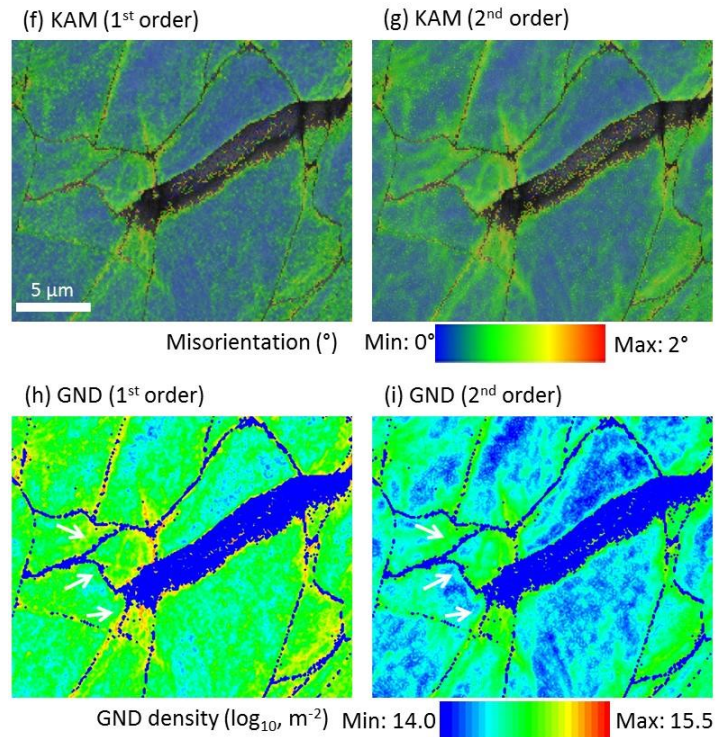


Figure 5-7 EBSD result of sub-grain boundary formation in austenite in the hydrogen charged sample after tensioning: (a) Band contrast; (b) Phase map; (c) IPF (Z) map; (d) Grain boundary plot; (e) CSL grain boundary plot; next page, (f) and (g) are KAM maps using first order and second order calculation schemes, respectively; (h) and (i) are calculated GND density using first order and second order schemes, respectively. White arrows in (c) and (h) point to the formed secondary grain boundaries. Invalid GND density values are shown in blue. Tensile stress applied vertically.

5.2.3.3 Trapping of crack propagation in ferrite

Figure 5-8 shows an EBSD result that a microcrack gets trapped in a ferrite grain boundary in the hydrogen charged sample after tensioning. According to the map in Figure 5-8 (e), an area with high GND density $>10^{15} \text{ m}^{-2}$ is measured. This result suggests that dislocation emission occurred ahead of the crack tip, which is a sign that crack tip blunted. Thus, the crack gets trapped at this ferrite grain boundary.

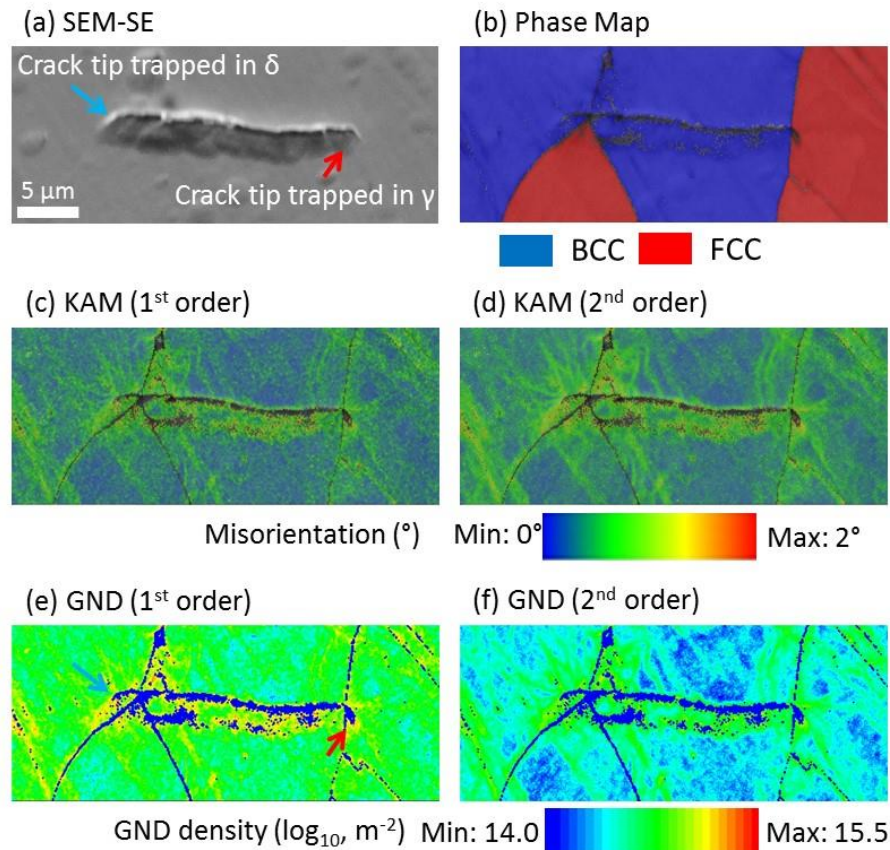


Figure 5-8 EBSD result of a microcrack that gets trapped at a ferrite grain boundary in the hydrogen charged sample after tensioning: (a) SEM-SE micrograph; (b) Phase map; (c) and (d) are KAM maps using first order and second order calculation schemes, respectively; (e) and (f) are calculated GND density using first order and second order schemes, respectively. Invalid GND density values are shown in blue. Tensile stress applied vertically.

5.3 Trapping mechanisms of hydrogen assisted crack propagation

In Section 5.2, results of study on several micro-cracks with respect to the trapping of crack propagation are presented. According to these results, it can be concluded that austenite has higher resistance to HAC than ferrite.

5.3.1 GND density distribution ahead of crack tip

In the hydrogen free sample, a high GND density $>10^{15} \text{ m}^{-2}$ distribution is measured ahead of crack tips in ferrite grains, as shown in Figure 5-3 and Figure 5-4. This high GND density indicates a large-scale plastic deformation at a location where the crack tip is blunted locally which leads to conclusion that the activation of dislocations emission can hamper the crack propagation. Compared with the crack characterised in ferrite in hydrogen

charged sample, the dislocation emission has not been detected ahead of the crack tips. Therefore, the formed the sharp crack tip can be easily advanced by the concentrated stress. Compared with ferrite, austenite exhibits a better plasticity even with hydrogen concentration. In Figure 5-3 (a), though austenite has a low EBSP index rate, the band contrast map shows austenite has a high density of slip or shear bands after tensioning. The formation of these bands implies that austenite has a good plasticity without hydrogen. After SDSS gets hydrogen charged, as shown in results from Figure 5-5 to Figure 5-8, the austenite can trap cracks when crack propagated into it. The activation of dislocation emission or the formation of the sub-grain boundary can impede the crack propagation. A high dislocation density $>10^{15} \text{ m}^{-2}$ is measured in an area with dislocation emission.

5.3.2 Crack trapping mechanisms in SDSS with hydrogen concentration

In SDSS, the dominant trapping mechanism of hydrogen assisted crack is the crack trapping by austenite. When crack propagated into austenite, there are two ways that crack can be trapped. First, when sharp crack tip penetrates from ferrite to austenite, the plastic deformation accompanied by the activation of dislocation emission can blunt this sharp crack tip. Second, the formation of the sub-grain boundary can hinder the crack propagation and result in a trapping of cleavage. These results suggest the plasticity degradation of austenite is not severe.

Though ferrite has lower resistance to HAC, the crack propagation can either be hampered by the presence of ferrite grain boundary and formation of slip band. In the former case, owing to an irregular lattice alignment at boundaries, a ferrite grain boundary possesses higher strength than the matrix, which could retard the crack propagation. In the latter case, the formation of slip band absorbs an amount of fracture energy and then lowers the stress

concentration at the tip of the crack. Thus, the crack propagation can be retarded by the formation of slip band in ferrite.

5.4 Chapter summary

In this Chapter, experimental results of effect of hydrogen on crack propagation in SDSS are presented. Key findings are:

- The plasticity degradation of austenite is not severe with a 10 days hydrogen charge. Ferrite has lower resistance to HAC compared with austenite in SDSS.
- In austenite, trapping of crack tips can be achieved by dislocation emission and formation of sub-grain boundary ahead of the crack tip.

Chapter 6

Conclusions and future work

In this section, the conclusion and future work will be given. Section 6.1 summaries the key outcomes of this work. Section 6.2 presents the future works based on this study.

6.1 Conclusions

Though super duplex stainless steel has achieved successes in industrial application, the challenges remain during manufacturing, processing and servicing, i.e. precipitation and hydrogen embrittlement. To overcome these challenges, studies of microstructure change and hydrogen embrittlement were carried out in this work.

In SDSS, precipitates of σ phase, χ phase, carbides and nitrides can be formed. The SEM results reveal a small amount of σ phase can be formed within 6 min ageing at 800°C. When the sample has 30 min ageing at 800°C, σ phase has an obvious precipitation at both grain boundaries and phase boundaries. Compared with σ phase, precipitation of χ phase is faster whose presence is detected in the sample with 6 min ageing at 800°C. A moderate increasing of precipitation volume is realised in samples with 30 min and 60 min ageing at 800°C. This result is comparing well with the thermodynamic modelling of σ phase and χ phase evolution in such conditions. In the sample with 30 min ageing at 800°C, the rod-like Cr_2N are preferred to precipitate at boundaries and in the ferrite matrix. Their dimensions are about 200 nm to 300 nm in length and tens of nanometres in width. A lamellar M_{23}C_6 is characterised at a phase boundary with a thickness of about 20 nm. The presentation of such M_{23}C_6 seems able to dramatically facilitate the Cr_2N precipitation. In the HAZ of the weldment, the precipitation of σ phase, χ phase and nitrides is detected. In

addition, nano-size Cr_2N precipitates were characterised at both ferrite-ferrite grain boundaries and ferrite-austenite phase boundaries.

The EBSD study depicts the hydrogen assisted crack tends to propagate through ferrite phase, which shows a low resistance to hydrogen assisted cracks in ferrite. Though the ferrite has lower resistance to hydrogen embrittlement than austenite, both phases are capable to trap cracks. In austenite phase, the formation of sub-grain boundaries is one mechanism to trap cracking tip owing to a higher strength being provided by the grain boundary. In ferrite, the cleavage features present frequently in ferrite grains. Nevertheless, the cracking tip is still possible to be trapped by the presence of ferrite grain boundary whose disordered lattice structure can provide a greater strength than ferrite matrix.

Using TOF neutron diffractometry, the dislocation density is probed in hydrogen charged SDSS with different pre-strain. In samples with less than 5% pre-strain, the hydrogen charging triggers the dislocation multiplication in both ferrite and austenite. In contrast, in samples with more than 10% pre-strain, the dislocation multiplication is not increased in proportion to pre-strain level. This result suggests the condition of residual stress is critical for hydrogen to activate dislocation multiplication.

6.2 Future work

The present work studies the microstructure change and hydrogen embrittlement in super duplex stainless steel. A large potential exists to a further extent the studies in following aspects:

- With higher chromium and nitrogen alloying in SDSS, it is important to understand the precipitation mechanism of high chromium and nitrogen contained Cr_2N . In this study, a precipitation phenomenon of nano-size Cr_2N rods on lamellar M_{23}C_6 is

reported. Nevertheless, this precipitation mechanism still needs further investigation including thermal dynamic analysis and characterisation work.

- Using TOF neutron diffraction, it has been measured that hydrogen can activate the dislocation multiplication in both ferrite and austenite in SDSS. A mechanism is proposed that the residual stress is critical for dislocation multiplication in the duplex structured steels. However, the residual stress states are not clear in these different pre-strain samples. Therefore, it would be valuable to measure the residual stress state and investigate its relationship with dislocation multiplication.
- The hydrogen assisted crack is a critical topic to be understood. We have shown there are several mechanisms that can trap the crack tips in both ferrite and austenite in SDSS. Nevertheless, it is still not clear that how much contribution can be made from the individual trapping mechanism.

References

- [1] J.O. Nilsson, Super duplex stainless steels, *Materials Science and Technology* 8(8) (1992) 685-700.
- [2] K. Lo, C. Shek, J. Lai, Recent developments in stainless steels, *Materials Science and Engineering R* 65(4) (2009) 39-104.
- [3] X.Z. Liang, M.F. Dodge, W. Liang, H.B. Dong, Precipitation of chromium nitride nano-rods on lamellar carbides along austenite-ferrite boundaries in super duplex stainless steel, *Scripta Materialia* 127 (2017) 45-48.
- [4] M. Knyazeva, M. Pohl, Duplex Steels. Part II: Carbides and Nitrides, *Metallogr. Microstruct. Anal.* 2(5) (2013) 343-351.
- [5] H.K.D.H. Bhadeshia, Prevention of Hydrogen Embrittlement in Steels, *ISIJ International* 56(1) (2016) 24-36.
- [6] K. Takasawa, R. Ikeda, N. Ishikawa, R. Ishigaki, Effects of grain size and dislocation density on the susceptibility to high-pressure hydrogen environment embrittlement of high-strength low-alloy steels, *International Journal of Hydrogen Energy* 37(3) (2012) 2669-2675.
- [7] M. Nagumo, Characteristic Features of Deformation and Fracture in Hydrogen Embrittlement, *Fundamentals of Hydrogen Embrittlement*, Springer Singapore, Singapore, (2016), 137-165.
- [8] G. Lu, E. Kaxiras, Hydrogen embrittlement of aluminum: the crucial role of vacancies, *Physical Review Letters* 94(15) (2005) 155501.

- [9] H. Vehoff, W. Rothe, Gaseous hydrogen embrittlement in FeSi- and Ni-single crystals, *Acta Metallurgica* 31(11) (1983) 1781-1793.
- [10] D.F. Teter, I.M. Robertson, H.K. Birnbaum, The effects of hydrogen on the deformation and fracture of β -titanium, *Acta Materialia* 49(20) (2001) 4313-4323.
- [11] R. Kirchheim, Reducing grain boundary, dislocation line and vacancy formation energies by solute segregation. I. Theoretical background, *Acta Materialia* 55(15) (2007) 5129-5138.
- [12] R. Kirchheim, Reducing grain boundary, dislocation line and vacancy formation energies by solute segregation: II. Experimental evidence and consequences, *Acta Materialia* 55(15) (2007) 5139-5148.
- [13] T.S. Taylor, T. Pendlington, R. Bird, Foinaven Super Duplex Materials Cracking Investigation, Offshore Technology Conference.
- [14] B. Voronenko, Austenitic-ferritic stainless steels: A state-of-the-art review, *Met Sci Heat Treat* 39(10) (1997) 428-437.
- [15] I.M. Association, T. Stainless, Practical guidelines for the fabrication of duplex stainless steels, International Molybdenum Association 2014.
- [16] A.R. Akisanya, U. Obi, N.C. Renton, Effect of ageing on phase evolution and mechanical properties of a high tungsten super-duplex stainless steel, *Materials Science and Engineering A* 535 (2012) 281-289.
- [17] A. Rokanopoulou, G. Papadimitriou, Production of high nitrogen surfaces on 2205 duplex stainless steel substrate using the PTA technique, *Materials Science and Technology* 27(9) (2011) 1391-1398.

- [18] J. Alsarraf, Hydrogen Embrittlement Susceptibility of Super Duplex Stainless Steels, (2010).
- [19] M. Kaneko, H.S. Isaacs, Effects of molybdenum on the pitting of ferritic- and austenitic-stainless steels in bromide and chloride solutions, *Corrosion Science* 44(8) (2002) 1825-1834.
- [20] C.-J. Park, H.-S. Kwon, Effects of aging at 475 °C on corrosion properties of tungsten-containing duplex stainless steels, *Corrosion Science* 44(12) (2002) 2817-2830.
- [21] K. Ogawa, H. Okamoto, M. Igarashi, M. Ueda, T. Mori, T. Kobayashi, Effects of tungsten on precipitation behaviour of intermetallic compounds in the HAZ of duplex stainless steel: Study of weldability of high-tungsten duplex stainless steel (2nd Report), *Welding international* 11(1) (1997) 14-22.
- [22] C.-C. Hsieh, W. Wu, Overview of Intermetallic Sigma Phase Precipitation in Stainless Steels, *ISRN Metallurgy* (2012).
- [23] W. Treitschke, G. Tammann, Enthalpy of formation for σ -phase solid solutions at 1060 K, *Anorganische Chemie* 55 (1907) 707-708.
- [24] E.C.B.a.W.E. Griffiths, An introduction to the Iron-Chromium Nickel alloys, *Transactions American Institute of Mining, Metallurgical and Petroleum Engineers* vol. 75 (1927) pp. 166–213.
- [25] D.E. Villanueva, F. Junior, R. Plaut, A. Padilha, Comparative study on sigma phase precipitation of three types of stainless steels: austenitic, superferritic and duplex, *Materials Science and Technology* 22(9) (2006) 1098-1104.
- [26] D.M. Escriba, E. Materna-Morris, R.L. Plaut, A.F. Padilha, Chi-phase precipitation in a duplex stainless steel, *Materials Characterization* 60(11) (2009) 1214-1219.

- [27] A.F. Padilha, D. Aguiar, R. Plaut, Duplex Stainless Steels: A Dozen of Significant Phase Transformations, Defect and Diffusion Forum, Trans Tech Publ, 2012, pp. 163-174.
- [28] N. Sathirachinda, R. Pettersson, S. Wessman, J. Pan, Study of nobility of chromium nitrides in isothermally aged duplex stainless steels by using SKPFM and SEM/EDS, Corrosion Science 52(1) (2010) 179-186.
- [29] N. Sathirachinda, R. Pettersson, S. Wessman, U. Kivisäkk, J. Pan, Scanning Kelvin probe force microscopy study of chromium nitrides in 2507 super duplex stainless steel—Implications and limitations, Electrochimica Acta 56(4) (2011) 1792-1798.
- [30] N. Pettersson, R.A. Pettersson, S. Wessman, Precipitation of Chromium Nitrides in the Super Duplex Stainless Steel 2507, Metallurgical and Materials Transactions A 46(3) (2015) 1062-1072.
- [31] A. Ramirez, J. Lippold, S. Brandi, The relationship between chromium nitride and secondary austenite precipitation in duplex stainless steels, Metallurgical and Materials Transactions A 34(8) (2003) 1575-1597.
- [32] W.D. Callister, Jr., D.G. Rethwisch, Materials science and engineering, Wiley, Hoboken, N.J, 2011.
- [33] N. Kamikawa, K. Sato, G. Miyamoto, M. Murayama, N. Sekido, K. Tsuzaki, T. Furuhashi, Stress-strain behavior of ferrite and bainite with nano-precipitation in low carbon steels, Acta Materialia 83 (2015) 383-396.
- [34] J.Y. He, H. Wang, H.L. Huang, X.D. Xu, M.W. Chen, Y. Wu, X.J. Liu, T.G. Nieh, K. An, Z.P. Lu, A precipitation-hardened high-entropy alloy with outstanding tensile properties, Acta Materialia 102 (2016) 187-196.

- [35] A. Barnoush, M. Asgari, R. Johnsen, Resolving the hydrogen effect on dislocation nucleation and mobility by electrochemical nanoindentation, *Scripta Materialia* 66(6) (2012) 414-417.
- [36] W.D. Nix, H. Gao, Indentation size effects in crystalline materials: a law for strain gradient plasticity, *Journal of the Mechanics and Physics of Solids* 46(3) (1998) 411-425.
- [37] C.A. Schuh, T.G. Nieh, T. Yamasaki, Hall–Petch breakdown manifested in abrasive wear resistance of nanocrystalline nickel, *Scripta Materialia* 46(10) (2002) 735-740.
- [38] H. Bhadeshia, R. Honeycombe, *Steels Microstructure and Properties*, Elsevier, Oxford (2006) 276-276.
- [39] S. Nambu, N. Shibuta, M. Ojima, J. Inoue, T. Koseki, H.K.D.H. Bhadeshia, In situ observations and crystallographic analysis of martensitic transformation in steel, *Acta Materialia* 61(13) (2013) 4831-4839.
- [40] Y. Zhang, N.R. Tao, K. Lu, Mechanical properties and rolling behaviors of nano-grained copper with embedded nano-twin bundles, *Acta Materialia* 56(11) (2008) 2429-2440.
- [41] C. Borchers, Y. Chen, M. Deutges, S. Goto, R. Kirchheim, Carbon-defect interaction during recovery and recrystallization of heavily deformed pearlitic steel wires, *Philosophical Magazine Letters* 90(8) (2010) 581-588.
- [42] R. Madec, B. Devincre, L. Kubin, T. Hoc, D. Rodney, The Role of Collinear Interaction in Dislocation-Induced Hardening, *Science* 301(5641) (2003) 1879-1882.
- [43] K. Lu, Stabilizing nanostructures in metals using grain and twin boundary architectures, *Nature Reviews Materials* 1 (2016) 16019.

- [44] K. Lu, L. Lu, S. Suresh, Strengthening materials by engineering coherent internal boundaries at the nanoscale, *Science* 324(5925) (2009) 349-352.
- [45] J.W. Martin, Particle strengthening of metals and alloys, *Materials Science and Technology* 13(8) (1997) 705.
- [46] <http://www.diagrams.science/periodic-table-trends-atomic-radius/>
- [47] W.H. Johnson, On some remarkable changes produced in iron and steel by the action of hydrogen and acids, *Proceedings of the Royal Society of London* 23(156-163) (1874) 168-179.
- [48] T. Tsuru, Y. Huang, M.R. Ali, A. Nishikata, Hydrogen entry into steel during atmospheric corrosion process, *Corrosion Science* 47(10) (2005) 2431-2440.
- [49] E. Owczarek, T. Zakroczymski, Hydrogen transport in a duplex stainless steel, *Acta Materialia* 48(12) (2000) 3059-3070.
- [50] V. Olden, A. Saai, L. Jemblie, R. Johnsen, FE simulation of hydrogen diffusion in duplex stainless steel, *International Journal of Hydrogen Energy* 39(2) (2014) 1156-1163.
- [51] V. Olden, C. Thaulow, R. Johnsen, Modelling of hydrogen diffusion and hydrogen induced cracking in supermartensitic and duplex stainless steels, *Materials and Design* 29(10) (2008) 1934-1948.
- [52] D.R. Askeland, *The science and engineering of materials*, Brooks/Cole Engineering Division, Monterey, Calif, (1984).
- [53] J.D. Fast, *Gases in metals*, Macmillan New York 1976.
- [54] I. Robertson, D. Tetter, Controlled environment transmission electron microscopy, *Microscopy research and technique* 42(4) (1998) 260.

- [55] J. Morlet, H. Johnson, A. Troiano, A new concept of hydrogen embrittlement in steel, Wright Air Development Center, Air Research and Development Command, United States Air Force (1957).
- [56] A.R. Troiano, The role of hydrogen and other interstitials in the mechanical behavior of metals, *Metallogr. Microstruct. Anal.* 5(6) (2016) 557-569.
- [57] A.R. Troiano, The role of hydrogen and other interstitials in the mechanical behavior of metals, *trans. ASM* 52(1) (1960) 54-80.
- [58] R.A. Oriani, The diffusion and trapping of hydrogen in steel, *Acta metallurgica* 18(1) (1970) 147-157.
- [59] R. Oriani, P. Josephic, Equilibrium aspects of hydrogen-induced cracking of steels, *Acta Metallurgica* 22(9) (1974) 1065-1074.
- [60] R. Oriani, A mechanistic theory of hydrogen embrittlement of steels, *Berichte der Bunsengesellschaft für physikalische Chemie* 76(8) (1972) 848-857.
- [61] R. Oriani, P. Josephic, Equilibrium and kinetic studies of the hydrogen-assisted cracking of steel, *Acta Metallurgica* 25(9) (1977) 979-988.
- [62] P. Ferreira, I. Robertson, H. Birnbaum, Hydrogen effects on the interaction between dislocations, *Acta Materialia* 46(5) (1998) 1749-1757.
- [63] I. Robertson, P. Sofronis, A. Nagao, M.L. Martin, S. Wang, D.W. Gross, K.E. Nygren, Hydrogen Embrittlement Understood, *Metallurgical and Materials Transactions A* 46(6) (2015) 2323-2341.
- [64] D.P. Abraham, C.J. Altstetter, Hydrogen-enhanced localization of plasticity in an austenitic stainless steel, *Metallurgical and Materials Transactions A* 26(11) (1995) 2859-2871.

- [65] D.P. Abraham, C.J. Altstetter, The effect of hydrogen on the yield and flow stress of an austenitic stainless steel, *Metallurgical and Materials Transactions A* 26(11) (1995) 2849-2858.
- [66] J. Song, W. Curtin, Atomic mechanism and prediction of hydrogen embrittlement in iron, *Nature Materials* 12(2) (2013) 145-151.
- [67] J. Song, W. Curtin, A nanoscale mechanism of hydrogen embrittlement in metals, *Acta Materialia* 59(4) (2011) 1557-1569.
- [68] J. Song, W.A. Curtin, Mechanisms of hydrogen-enhanced localized plasticity: An atomistic study using α -Fe as a model system, *Acta Materialia* 68 (2014) 61-69.
- [69] S. Li, Y. Li, Y.-C. Lo, T. Neeraj, R. Srinivasan, X. Ding, J. Sun, L. Qi, P. Gumbsch, J. Li, The interaction of dislocations and hydrogen-vacancy complexes and its importance for deformation-induced proto nano-voids formation in α -Fe, *International Journal of Plasticity* 74 (2015) 175-191.
- [70] D. Xie, S. Li, M. Li, Z. Wang, P. Gumbsch, J. Sun, E. Ma, J. Li, Z. Shan, Hydrogenated vacancies lock dislocations in aluminium, *Nature Communications* 7 (2016) 13341.
- [71] C. Varvenne, O. Mackain, L. Proville, E. Clouet, Hydrogen and vacancy clustering in zirconium, *Acta Materialia* 102 (2016) 56-69.
- [72] H. Momida, Y. Asari, Y. Nakamura, Y. Tateyama, T. Ohno, Hydrogen-enhanced vacancy embrittlement of grain boundaries in iron, *Physical Review B* 88(14) (2013) 144107.
- [73] Y. Tateyama, T. Ohno, Stability and clusterization of hydrogen-vacancy complexes in alpha Fe: An ab initio study, *Physical Review B* 67(17) (2003) 174105.

- [74] S. Wang, N. Hashimoto, Y. Wang, S. Ohnuki, Activation volume and density of mobile dislocations in hydrogen-charged iron, *Acta Materialia* 61(13) (2013) 4734-4742.
- [75] Y.Z. Chen, H.P. Barth, M. Deutges, C. Borchers, F. Liu, R. Kirchheim, Increase in dislocation density in cold-deformed Pd using H as a temporary alloying addition, *Scripta Materialia* 68(9) (2013) 743-746.
- [76] M. Deutges, H.P. Barth, Y. Chen, C. Borchers, R. Kirchheim, Hydrogen diffusivities as a measure of relative dislocation densities in palladium and increase of the density by plastic deformation in the presence of dissolved hydrogen, *Acta Materialia* 82 (2015) 266-274.
- [77] A. Barnoush, M. Zamanzade, H. Vehoff, Direct observation of hydrogen-enhanced plasticity in super duplex stainless steel by means of in situ electrochemical methods, *Scripta Materialia* 62(5) (2010) 242-245.
- [78] A. Oudriss, J. Creus, J. Bouhattate, E. Conforto, C. Berziou, C. Savall, X. Feaugas, Grain size and grain-boundary effects on diffusion and trapping of hydrogen in pure nickel, *Acta Materialia* 60(19) (2012) 6814-6828.
- [79] C.A. Wert, Trapping of hydrogen in metals, in: G. Alefeld, J. Völkl (Eds.), *Hydrogen in Metals II: Application-Oriented Properties*, Springer Berlin Heidelberg, Berlin, Heidelberg, 1978, pp. 305-330.
- [80] D. Di Stefano, M. Mrovec, C. Elsässer, First-principles investigation of hydrogen trapping and diffusion at grain boundaries in nickel, *Acta Materialia* 98 (2015) 306-312.
- [81] A. Oudriss, J. Creus, J. Bouhattate, C. Savall, B. Peraudeau, X. Feaugas, The diffusion and trapping of hydrogen along the grain boundaries in polycrystalline nickel, *Scripta Materialia* 66(1) (2012) 37-40.

- [82] O. Sobol, F. Straub, T. Wirth, G. Holzlechner, T. Boellinghaus, W.E.S. Unger, Real Time Imaging of Deuterium in a Duplex Stainless Steel Microstructure by Time-of-Flight SIMS, *Scientific Reports* 6 (2016) 19929.
- [83] F.J. Humphreys, Characterisation of fine-scale microstructures by electron backscatter diffraction (EBSD), *Scripta Materialia* 51(8) (2004) 771-776.
- [84] D. Jorge-Badiola, A. Iza-Mendia, I. Gutiérrez, Study by EBSD of the development of the substructure in a hot deformed 304 stainless steel, *Materials Science and Engineering A* 394(1-2) (2005) 445-454.
- [85] V. Venegas, F. Caleyó, J.L. González, T. Baudin, J.M. Hallen, R. Penelle, EBSD study of hydrogen-induced cracking in API-5 L-X46 pipeline steel, *Scripta Materialia* 52(2) (2005) 147-152.
- [86] M. Daly, T.L. Burnett, E.J. Pickering, O.C.G. Tuck, F. Léonard, R. Kelley, P.J. Withers, A.H. Sherry, A multi-scale correlative investigation of ductile fracture, *Acta Materialia* 130 (2017) 56-68.
- [87] A. Khosravani, D.T. Fullwood, B.L. Adams, T.M. Rampton, M.P. Miles, R.K. Mishra, Nucleation and propagation of twins in AZ31 magnesium alloy, *Acta Materialia* 100 (2015) 202-214.
- [88] H. Masuda, H. Tobe, E. Sato, Y. Sugino, S. Ukai, Two-dimensional grain boundary sliding and mantle dislocation accommodation in ODS ferritic steel, *Acta Materialia* 120 (2016) 205-215.
- [89] P.W. Trimby, Y. Cao, Z. Chen, S. Han, K.J. Hemker, J. Lian, X. Liao, P. Rottmann, S. Samudrala, J. Sun, J.T. Wang, J. Wheeler, J.M. Cairney, Characterizing deformed

ultrafine-grained and nanocrystalline materials using transmission Kikuchi diffraction in a scanning electron microscope, *Acta Materialia* 62 (2014) 69-80.

[90] N. Mortazavi, M. Esmaily, M. Halvarsson, The capability of Transmission Kikuchi Diffraction technique for characterizing nano-grained oxide scales formed on a FeCrAl stainless steel, *Materials Letters* 147 (2015) 42-45.

[91] P.W. Trimby, Orientation mapping of nanostructured materials using transmission Kikuchi diffraction in the scanning electron microscope, *Ultramicroscopy* 120 (2012) 16-24.

[92] S. Suzuki, Features of transmission EBSD and its application, *Jom* 65(9) (2013) 1254-1263.

[93] M. Abbasi, D.-I. Kim, H.-U. Guim, M. Hosseini, H. Danesh-Manesh, M. Abbasi, Application of Transmitted Kikuchi Diffraction in Studying Nano-oxide and Ultrafine Metallic Grains, *ACS Nano* 9(11) (2015) 10991-11002.

[94] J. Small, J. Michael, D. Bright, Improving the quality of electron backscatter diffraction (EBSD) patterns from nanoparticles, *Journal of Microscopy* 206(2) (2002) 170-178.

[95] R. Keller, R. Geiss, Transmission EBSD from 10 nm domains in a scanning electron microscope, *Journal of Microscopy* 245(3) (2012) 245-251.

[96] J. Kadkhodapour, S. Schmauder, D. Raabe, S. Ziaei-Rad, U. Weber, M. Calcagnotto, Experimental and numerical study on geometrically necessary dislocations and non-homogeneous mechanical properties of the ferrite phase in dual phase steels, *Acta Materialia* 59(11) (2011) 4387-4394.

- [97] M. Calcagnotto, D. Ponge, E. Demir, D. Raabe, Orientation gradients and geometrically necessary dislocations in ultrafine grained dual-phase steels studied by 2D and 3D EBSD, *Materials Science and Engineering A* 527(10–11) (2010) 2738-2746.
- [98] P.D. Littlewood, T.B. Britton, A.J. Wilkinson, Geometrically necessary dislocation density distributions in Ti–6Al–4V deformed in tension, *Acta Materialia* 59(16) (2011) 6489-6500.
- [99] J. Jiang, T.B. Britton, A.J. Wilkinson, Measurement of geometrically necessary dislocation density with high resolution electron backscatter diffraction: Effects of detector binning and step size, *Ultramicroscopy* 125 (2013) 1-9.
- [100] A. Ramazani, K. Mukherjee, A. Schwedt, P. Goravanchi, U. Prahl, W. Bleck, Quantification of the effect of transformation-induced geometrically necessary dislocations on the flow-curve modelling of dual-phase steels, *International Journal of Plasticity* 43 (2013) 128-152.
- [101] H.-W. Yen, S.W. Ooi, M. Eizadjou, A. Breen, C.-Y. Huang, H.K.D.H. Bhadeshia, S.P. Ringer, Role of stress-assisted martensite in the design of strong ultrafine-grained duplex steels, *Acta Materialia* 82 (2015) 100-114.
- [102] J.L. Sun, P.W. Trimby, X. Si, X.Z. Liao, N.R. Tao, J.T. Wang, Nano twins in ultrafine-grained Ti processed by dynamic plastic deformation, *Scripta Materialia* 68(7) (2013) 475-478.
- [103] M. Daymond, L. Edwards, Scientific Review: ENGIN-X: A Fully Refined Diffractometer Designed Specifically for Measurement of Stress, *Neutron News* 15(1) (2004) 24-29.

- [104] J. Ågren, Calculation of phase diagrams: Calphad, Current opinion in solid state and materials science 1(3) (1996) 355-360.
- [105] J.-O. Andersson, T. Helander, L. Höglund, P. Shi, B. Sundman, Thermo-Calc & DICTRA, computational tools for materials science, Calphad 26(2) (2002) 273-312.
- [106] N. Saunders, U.K. Guo, X. Li, A. Miodownik, J.-P. Schillé, Using JMatPro to model materials properties and behavior, JOM Journal of the Minerals, Metals and Materials Society 55(12) (2003) 60-65.
- [107] G.K. Williamson, R.E. Smallman, III. Dislocation densities in some annealed and cold-worked metals from measurements on the X-ray debye-scherrer spectrum, Philosophical Magazine 1(1) (1956) 34-46.
- [108] F. Christien, M.T.F. Telling, K.S. Knight, Neutron diffraction in situ monitoring of the dislocation density during martensitic transformation in a stainless steel, Scripta Materialia 68(7) (2013) 506-509.
- [109] E.I. Galindo-Nava, P.E.J. Rivera-Díaz-del-Castillo, A model for the microstructure behaviour and strength evolution in lath martensite, Acta Materialia 98 (2015) 81-93.
- [110] B. Kim, E. Boucard, T. Sourmail, D. San Martín, N. Gey, P.E.J. Rivera-Díaz-del-Castillo, The influence of silicon in tempered martensite: Understanding the microstructure-properties relationship in 0.5–0.6 wt.% C steels, Acta Materialia 68 (2014) 169-178.
- [111] M. Shamma, E.a.N. Caspi, B. Anasori, B. Clausen, D.W. Brown, S.C. Vogel, V. Presser, S. Amini, O. Yeheskel, M.W. Barsoum, In situ neutron diffraction evidence for fully reversible dislocation motion in highly textured polycrystalline Ti₂AlC samples, Acta Materialia 98 (2015) 51-63.

- [112] F. Christien, M.T.F. Telling, K.S. Knight, R. Le Gall, A method for the monitoring of metal recrystallization based on the in-situ measurement of the elastic energy release using neutron diffraction, *Review of Scientific Instruments* 86(5) (2015) 053901.
- [113] G.K. Williamson, W.H. Hall, X-ray line broadening from fcc aluminium and wolfram, *Acta Metallurgica* 1(1) (1953) 22-31.
- [114] E.A. Faulkner, Calculation of stored energy from broadening of X-ray diffraction lines, *Philosophical Magazine* 5(53) (1960) 519-521.
- [115] G.E. Dieter, D.J. Bacon, *Mechanical metallurgy*, McGraw-Hill New York (1986).
- [116] C. Moreton-Smith, S. Johnston, F. Akeroyd, Open GENIE—a generic multi-platform program for the analysis of neutron scattering data, *Journal of Neutron Research* 4(1-4) (1996) 41-47.
- [117] A. Arsenlis, D.M. Parks, Crystallographic aspects of geometrically-necessary and statistically-stored dislocation density, *Acta Materialia* 47(5) (1999) 1597-1611.
- [118] J. Nye, Some geometrical relations in dislocated crystals, *Acta Metallurgica* 1(2) (1953) 153-162.
- [119] M.A. Meyers, A. Mishra, D.J. Benson, Mechanical properties of nanocrystalline materials, *Progress in Materials Science* 51(4) (2006) 427-556.
- [120] H. Gao, Y. Huang, W. Nix, J. Hutchinson, Mechanism-based strain gradient plasticity—I. Theory, *Journal of the Mechanics and Physics of Solids* 47(6) (1999) 1239-1263.
- [121] M. Ashby, The deformation of plastically non-homogeneous materials, *Philosophical Magazine* 21(170) (1970) 399-424.

- [122] P.J. Konijnenberg, S. Zaeferrer, D. Raabe, Assessment of geometrically necessary dislocation levels derived by 3D EBSD, *Acta Materialia* 99 (2015) 402-414.
- [123] A. Kundu, D.P. Field, Influence of plastic deformation heterogeneity on development of geometrically necessary dislocation density in dual phase steel, *Materials Science and Engineering A* 667 (2016) 435-443.
- [124] J. Jiang, T.B. Britton, A.J. Wilkinson, Evolution of dislocation density distributions in copper during tensile deformation, *Acta Materialia* 61(19) (2013) 7227-7239.
- [125] J. Jiang, T.B. Britton, A.J. Wilkinson, Accumulation of geometrically necessary dislocations near grain boundaries in deformed copper, *Philosophical Magazine Letters* 92(11) (2012) 580-588.
- [126] L. Kubin, A. Mortensen, Geometrically necessary dislocations and strain-gradient plasticity: a few critical issues, *Scripta Materialia* 48(2) (2003) 119-125.
- [127] W. Woo, T. Ungár, Z. Feng, E. Kenik, B. Clausen, X-ray and neutron diffraction measurements of dislocation density and subgrain size in a friction-stir-welded aluminum alloy, *Metallurgical and Materials Transactions A* 41(5) (2010) 1210-1216.
- [128] T. Ungár, S. Ott, P.G. Sanders, A. Borbély, J.R. Weertman, Dislocations, grain size and planar faults in nanostructured copper determined by high resolution X-ray diffraction and a new procedure of peak profile analysis, *Acta Materialia* 46(10) (1998) 3693-3699.
- [129] J.G. Suits, J.R. Low, Dislocation etch pits in silicon iron, *Acta Metallurgica* 5(5) (1957) 285-289.
- [130] A. Vilalta-Clemente, G. Naresh-Kumar, M. Nouf-Allahiani, P. Gamarra, M. di Forte-Poisson, C. Trager-Cowan, A. Wilkinson, Cross-correlation based high resolution electron

backscatter diffraction and electron channelling contrast imaging for strain mapping and dislocation distributions in InAlN thin films, *Acta Materialia* 125 (2017) 125-135.

[131] Q. Lu, Z. You, X. Huang, N. Hansen, L. Lu, Dependence of dislocation structure on orientation and slip systems in highly oriented nanotwinned Cu, *Acta Materialia* 127 (2017) 85-97.

[132] J. Pešička, R. Kužel, A. Dronhofer, G. Eggeler, The evolution of dislocation density during heat treatment and creep of tempered martensite ferritic steels, *Acta Materialia* 51(16) (2003) 4847-4862.

[133] R.K. Ham, The determination of dislocation densities in thin films, *Philosophical Magazine* 6(69) (1961) 1183-1184.

[134] B. David, C.C. Barry, *Transmission electron microscopy: A textbook for materials science*, Springer, 2009.

[135] J. Nowacki, A. Łukojc, Microstructural transformations of heat affected zones in duplex steel welded joints, *Materials Characterization* 56(4–5) (2006) 436-441.

[136] B. ISO, 148-1: 2009 ‘Metallic materials--Charpy pendulum impact test--Part 1: Test method’, British Standards Institution (2009).

[137] P.M. Anderson, J.P. Hirth, J. Lothe, *Theory of Dislocations*, Cambridge University Press (2017).

[138] E. Nes, K. Marthinsen, Y. Brechet, On the mechanisms of dynamic recovery, *Scripta Materialia* 47(9) (2002) 607-611.

[139] S. Harjo, Y. Tomota, M. Ono, Measurements of thermal residual elastic strains in ferrite–austenite Fe–Cr–Ni alloys by neutron and X-ray diffractions, *Acta Materialia* 47(1) (1998) 353-362.

- [140] A. Pundt, R. Kirchheim, Hydrogen in metals: microstructural aspects, *Annual Review Materials Research* 36 (2006) 555-608.
- [141] J. Johansson, M. Odén, X.-H. Zeng, Evolution of the residual stress state in a duplex stainless steel during loading, *Acta Materialia* 47(9) (1999) 2669-2684.
- [142] N. Jia, R. Lin Peng, Y. Wang, S. Johansson, P. Liaw, Micromechanical behavior and texture evolution of duplex stainless steel studied by neutron diffraction and self-consistent modeling, *Acta Materialia* 56(4) (2008) 782-793.
- [143] U.F. Kocks, H. Mecking, Physics and phenomenology of strain hardening: the FCC case, *Progress in Materials Science* 48(3) (2003) 171-273.
- [144] M. Delincé, Y. Bréchet, J.D. Embury, M.G.D. Geers, P.J. Jacques, T. Pardoen, Structure–property optimization of ultrafine-grained dual-phase steels using a microstructure-based strain hardening model, *Acta Materialia* 55(7) (2007) 2337-2350.
- [145] B. Devincere, T. Hoc, L. Kubin, Dislocation mean free paths and strain hardening of crystals, *Science* 320(5884) (2008) 1745-1748.
- [146] T. Zakroczymski, A. Glowacka, W. Swiatnicki, Effect of hydrogen concentration on the embrittlement of a duplex stainless steel, *Corrosion science* 47(6) (2005) 1403-1414.
- [147] P. Craidy, L. Briottet, D. Santos, Hydrogen–Microstructure–Mechanical properties interactions in super duplex stainless steel components, *International Journal of Hydrogen Energy* 40(47), (2015) 17084-17090.
- [148] A. Elhoud, N. Renton, W. Deans, Hydrogen embrittlement of super duplex stainless steel in acid solution, *International Journal of Hydrogen Energy* 35(12) (2010) 6455-6464.